Critical Effects and Universality in Graphene Quantum Dots

Inaugural-Dissertation

zur Erlangung des Doktorgrades der
Mathematisch-Naturwissenschaftlichen Fakultät der
Heinrich-Heine-Universität Düsseldorf

vorgelegt von

Denis Klöpfer

aus Moskau

Düsseldorf, September 2014

Aus dem Institut für Theoretische Physik IV
der Heinrich-Heine-Universität Düsseldorf

Gedruckt mit der Genehmigung der
Mathematisch-Naturwissenschaftlichen Fakultät der
Heinrich-Heine-Universität Düsseldorf

Referent: Prof. Dr. Reinhold Egger
koreferent: Prof. Dr. Dr. Carsten Müller
Tag der mündlichen Prüfung: 14.01.2015

This thesis is based on following original articles

Chapter 2

Electric-Dipole-Induced Universality for Dirac Fermions in Graphene
Alessandro De Martino, Denis Klöpfer, Davron Matrasulov and Reinhold Egger
Phys. Rev. Lett. **112**, 186603 (2014)

Scattering theory and ground-state energy of Dirac fermions in graphene with two Coulomb impurities
Denis Klöpfer, Alessandro De Martino, Davron Matrasulov and Reinhold Egger
EPJB **87**, 187 (2014)

Chapter 3

Bound States and Supercriticality in Graphene-Based Topological Insulators
Denis Klöpfer, Alessandro De Martino and Reinhold Egger
Crystals **3**, 14-27 (2013)

Zusammenfassung

Graphen ist ein zweidimensionaler Festkörper, welcher sich durch einzigartige Eigenschaften auszeichnet. Abgesehen von seiner mechanischen und chemischen Stabilität, hat es auch bemerkenswerte elektronische Eigenschaften, die sich durch äußere Einflussnahme in weiten Bereichen variieren lassen. Da sich Elektronen in Graphen wie relativistische Teilchen verhalten, bietet es ein ideales Versuchsfeld für Quanten-Elektrodynamik.

Im Rahmen dieser Arbeit befassen wir uns mit dem Einfluss äußerer Potentiale auf das Verhalten von Elektronen in Graphen mit Substrat-, oder Spin-Bahn-Effekt-induzierter Bandlücke. Genauer gesagt untersuchen wir die Fähigkeit dieser Potentiale Elektronen zu binden und das kritische Verhalten dieser Potentiale, also ihre Fähigkeit mit steigender Kopplungsstärke gebundene Elektronenniveaus wieder in eines der Bänder zu drücken, was dann Streuresonanzen erzeugen müsste.

Im ersten Teil (Kapitel 3) dieser Arbeit untersuchen wir zuerst den Einfluss zweier gleich geladener Coulomb-Zentren im endlichen Abstand auf die elektronische Struktur. Wir können sowohl den gebundenen Grundzustand charakterisieren, als auch den Abstand der Zentren bestimmen, bei welchem der Grundzustand kritisch wird. Ferner untersuchen wir den Einfluss zweier gegensätzlich geladener Coulomb Zentren im endlichen Abstand, also eines Dipols, im nicht relativistischen Grenzfall. Wir zeigen, dass dieser zwar immer, unabhängig von der Dipolstärke, eine unendliche Anzahl gebundener Niveaus erzeugt, und dass zusätzliche Klassen gebundener Niveaus bei gewissen Dipolstärken entstehen, das System jedoch nie kritisch wird.

Im zweiten Teil (Kapitel 4) wird der Einfluss von Spin-Bahn Kopplung auf das Spektrum eines Quantenpunkts untersucht, wobei uns ein Potentialtopf als Modell dient. Wir sind in der Lage sowohl das Spektrum gebundener Zustände, von denen immer mindestens einer existiert, als auch das Streuspektrum zu charakterisieren. Es findet sich außerdem eine Klasse Symmetrie-geschützter Zustände, welche parallel zu einem Kontinuum existieren, jedoch nicht zur Streuung beitragen. Wir gehen davon aus, dass ein Symmetrie-brechendes Störpotential zusätzliche Resonanzen erzeugen würde.

Summary

Graphene is a two dimensional solid, which is outstanding due to its unique properties. Besides its mechanical and chemical stability it additionally has notable electronic characteristics, which may be tuned over a wide range of regimes. Since the quasiparticles in graphene behave as relativistic electrons, it offers a great opportunity for testing predictions of quantum electrodynamics, which may not be accessible otherwise. Within this work we investigate the effect of exterior potentials, forming quantum dots, on electron behavior in graphene with a gap induced by substrate or spin-orbit effects. More precisely, we investigate the ability of these potentials to bind electrons and we investigate the critical behavior of these potentials, i.e. their capability of pushing bound states into one of the bands creating scattering resonances.

In the first part (chapter 3) we focus on two Coulomb-type impurities separated by a finite distance. First we focus on equally charged impurities. We describe the behavior of the bound groundstate and estimate the critical distance between the centers in the case of a supercritical total charge of both centers. We then continue to investigate the effects of a dipole impurity, i.e. two oppositely charged Coulomb centers at a finite distance, in the non relativistic limit. We find that bound states exist for any finite dipole strength, but no criticality is possible. Statements about the full relativistic case are made using a numerical diagonalization procedure. Nevertheless, we observe resonances, which correspond to new sets of bound levels appearing at certain critical dipole moments. These levels exhibit certain universal features independent of the short range characteristics of the impurity.

In the second part (chapter 4) we focus on quantum dots in graphene under the influence of spin-orbit coupling. A potential well serves us as a model system. We are able to calculate the bound state spectrum as well as the resonance spectrum of the system. In particular, we show that always at least one bound state exists at finite potential strength. We also discover a class of symmetry protected states, which may exist within, but not coupled to, a continuum and therefore do not cause a scattering resonance. A symmetry breaking perturbation should lift the protection and new resonances should appear.

Contents

1 Introduction

Graphene consists of sp^2-hybritized carbon atoms, each covalently bound to three others by the sp^2 orbitals. It thus has the shape of a honeycomb formed of carbon atoms at the junctions, the links are σ-bonds [1]. Although it is abundant in the nature as the building part of graphite, which consists of many graphene layers stacked on each other bound by van der Waals force, for a long time it was not possible to isolate it and it was commonly believed that it may not be stable.

Nevertheless, its low energy quantum mechanical properties were investigated long ago, in 1947, when P.R. Wallace was initially investigating graphite using tight binding theory [2]. During his work he discovered that the electrons in pristine graphene at the Fermi surface behave like massless particles with a lightlike dispersion relation with the Fermi velocity $v_F \approx 3 \cdot 10^6 \, {}^{\mathrm{m}}/_{\mathrm{s}}$, a speed of light equivalent in graphene.

These striking properties became relevant when graphene was first isolated in 2004 by K. Novoselov et al. [3] by the scotch tape method, which earned the Nobel prize in 2010. Using this method graphene is synthesized from graphite by applying duct tape, which detaches flakes of multilayer graphene. Repeating the process on these flakes will eventually produce single layer graphene flakes with a thickness of $\sim 0.8\,\mathrm{nm}$, which may be seen by atomic force microscopy.

Other methods to prepare graphene are by heat desorption of SiC [4] or on metal surfaces [5]. The substrates, however, will strongly influence its properties in contrast to free standing graphene. For instance, a gap may be created and to turn it into an insulator, or it may be strongly doped to make it metallic [1]. Other methods to manipulate graphene are to introduce strain, which will result in effective electromagnetic potentials, by creating disorder and lattice defects [6], or by adsorbed impurities [7]. Ribbons of graphene also develop very distinct features depending on the nature of the edges [8].

Another class of tunable properties within graphene are its spin-orbit coupling capabilities, which may be tuned by curvature or normal to the plane electric fields [9] or by surface adatoms [10].

Other striking discoveries within graphene physics are the anomalous integer

quantum Hall effect [11] and the quantum spin Hall effect [12], the discovery of which induced the intense research on topological insulators.

As mentioned above, the electrons at the Fermi surface in graphene behave like relativistic particles. This makes it a simple to control lab environment for quantum electrodynamics. Due to its high tunability and lower quasiparticle velocities compared to the speed of light one may establish many regimes to observe effects, which would be difficult, if not impossible, to realize in three dimensional vacuum. One of these effects is the criticality of relativistic quantum systems cause by large charge concentrations [13] and potentials resultig from these. In the presence of such potentials bound levels may be pushed into the negative continuum and become scattering resonances. This effect should be observable for nuclei with a charge of $\sim 170e$. Of course, elements with such a high nuclear charge do not exist. In graphene, however, the charge necessary to create these effects is only of order $\sim 1e$ [14], which may be realized by deposition of adatom clusters on the surface [7].

In the first part of the thesis we will investigate the action of two separated Coulomb centers on graphene. One may think of two situations:

1. Equally charged centers.

2. Centers carrying opposite charges.

The first situation is easy to grasp intuitively. If the charges are close to each other, they act as a single center with twice the charge. On the other hand, if the charges are separated on a large scale[1], an electron would only see one of the centers, i.e. we again would deal with a single impurity. The crossover regime we will investigate using the linear combination of atomic orbitals method. Further, it will enable us to investigate at which distance between the centers the "concentration" of the charges is large enough to create criticality.

The second of the above situations is more difficult to understand a priori. If the centers are close to each other, the effective visible charge should be zero. May any electrons (or holes) then be bound at all? If not, what is the minimal distance to enable them to do so? And once an electron is bound, may it also become critical at some point? We will be able to address all of these questions within this work. Finally, we analyze the scattering of electrons by such an impurity.

The second part of the thesis will deal with quantum dots in graphene in the presence of strong spin-orbit coupling, which is a highly tunable property of graphene, see discussion below. We thus would like to investigate its effects on

[1] This scale is yet to be clarified.

the bound level spectrum as well as on the scattering, where a quantum well will serve us as a model system.

At last we would like to mention that many of the effects discussed here one may as well induce in surface states of topological insulators [15] and the so-called molecular graphene [16], which consists of carbon monoxide molecules assembled on a copper surface. Both of these systems exhibit the relativistic dispersion relation, which graphene is popular for.

2 Introduction to Theory of Graphene and Critical Effects in Relativistic Quantum Mechanics

2.1 Low-Energy Physics of Graphene

2.1.1 Microscopic Structure of Graphene

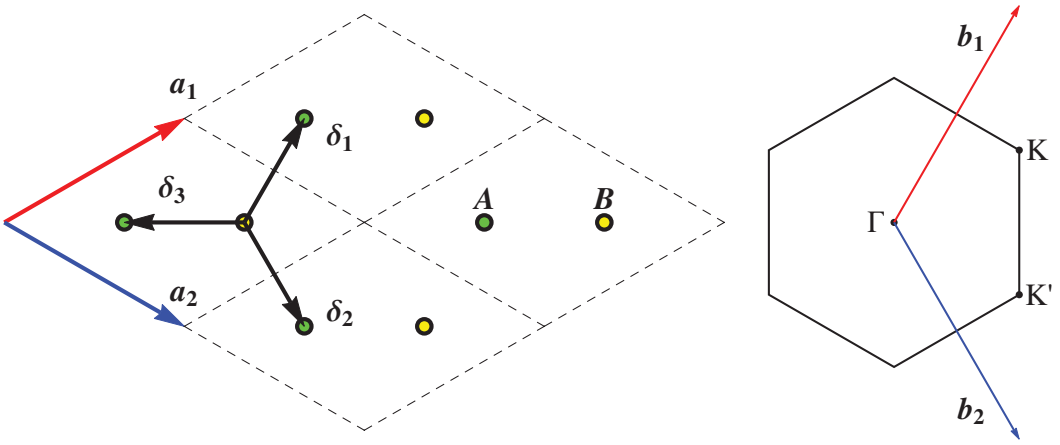

Figure 2.1.: Microscopic structure of graphene. Left: real space. Right: reciprocal space.

Graphene consists of sp^2-hybridized carbon atoms connected to their next neighbors by σ-bonds. Since the corresponding sp^2 states are all occupied, the bands formed by them are full and deep below the Fermi surface and thus do not contribute to the conductance. The remaining p-orbitals are normal to the plane. By interactions with neighboring atoms they are delocalized and thus form the π-band, see sec. 2.1.2.

The lattice that follows from this configuration is hexagonal and has a basis consisting of two atoms (sublattice A and B). The lattice vectors are [2]

$$\mathbf{a}_1 = \tfrac{a}{2}\begin{bmatrix} 3 \\ \sqrt{3} \end{bmatrix}, \quad \mathbf{a}_2 = \tfrac{a}{2}\begin{bmatrix} 3 \\ -\sqrt{3} \end{bmatrix} \tag{2.1}$$

and the vectors connecting any B-site to neighboring A-sites are given by

$$\boldsymbol{\delta}_1 = \tfrac{a}{2}\begin{bmatrix} 1 \\ \sqrt{3} \end{bmatrix}, \; \boldsymbol{\delta}_2 = \tfrac{a}{2}\begin{bmatrix} 1 \\ -\sqrt{3} \end{bmatrix}, \; \boldsymbol{\delta}_3 = a\begin{bmatrix} -1 \\ 0 \end{bmatrix},$$

where $a \approx 1.42$ Å is the next-neighbor distance. The corresponding connections from A-sites to B-sites one may find by $\boldsymbol{\delta}_i \to -\boldsymbol{\delta}_i$.

The reciprocal lattice is spanned by the vectors

$$\mathbf{b}_1 = \tfrac{2\pi}{3a}\begin{bmatrix} 1 \\ \sqrt{3} \end{bmatrix}, \quad \mathbf{b}_2 = \tfrac{2\pi}{3a}\begin{bmatrix} 1 \\ -\sqrt{3} \end{bmatrix}.$$

Correspondingly the first Brillouin-zone (1.BZ) is a hexagon, see fig. 2.1. The two of its nonequivalent corners (K-points) are

$$\mathbf{K} = \tfrac{2\pi}{3a}\begin{bmatrix} 1 \\ \frac{1}{\sqrt{3}} \end{bmatrix} \text{ and } \mathbf{K}' = \tfrac{2\pi}{3a}\begin{bmatrix} 1 \\ -\frac{1}{\sqrt{3}} \end{bmatrix}.$$

It turns out that the number of modes inside the 1.BZ exactly corresponds to the density of p-orbital-electrons (two per unit-cell) on graphene [2]. Due to this the π-bands are at half filling.

2.1.2 Tight Binding Theory of Graphene

Because of the weak coupling between the p-orbitals located at neighboring sites, the characteristics of the corresponding bands are well captured by the tight-binding theory (for general formulation see for instance [17] or any textbook on solid state physics). For the derivation (see [1] and the references within) one may start by introducing annihilation-operators corresponding to p-orbitals at site $\mathrm{A}_i(\mathrm{B}_i)$ with spin $s_z = s$, $a_{s,i}(b_{s,i})$, which obey fermionic anti-commutation relations:

$$\left\{a_{s,i}, a^\dagger_{s',j}\right\} = \delta_{i,j}\delta_{s,s'} = \left\{b_{s,i}, b^\dagger_{s',j}\right\}, \; \left\{a_{s,i}, a_{s',j}\right\} = 0 = \left\{b_{s,i}, b_{s',j}\right\}, \; \left\{a_{s,i}, b^{(\dagger)}_{s',j}\right\} = 0. \tag{2.2}$$

The p-orbital part of the (kinetic) Hamiltonian may now be formulated in terms of these operators:

$$H_T = -t \sum_{<i,j>,s} \left(a^\dagger_{s,i} b_{s,j} + b^\dagger_{s,i} a_{s,j}\right), \tag{2.3}$$

where $t \approx 2.6\,\mathrm{eV}$ is the hopping energy and the sum only runs over neighboring sites, which is denoted by $< i, j >$ in the sum argument. For now we skip the spin-index s, since both spin-sectors may be treated separately as long as no spin-changing are effects considered ($[H, s_z] = 0$). Now some Bloch operators may be constructed as linear combinations of the site creation operators (2.2)

$$a_{\mathbf{k}} = \frac{1}{\sqrt{\mathcal{N}}} \sum_i a_i \, \mathrm{e}^{\mathrm{i}\mathbf{k}\cdot\mathbf{r}_i^a}, \; b_{\mathbf{k}} = \frac{1}{\sqrt{\mathcal{N}}} \sum_i b_i \, \mathrm{e}^{\mathrm{i}\mathbf{k}\cdot\mathbf{r}_i^b}. \tag{2.4}$$

where $\mathcal{N}$ is the volume of the first Brillouin zone (normalization) and the sum runs over all lattice sites fig. 2.1. The reverse transformation is given by the formula

$$a_i = \frac{1}{\sqrt{\mathcal{N}}} \int_{1.BZ} d\mathbf{k} \, a_{\mathbf{k}} \, \mathrm{e}^{-\mathrm{i}\mathbf{k}\cdot\mathbf{r}_i^a}, \; b_i = \frac{1}{\sqrt{\mathcal{N}}} \int_{1.BZ} d\mathbf{k} \, b_{\mathbf{k}} \, \mathrm{e}^{-\mathrm{i}\mathbf{k}\cdot\mathbf{r}_i^b},$$

where the integral is taken over the first Brillouin zone. Note that due to the unitary nature of the transformation between a_i (b_i) and $a_{\mathbf{k}}$ ($b_{\mathbf{k}}$) the anti-commutation relations (2.2) are conserved:

$$\left\{a_{\mathbf{k}}, a^\dagger_{\mathbf{k}'}\right\} = \delta(\mathbf{k} - \mathbf{k}') = \left\{b_{\mathbf{k}}, b^\dagger_{\mathbf{k}'}\right\}, \; \{a_{\mathbf{k}}, a_{\mathbf{k}'}\} = 0 = \{b_{\mathbf{k}}, b_{\mathbf{k}'}\}, \; \left\{a_{\mathbf{k}}, b^{(\dagger)}_{\mathbf{k}'}\right\} = 0. \tag{2.5}$$

Using (2.5) H may be expressed by the Bloch operators as follows:

$$[H_T, a_{\mathbf{k}}] = t \sum_{\delta_i} \mathrm{e}^{-\mathrm{i}\delta_i\cdot\mathbf{k}} b_{\mathbf{k}} = t f(\mathbf{k}) b_{\mathbf{k}},$$

$$\text{and similarly} \quad [H_T, b_{\mathbf{k}}] = t f^*(\mathbf{k}) a_{\mathbf{k}},$$

where

$$f(\mathbf{k}) = 2\mathrm{e}^{-\mathrm{i}k_x a/2} \cos(\sqrt{3}k_y a/2) + \mathrm{e}^{-\mathrm{i}k_x a}.$$

Using this one may write

$$H_T = t \int_{1.BZ} d\mathbf{k} \, \psi^\dagger_{\mathbf{k}} \begin{bmatrix} & f^*(\mathbf{k}) \\ f(\mathbf{k}) & \end{bmatrix} \psi_{\mathbf{k}}, \; \psi_{\mathbf{k}} = [a_{\mathbf{k}}, b_{\mathbf{k}}]^T.$$

Since the result is diagonal in k one may now give the dispersion-relation:

$$\epsilon_{\mathbf{k}} = \pm t |f(\mathbf{k})| = \pm t \sqrt{3 + 2\cos(\sqrt{3}k_y a) + 4\cos(\tfrac{\sqrt{3}k_y a}{2}) \cos(\tfrac{3}{2}k_x a)}. \tag{2.6}$$

One may note that $f(\mathbf{K}^{(\prime)}) = 0$, thus it makes sense to expand H around the

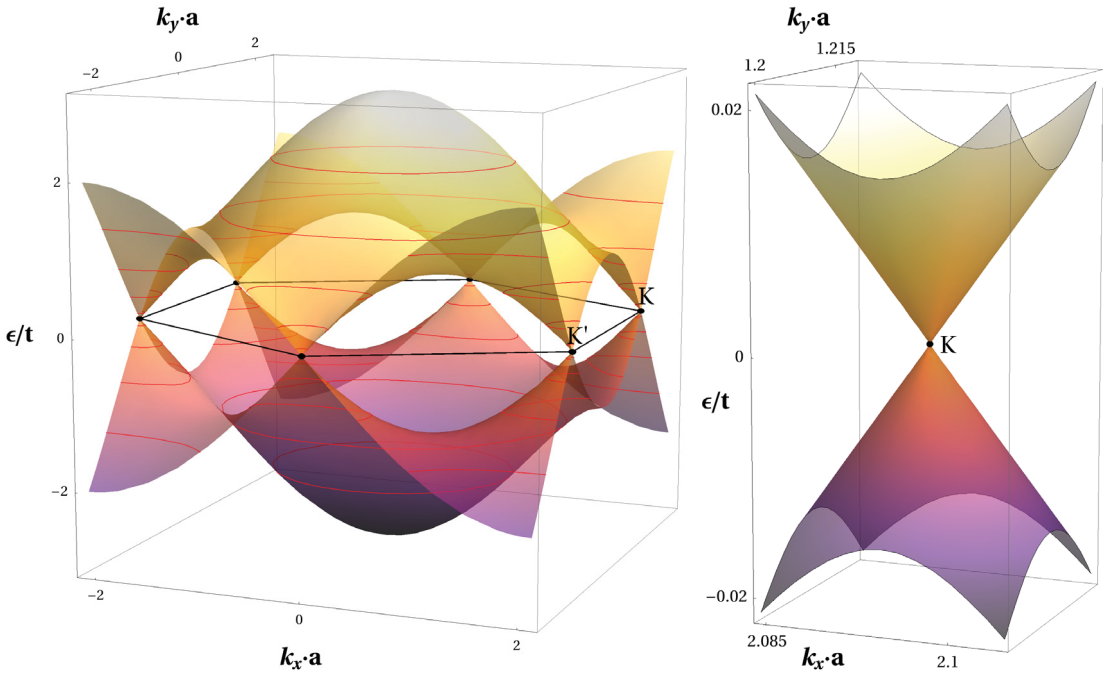

Figure 2.2.: Left: Dispersion-relation of graphene from (2.6). Right: Note the linear, lightlike behavior next to the K-points.

K-points $\mathbf{k} \to \mathbf{k} + \mathbf{K}^{(\prime)}$. The result up to first order is

$$H_T = \frac{3ta}{2} \int d\mathbf{k} \left(\psi^\dagger_{\mathbf{k},\mathbf{K}} \left(\begin{bmatrix} & \frac{(\mathrm{i}+\sqrt{3})}{2} \\ -\frac{(\mathrm{i}-\sqrt{3})}{2} & \end{bmatrix} k_x + \begin{bmatrix} & \frac{(1-\mathrm{i}\sqrt{3})}{2} \\ \frac{(1+\mathrm{i}\sqrt{3})}{2} & \end{bmatrix} k_y \right) \psi_{\mathbf{k},\mathbf{K}} \right.$$
$$\left. + \psi^\dagger_{\mathbf{k},\mathbf{K}'} \left(\begin{bmatrix} & \frac{(\mathrm{i}-\sqrt{3})}{2} \\ -\frac{(\mathrm{i}+\sqrt{3})}{2} & \end{bmatrix} k_x + \begin{bmatrix} & -\frac{(1+\mathrm{i}\sqrt{3})}{2} \\ -\frac{(1-\mathrm{i}\sqrt{3})}{2} & \end{bmatrix} k_y \right) \psi_{\mathbf{k},\mathbf{K}'} \right). \quad (2.7)$$

Rotating $\mathbf{k}$ by $\frac{\pi}{6}$ and transforming into the real space one ends up with the 2D-variant of the Dirac-Weyl equation, which usually describes massless relativistic spin $\frac{1}{2}$ particles [18] and, as we now see, also represents low energy electronic excitations in graphene:

$$H_T = -\mathrm{i}\hbar v_F \int d\mathbf{r} \, (\psi^\dagger_{\mathbf{K}'}(\vec{\mathbf{r}})\sigma \cdot \nabla \psi_{\mathbf{K}'}(\mathbf{r}) - \psi^\dagger_K(\mathbf{r})\sigma^* \cdot \nabla \psi_{\mathbf{K}}(\mathbf{r})),$$

where $v_F = \frac{3ta}{2} \approx 10^6 \frac{\mathrm{m}}{\mathrm{s}}$ is the Fermi-velocity in graphene, $\boldsymbol{\sigma} = [\sigma_x, \sigma_y]^T$, $\sigma_{x,y}$ are the corresponding Pauli matrices operating on the sublattice space and σ^* means the component wise complex conjugate. The dispersion relation around the K-points is thus light-cone shaped, $\epsilon_{\mathbf{k}} = \pm\hbar v_F k$, where $k = |\mathbf{k}|$. Due to the

relativistic behavior of the electrons near the K-points, these are also often called Dirac points. This can be cast into a more convenient notation

$$H_T = -\mathrm{i}\hbar v_F \int d\mathbf{r}\, \boldsymbol{\psi}^\dagger(\mathbf{r}) \left(\sigma_x\tau_z\partial_x + \sigma_y\partial_y\right) \boldsymbol{\psi}(\mathbf{r}). \tag{2.8}$$

Here τ_i, $i \in \{x, y, z\}$, is the Pauli matrix operating on the K-point degree of freedom, also called valley. $\boldsymbol{\psi}(\mathbf{r}) = [\psi_{a,\mathbf{K}}(\mathbf{r}), \psi_{b,\mathbf{K}}(\mathbf{r}), \psi_{a,\mathbf{K}'}(\mathbf{r}), \psi_{b,\mathbf{K}'}(\mathbf{r})]^T$ is now a four component-spinor and we use the abbreviation $\sigma_i \otimes \tau_j = \sigma_i\tau_j$ for the tensorial product[1]. Note that usually both K-points may be treated separately, if one assumes external potentials included into the problem to vary little on the scale of lattice vectors (2.1), and thus having no contributions in their Fourier spectrum close to the edge of the 1.BZ.

Due to the half-filling of the π-bands, see 2.1.1, at $T = 0$ the upper band is empty and the lower band is full. Thus the Fermi-surface exactly corresponds to the both K-points.

We mention for the sake of completeness that including a second neighbor hopping with the energy t' would induce an electron-hole symmetry breaking,

$$\epsilon_{\mathbf{k}} \to \epsilon_{\mathbf{k}} + t'(2\cos(\sqrt{3}k_y a) + 4\cos(\sqrt{3}k_y a/2)\cos(3k_x a/2)),$$

which we will neglect though, since $t \gg t' \approx 0.1\,\mathrm{eV}$.

Note that it is also straightforward to include some sublattice asymmetry

$$H_g = \sum_i \left(M_a a_i^\dagger a_i + M_b b_i^\dagger b_i\right)$$

into the calculations above. Without loss of generality one may set $M_a = M = -M_b$. The effect on the quasi-particle spectrum would be that of an effective mass:

$$H_T \to H_T + M \int d\mathbf{r}\, \boldsymbol{\psi}(\mathbf{r})^\dagger \sigma_z \boldsymbol{\psi}(\mathbf{r}). \tag{2.9}$$

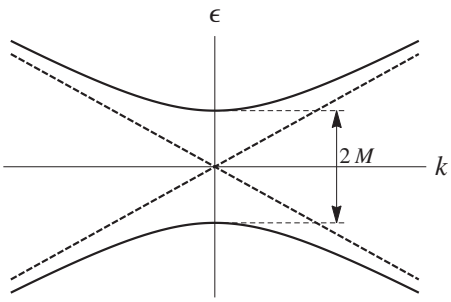

Figure 2.3.: Qualitative band structure in the vicinity of a K-point with and without (dashed) a gap.

This may be realized by substrate-effects, see [19] and [20] for theoretical prediction and experimental realization. The corresponding spectrum is easily calculated to be

$$\epsilon_{\mathbf{k}} = \pm\sqrt{(\hbar v_F k)^2 + M^2}.$$

[1] Note that in this sense one always should read $\sigma_i = \sigma_i \otimes \mathrm{id}_\tau$.

Obviously (2.9) is translational invariant in the graphene plane, since it commutes with ∂_x and ∂_y. We also note that (2.9) is rotationally invariant by means of the transformation

$$H_T(\phi, r) \to U_\theta^\dagger H_T(\phi, r) U_\theta = H_T(\phi + \theta, r), \quad U_\theta = \begin{bmatrix} e^{i\theta} & \\ & 1 \end{bmatrix}.$$

2.1.3 Effects of Spin-Orbit Coupling

So far the spin was neglected, since it was conserved by Hamiltonian in the tight-binding picture ($[H, s_z] = 0$). It turns out, however, that there are numerous effects, which may lift this degeneracy. These interactions enable a rich physics.

In 2005 it was shown [12] that at graphene ribbon boundaries edge states are induced. These carry counter propagating currents of spin filtered electrons. The spin is locked to the direction of propagation. This configuration is time reversal invariant, since under time reversal the spin of an electron would change as well as its direction of propagation. This phenomenon became popular under the name quantum-spin-Hall-effect[2] and encouraged the research on topological insulators, which support edge states and spin selective currents related to them at boundaries between topologically distinct phases. We will see that also in circular quantum dots in the presence of spin-orbit coupling spin selective currents are induced.

The intrinsic spin-orbit coupling (SOC) is due to a relativistic effect, which adds

$$H_{so} = \frac{\hbar}{4m_e^2 c^2} \mathbf{s} \cdot (\nabla V \times \mathbf{p}),$$

$\mathbf{s} = \left[s_x, s_y, s_z\right]^T$, to the one particle Schrödinger equation with any external potential V [12]. Here s_i, $i \in \{x, y, z\}$, is the Pauli matrix operating on the spin degree of freedom.

In case of graphene V is generated by the microscopic configuration of a graphene sample, which is usually not free standing, but located on a substrate and under influence of external fields, curvature and impurity coverings. Interactions with the σ-bonds, connecting neighboring lattice sites, also take place. This results in an additional term of the low-energy Hamiltonian (2.8), [12],

$$H_T \to H_T + M_{so} \int d\mathbf{r}\, \boldsymbol{\psi}^\dagger(\mathbf{r}) \sigma_z s_z \tau_z \boldsymbol{\psi}(\mathbf{r}). \tag{2.10}$$

[2]Note that the regular quantum-Hall-effect does not obey time-reversal symmetry due to presence of magnetic fields. Both spins are propagating in the same direction.

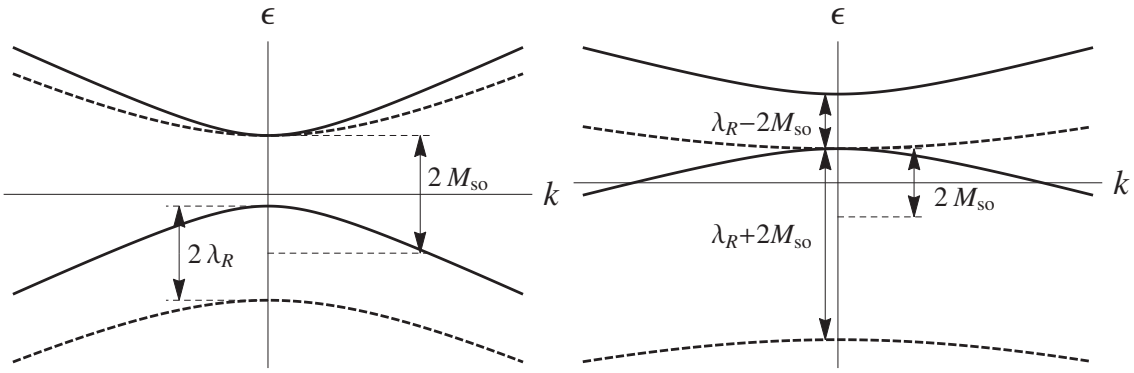

Figure 2.4.: Dispersion-relation of graphene from (2.13). Left: $|\lambda_R| < M_{so}$, Right: $|\lambda_R| > M_{so}$.

Note that ψ is now an eight-component spinor, which additionally includes the spin-degree of freedom. This Hamiltonian corresponds to a gap, which changes sign, depending on spin and valley.

Another class of SOC-effects, the so-called Rashba-SOC, arises through a breaking of symmetry normal to a two dimensional system [21], which gives an effective contribution

$$H_R = \lambda_R(\mathbf{s} \times \mathbf{p}) \cdot \mathbf{e}_z,$$

where $\mathbf{e}_z$ is the z-direction unit vector and λ_R is the so-called Rashba-coupling. Its magnitude is tunable by the magnitude of symmetry breaking, i.e. one may enhance it by applying a electric field normal to the plane of movement of the electrons.

One may achieve this on graphene e.g. by applying an electric field normal to the plane or by curvature [22]. The resulting part of the Hamiltonian one may calculate to be

$$H_T \to H_T + \frac{\lambda_R}{2} \int d\mathbf{r}\, \boldsymbol{\psi}^\dagger(\mathbf{r})(\sigma_x s_y \tau_z - \sigma_y s_x)\boldsymbol{\psi}(\mathbf{r}). \tag{2.11}$$

In contrast to the intrinsic effects Rashba-SOC will break electron-hole symmetry of the quasi-particle spectrum. However, the valley-degeneracy is still present, since the right side of (2.11) only depends on τ_z and thus $[H_T, \tau_z] = 0$.

Taking all SOC-effects into account one ends up with the Hamiltonian

$$H_T = \int d\mathbf{r}\, \boldsymbol{\psi}^\dagger(\mathbf{r}) \Big(-\mathrm{i}\hbar v_F(\tau_z \sigma_x \partial_x + \sigma_y \partial_y) + \tau_z s_z \sigma_z M_{so} + \frac{\lambda_R}{2}(\sigma_x s_y \tau_z - \sigma_y s_x) \Big) \boldsymbol{\psi}(\mathbf{r}) \tag{2.12}$$

whose eigenstates are represented by four valley-degenerate bands,

$$\begin{aligned} \epsilon^{-}_{\mathbf{k}} - \tfrac{\lambda_R}{2} &= \pm\sqrt{(\hbar v_F k)^2 + (M_{so} - \tfrac{\lambda_R}{2})^2} \text{ and} \\ \epsilon^{+}_{\mathbf{k}} + \tfrac{\lambda_R}{2} &= \pm\sqrt{(\hbar v_F k)^2 + (M_{so} + \tfrac{\lambda_R}{2})^2}, \end{aligned} \tag{2.13}$$

see fig. 2.4, and have no definite spin. Notably $\lambda_R \geq 2M_{so}$ would close the gap, thus the contributions due to M_{so} and λ_R are in competition for the possibility of a gap. Note also that for $t \gg \hbar v_F k \gg \max(\lambda_R, M_{so})$ the quasi-particles still have a light-like dispersion relation.

There are various numerical estimates for M_{so} generated due to spin-orbit effects present in isolated C-atoms. Using 2nd-order perturbation-theory it was shown by [9] and [23] that the SOC due to the intrinsic effects is ranging from 0.2 K to 0.01 K. In this context one speaks of intrinsic-SOC. Note that the effect due to this intrinsic effects is tiny compared to the energy scale of the system $t \approx 32 \times 10^3$ K, which would make its effects unobservable. However, by introducing a number of adatoms with a strong intrinsic SOC one may enhance the M_{so} [10]. Note that adatoms also introduce a local distortion of graphene, which would turn the interaction between the p- and s-orbitals into a first order process in the sense of perturbation theory [24]. Attention has to be paid to the possibility of simultaneous increasing of λ_R and thus closing of the gap again, see for instance [25] and [26] for theoretical predictions and experimental measurements with Au adatoms. It was predicted in [10] that using Te or In deposited on the surface of graphene, one may tune M_{so} over a large range, depending on the surface coverage (number of adatoms per unit cell) of these impurities. For instance, at 7% coverage one may achieve up to 25 meV~300 K for M_{so}, while simultaneously the Rashba coupling remains moderate. Experimental realization also include hydrogenated graphene with M_{so} enhanced by ~1000 compared to clean, freestanding graphene [24].

Different methods for varying the Rashba-SOC are, e.g by electric fields normal to the plane, as mentioned above, or curvature, see [9] and [23]. Typical estimates are $\lambda_R \approx 0.13$K at an electric field of $E \sim \frac{50\,\mathrm{V}}{300\,\mathrm{nm}}$. Note that effects of curvature and electric fields will add to each other.

Using a combination of all these procedures one may tune graphene to a wide range of regimes, thus allowing experimental testing of our calculations below.

2.2 Introduction to Criticality of Relativistic Electrons

The relativistic hydrogen problem was first treated by Dirac himself [27], [28] and thereafter by numerous authors (for a nice review cf. [29] and [13]). He managed to solve the corresponding static equation,

$$E\psi = \left(-i\hbar c \sum_{i=1}^{3} \alpha^i \partial_i + mc^2\alpha^0 - \frac{Ze^2}{r}\right)\psi \tag{2.14}$$

where α^i is a set of 4×4 matrices satisfying $\{\alpha^i, \alpha^j\} = 2\delta_{i,j}$. The lowest bound level (bound means $|\epsilon| < m_e c^2$, which corresponds to wave functions decaying as $e^{-|\kappa|r}$ for $r \to \infty$) was found to be

$$\frac{\epsilon_g}{m_e c^2} = \sqrt{1-\zeta^2}, \quad \zeta = \frac{Ze^2}{\hbar c} \approx \frac{Z}{137}.$$

Note that ϵ_g becomes purely imaginary once $Z > 137$. It turns out that any wave function in the limit $r \to 0$ then also behaves like

$$\psi \propto r^{\sqrt{1-\zeta^2}},$$

which makes it impossible to impose proper boundary-conditions, since the function does not converge. Proper boundary conditions are necessary to establish the hermiticity of H, thus it becomes non hermitian in this limit. This is the popular "falling to the center" phenomenon. The intuition behind this is that once a core gets charged above $Z \sim 137$ any electron attracted by it will collapse into the core, accumulating an infinite phase, thus reducing the effective charge to a value $Z < 137$, making it sub-critical again.

This problem may be cured by observing that a true physical charge never is point-like, e.g [29]. For instance, any atomic nucleus has an extent of the order of $\sim$ pm. Taking this into account mathematically means to introduce additional boundary conditions at $r = R$, where R has to be chosen appropriately small, i.e. by regularizing the potential. For instance, one may introduce a cutoff for the potential at $r < R$.

This enables one to tune the core charge to as big as $Z = Z_{cr} \approx 170$, if one regularizes the potential on a length scale corresponding to an atomic nucleus. Then the corresponding ground level energy would reach the negative-energy continuum, $\epsilon < -mc^2$, and become a Fano resonance [30]. One speaks in this case of "criticality" of the system. The wave function of the critical state consists of free wave functions from the negative continuum with a bound state

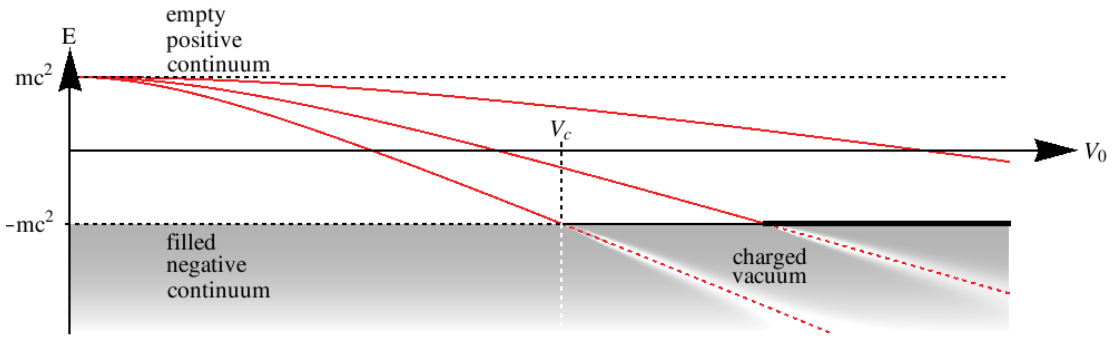

Figure 2.5.: Qualitative relativistic energy spectrum of a general binding potential with some coupling parameter V_0. V_c denotes the critical coupling, where the lowest bound level may cross the boundary to the lower continuum.

admixture forming a state of finite width, [13], where it was also shown that the corresponding energy behaves like $-\epsilon - mc^2 \propto (Z - Z_{cr})$ and the broadening of the resonance $\Gamma \propto (Z - Z_{cr})^2$. The bound state admixture distorts the continuum wave functions around the nucleus in the real space, which results in a polarized vacuum. This situation is depicted schematically in fig. 2.5. Also this state may capture an electron thus emmiting a positron, which may be detected.

Unfortunately the experimental evidence for this is hard to achieve since there are no stable nuclei charged as high as $170e$. Attempts were made to create a quasi-molecule with sufficient charge by colliding uranium nuclei [13]. So far no positron emission was observed. We will see in the next section, however, that similar physics was predicted and realized in graphene.

2.3 A Single, Charged Impurity in Graphene

The task would now consist in solving the one-particle version of (2.8) focusing on one single K-point with additional Coulomb potential and mass included:

$$0 = \begin{bmatrix} -\frac{\alpha}{r} - \epsilon + M & -\mathrm{i}(\partial_x - \mathrm{i}\partial_y) \\ -\mathrm{i}(\partial_x + \mathrm{i}\partial_y) & -\frac{\alpha}{r} - \epsilon - M \end{bmatrix} \begin{bmatrix} \psi_a \\ \psi_b \end{bmatrix} = (H_T + V - \epsilon)\boldsymbol{\psi} = (H - E)\boldsymbol{\psi}. \tag{2.15}$$

Here we set

$$\frac{\epsilon}{\hbar v_F} \to \epsilon, \quad \frac{M}{\hbar v_F} \to M \text{ and } \alpha = \frac{Ze^2}{\hbar v_F}. \tag{2.16}$$

Note that now M has the unit of inverse length, and thus may serve us as a length scale.

This problem has already been solved in numerous publications, e.g. [14], [31] and [32]. We will give a brief sketch of the solution.

First of all, one may easily check that $[H, L] = 0$, where $L = -\mathrm{i}\partial_\phi + \frac{1}{2}\sigma_z$ is the total angular momentum operator. This is true for all polar potentials. Obviously one may then separate the radial and angular coordinates by expressing $\boldsymbol{\psi}$ in terms of eigenstates of L:

$$\begin{bmatrix}\psi_a\\ \psi_b\end{bmatrix} = \begin{bmatrix}\mathrm{e}^{\mathrm{i}m\phi} f_a(r)\\ \mathrm{i}\mathrm{e}^{\mathrm{i}(m+1)\phi} f_b(r)\end{bmatrix}.$$

Here $m \in \mathbb{Z}$ to fulfill the periodic boundary condition $\boldsymbol{\psi}(r, \pi) = \boldsymbol{\psi}(r, -\pi)$. Using this and switching to polar coordinates one ends up with the following coupled equations for $f_{(a,b)}$:

$$\begin{aligned}(\epsilon + M + \frac{\alpha}{r}) f_{b,m} &= (-\partial_r + \frac{m}{r}) f_{a,m}\,,\\ (\epsilon - M + \frac{\alpha}{r}) f_{a,m} &= -(\partial_r + \frac{m+1}{r}) f_{b,m}.\end{aligned} \tag{2.17}$$

One may already observe that the asymptotic solutions at $r \to 0$ are $\propto r^{\pm\gamma - \frac{1}{2}}$, $\gamma = \sqrt{(m - \frac{1}{2})^2 - \alpha^2}$. Note that for $m \in \{0, 1\}$ γ becomes imaginary if $\alpha > \frac{1}{2}$. This hints at some critical behavior for "large" charges since it is then not possible to establish $|\psi| \xrightarrow{r\to 0} 0$.

After some calculations one may show that the solution of this equation is

$$\begin{aligned}f_{\sigma_z,m,n}(r) = {} & \sqrt{(M + \sigma_z\epsilon)}\mathrm{e}^{-ur}(2ur)^{\gamma-\frac{1}{2}}\times\\ & \left({}_1F_1(\gamma - \tfrac{\alpha\epsilon}{u}; 1 + 2\gamma; 2ur) + \sigma_z \frac{\gamma - \frac{\alpha\epsilon}{u}}{m + \frac{1}{2} + \frac{\alpha M}{u}}\, {}_1F_1(1 + \gamma - \tfrac{\alpha\epsilon}{u}; 1 + 2\gamma; 2ur)\right),\end{aligned} \tag{2.18}$$

(remember that σ_z operates on the sub-lattice space) where $u = \sqrt{|M^2 - \epsilon^2|}$,

$${}_1F_1(\mu; \nu; x) = 1 + \frac{\mu x}{\nu 1!} + \frac{\mu(\mu+1)x^2}{\nu(\nu+1)2!} + \dots$$

is the corresponding degenerate hypergeometric function [33]. Unfortunately (2.18) diverges for $r \to \infty$. Note, however, that ${}_1F_1(\mu; \nu; x)$ reduce to Polynomials for $-\mu = n \in \mathbb{N}_0$:

$$\binom{n+\alpha}{n} {}_1F_1(-n; \alpha; x) = L_n^\alpha(x)$$

with the corresponding Laguerre polynomials L_n^α [33]. This now allows to select solutions corresponding to bound levels,

$$\gamma - \frac{\alpha\epsilon}{u} = -n \Rightarrow \epsilon_{m,n} = \text{sign}(\alpha) M \sqrt{\frac{(n+\gamma)^2}{(n+\gamma)^2 + \alpha^2}}.$$

The bound state wave functions then are

$$f_{\sigma_z,m,n}(r) = \sqrt{(M + \sigma_z \epsilon_{m,n})} \mathrm{e}^{-ur} (2ur)^{\gamma - \frac{1}{2}} \times \left({}_1F_1(-n; 1+2\gamma; 2ur) - \sigma_z \frac{n}{m + \frac{1}{2} + \sqrt{\alpha^2 + (n+\gamma)^2}} \, {}_1F_1(1-n; 1+2\gamma; 2ur) \right). \tag{2.19}$$

Note the prefactor before the second term inside the brackets. It imposes $n \in \mathbb{N}_0$ for $m \geq 0$, $n \in \mathbb{N}$ for $m < 0$, since $\sqrt{\alpha^2 + \gamma^2} = |m + \frac{1}{2}|$.

$m = 0$, $n = 0$ corresponds to the minimal absolute energy

$$\epsilon = 2\text{sign}(\alpha) M \gamma. \tag{2.20}$$

Similarly to the three dimensional case it becomes imaginary for $\alpha > \frac{1}{2}$. In general one may show for potentials $\propto r^{-s}$ that these characteristics always occur for $s > 1$ and never for $s < 1$, turning $s = 1$ into a boundary with mixed behavior [31].

Again, this problem may be circumvented for a larger range of α by imposing different boundary conditions. This was for instance performed in [32], where

$$V = -\frac{\alpha}{r} \to -\frac{\alpha}{\max(r, R)}.$$

Imposing continuity at $r = R$ it was found

$$\lim_{R \to 0} \alpha_c \approx \frac{1}{2} + \frac{\pi^2}{\ln^2(MR)}$$

for the critical coupling.

Note that the charge necessary to drive the system into a critical state now is of order $Z \approx 1$. This is due to the fact that the light speed-equivalent in graphene, the Fermi velocity v_F, is about 100 times smaller than c, which reduces the fine structure constant equivalent by the same factor. This makes it much easier to realize supercritical configurations experimentally, as was shown in [7] recently. Their approach consisted in clustering together several Ca adatoms. Although each of them was charged subcriticaly, the total charge may exceed the critical value. The scale of regularization then is the cluster-size.

3 Two Center Problem in Graphene

As we discussed in the introduction, critical effects may occur if Dirac particles get bound by a sufficiently deep potential, for instance caused by a charge center. In the following sections, we will investigate how this situation would change in a case where we have two centers which may be carrying either equal charge, or equal absolute charge with opposite prefactor.

It is possible to realize such situations experimentally [7], as we mentioned above, where adatoms were clustered on a graphene sheet in a controlled way. We note that depending on the electronegativity of the used atoms one may create positively or negatively charged clusters. Also tunable potentials may be created by the use of the so-called conical singularities, consisting of wrinkles of the graphene sheet [34]. The potentials in this case are induced by the curvature of the sheet. We would like to mention again that all of the following calculations hold for the topological insulators and molecular graphene.

3.1 Equal Charges - The LCAO Approach

In this section we will discuss the two center problem in graphene, which means the case, where two equal charges are located at $\mathbf{c}_\pm = [\pm a, 0]^T$. Note that the alignment of the centers w.r.t. the origin is arbitrary due to translational and rotational invariance of the free, massive Dirac Hamiltonian (2.9), and we thus may make a choice convenient for latter calculations.

This problem was dealt with in a recent publication [35] already by different procedures. In what follows we will investigate this system by means of the linear combination of atomic orbitals (LCAO). One may see [36] for the general theory and [37] for the application to the 3D two center Dirac problem, i.e. (2.14) with an additional Coulomb potential centered at some different position w.r.t. the first one.

Take a set of states, which depend on a set of parameters $\mathbf{v}$, $|i(\mathbf{v})\rangle$, usually these are naturally given by the problem at hand, then expand the full Hamiltonian in the subspace spanned by $|i(\mathbf{v})\rangle$, find the eigenenergies and minimize these

with respect to the parameters $\mathbf{v}$. In our case we use superpositions of one-center Coulomb problem ground state solutions to find the bound states of the two-center problem.

Focusing on the K-point $\mathbf{K}$ the corresponding Hamiltonian reads

$$H = H_T + V^{tc} = -\mathrm{i}\boldsymbol{\sigma}\cdot\nabla + M\sigma_z - \alpha\left(\frac{1}{r_+} + \frac{1}{r_-}\right), \tag{3.1}$$

where the first two parts in the rightmost term correspond to H_T, $r_\pm = |\mathbf{r} - \mathbf{c}_\pm|$, $\mathbf{c}_\pm = [\pm a, 0]^T$, please also see appendix A, and we use the units (2.16),

$$(\hbar v_F)^{-1}[M, \epsilon]^T \to [M, \epsilon]^T$$

for mass and energy.

Due to the fact that asymptotically the potential has a $1/r$ behavior, we qualitatively expect the same physics as in the one center case, see 2.3, which means that we should encounter critical behavior, if the total charge $\zeta = 2\alpha$ exceeds a threshold value. However, the magnitude of this value should be strongly dependent on the distance $R = 2a$ between the centers. Note that separating the charge into two different centers in itself is a regularization, which usually is the procedure of turning a mathematical problem of a point-like centers into a more physical situation of smeared out charges. Thus it should be possible to drive the total charge $\zeta = 2\alpha$ above 0.5 before the system becomes critical.

As in [37], we consider two wave functions, centered around one of the centers, to be a ground state with respect to some effective charge Q, which will be our parameter with respect to which the energy is to be minimized. These will span the subspace in which the Hamiltonian is expanded and $\mathbf{v} = Q$.

The Hamiltonian of the full problem can be cast into the form

$$H = H_T - Q\left(\frac{1}{r_+} + \frac{1}{r_-}\right) - \delta\alpha\left(\frac{1}{r_+} + \frac{1}{r_-}\right), \tag{3.2}$$

where H_T is the free (kinetic) part of the Hamiltonian (2.8) and $\delta\alpha = \alpha - Q$. We use the normalized wave functions [31]

$$\boldsymbol{\psi}^Q_\pm(r_\pm) = \frac{u_Q}{\sqrt{4\pi M\Gamma(2\gamma_Q + 1)}}\begin{bmatrix}\sqrt{M + \epsilon_{g,Q}} \\ \mathrm{i}\sqrt{M - \epsilon_{g,Q}}\mathrm{e}^{\mathrm{i}\phi_\pm}\end{bmatrix}\mathrm{e}^{-u_Q r_\pm}(2u_Q r_\pm)^{\gamma_Q - \frac{1}{2}} = \langle x|\pm\rangle$$

which obey

$$(T - \frac{Q}{r_\pm})\psi^Q_g(r_\pm) = \epsilon_{g,Q}\psi^Q_g(r_\pm), \tag{3.3}$$

where

$$\epsilon_{g,Q} = \text{sign}(Q)M\sqrt{1-4Q^2},\ \ \gamma_Q = \sqrt{\frac{1}{4}-Q^2},\ \ u_Q = 2MQ$$

and $r_\pm = |\mathbf{r} - \mathbf{c}_\pm|$ is the distance to the centers and $\phi_\pm$ is the angle enclosed $\mathbf{r} - \mathbf{c}_\pm$ and the x-axis, please check appendix A for further explanations.

Expanding the Hamiltonian in $|\pm\rangle$ gives:

$$\begin{bmatrix} \epsilon_{g,Q} - \langle +|\frac{\delta\alpha}{r_+} + \frac{\alpha}{r_-}|+\rangle & \epsilon_{g,Q}\langle +|-\rangle - \langle +|\frac{\delta\alpha}{r_+} + \frac{\alpha}{r_-}|-\rangle \\ \epsilon_{g,Q}\langle -|+\rangle - \langle -|\frac{\delta\alpha}{r_+} + \frac{\alpha}{r_-}|+\rangle & \epsilon_{g,Q} - \langle -|\frac{\delta\alpha_-}{r_-} + \frac{\alpha}{r_+}|-\rangle \end{bmatrix}\begin{bmatrix} v_+ \\ v_- \end{bmatrix} = \epsilon\begin{bmatrix} 1 & \langle +|-\rangle \\ \langle -|+\rangle & 1 \end{bmatrix}\begin{bmatrix} v_+ \\ v_- \end{bmatrix}. \tag{3.4}$$

Finding the minimum of ϵ w.r.t. Q will give us an upper bound estimate of the actual ground state energy, once we have found expressions for the various overlaps. We may already evaluate in polar coordinates

$$A_0 = \langle \pm|\frac{1}{r_\pm}|\pm\rangle = \frac{2Q}{\gamma_Q}.$$

The remaining task is now to calculate the values of $S = \langle +|-\rangle$, $C = \langle \pm|\frac{1}{r_\mp}|\mp\rangle$ and $A = \langle \pm|\frac{1}{r_\mp}|\pm\rangle$ as a function of a, which we will do in elliptic coordinates[1]. Note that one may note simply copy the results obtained in three dimnesions [37], since the volume element of the prolate spheroidal coordinates used there is quite different from what we encounter within simple elliptic coordinates.

3.1.1 Calculation of the Overlaps A, C, S.

We perform the calculation of the overlaps A, C and S [38]. Useful identities will be:

$$\begin{aligned} \int_{-1}^{1} d\nu(1-\tfrac{\nu^2}{\mu^2})^\Omega\sqrt{1-\nu^2} &= \frac{\pi}{2}F\left(\frac{1}{2},-\Omega;2;\mu^{-2}\right), \\ \int_{-1}^{1} d\nu\frac{(1-\frac{\nu^2}{\mu^2})^\Omega}{\sqrt{1-\nu^2}} &= \pi F\left(\frac{1}{2},-\Omega;1;\mu^{-2}\right), \end{aligned} \tag{3.5}$$

see [39],

$$\int_{-1}^{1} dx\frac{\mathrm{e}^{-px}x^n}{\sqrt{1-x^2}} = \pi(-1)^n\partial_p^n I_0(p) = f^I(n,p), \tag{3.6}$$

[1] Please check appendix A.

see [33], and

$$\int_1^\infty dx \frac{x^\alpha e^{-px}}{\sqrt{x^2-1}} = \\ \frac{1}{2}B\left(\tfrac{1}{2},-\tfrac{\alpha}{2}\right){}_1F_2\left(\tfrac{\alpha+1}{2};\tfrac{1}{2},\tfrac{\alpha}{2}+1;\tfrac{p^2}{4}\right) - \frac{p}{2}B\left(\tfrac{1}{2},-\tfrac{\alpha+1}{2}\right){}_1F_2\left(\tfrac{\alpha+1}{2};\tfrac{3}{2},\tfrac{\alpha+3}{2};\tfrac{p^2}{4}\right) \\ + p^{-a}\Gamma(\alpha){}_1F_2\left(\tfrac{1}{2};\tfrac{1-\alpha}{2},1-\tfrac{\alpha}{2};\tfrac{p^2}{4}\right) = \mathcal{I}(\alpha,p), \tag{3.7}$$

[39] where B is the β-function, I is the corresponding modified Bessel function and Γ, F and ${}_1F_2$ have their usual meanings.

We compute using (A.4)

$$\begin{aligned} S &= \frac{(2u_Q)^{2\gamma_Q}(M+\epsilon_{g,Q})}{8\pi M\Gamma(2\gamma_Q+1)}\int d\mathbf{r}\left(1+\kappa\cos(\phi_+-\phi_-)\right)(r_+r_-)^{\gamma_Q-\frac{1}{2}}\mathrm{e}^{-u_Q(r_++r_-)} \\ &= P_S\int_{\mu=1,\nu=-1}^{\mu=\infty,\nu=1}\frac{d\mu d\nu(\mu^2-\nu^2)}{\sqrt{(\mu^2-1)(1-\nu^2)}}\left(1+\kappa-2\kappa\frac{1-\nu^2}{\mu^2-\nu^2}\right)(\mu^2-\nu^2)^{\gamma_Q-\frac{1}{2}}\mathrm{e}^{-uR\mu} \\ &= P_S\left[(1+\kappa)\int_{\mu=1,\nu=-1}^{\mu=\infty,\nu=1}\frac{d\mu d\nu(\mu^2-\nu^2)^{\gamma_Q+\frac{1}{2}}}{\sqrt{(\mu^2-1)(1-\nu^2)}}\mathrm{e}^{-u_QR\mu}\right. \\ &\qquad\left. -2\kappa\int_{\mu=1,\nu=-1}^{\mu=\infty,\nu=1}\frac{d\mu d\nu(\mu^2-\nu^2)^{\gamma_Q-\frac{1}{2}}\sqrt{(1-\nu^2)}}{\sqrt{\mu^2-1}}\mathrm{e}^{-u_QR\mu}\right] \end{aligned} \tag{3.8}$$

where

$$\kappa = \tfrac{M-\epsilon_{g,Q}}{M+\epsilon_{g,Q}} \text{ and } P_S = \frac{(Ru_Q)^{2\gamma_Q}(M+\epsilon_{g,Q})}{4\pi RM\Gamma(2\gamma_Q+1)}.$$

Note that in (3.8) we neglected $\mathrm{i}\sin(\phi_+-\phi_-)$, stemming from $\exp(\phi_+-\phi_-)$, in the integral due to its antisymmetry ($\mathrm{sign}(\phi_+)=\mathrm{sign}(\phi_-)$). Also, we included a factor two due to integration over both half planes of y, $\mathrm{sign}(y)=\pm1$.

Now we may use (3.5):

$$S = P_S\pi\left[(1+\kappa)\int_{\mu=1}^{\mu=\infty}\frac{d\mu\mu^{2\gamma_Q+1}F\left(\frac{1}{2},-\gamma_Q-\frac{1}{2};1;\mu^{-2}\right)}{\sqrt{\mu^2-1}}\mathrm{e}^{-u_QR\mu}\right.$$
$$\left.-\kappa\int_{\mu=1}^{\mu=\infty}\frac{d\mu\mu^{2\gamma_Q-1}F\left(\frac{1}{2},-\gamma_Q+\frac{1}{2};2;\mu^{-2}\right)}{\sqrt{\mu^2-1}}\mathrm{e}^{-u_QR\mu}\right]. \quad (3.9)$$

The $F(a,b;c;x)$ are convergent for $x=1$, iff $\Re(c)>\Re(a+b)$, [33]. This is the case in the integrals above, since $\gamma_Q\in]0,\frac{1}{2}[$. Thus we may expand F in the hypergeometric series and safely interchange the sum and the integral. Using

$$F(a,b;c;x)=1+\frac{ab}{c1!}x+\frac{a(a+1)b(b+1)}{c(c+1)2!}x^2+\ldots=\sum_{n=1}^{\infty}\frac{(a)_n(b)_n}{(c)_nn!}x^n,$$

where $(k)_n$ is the so-called Pochhammer symbol, $(k)_{n+1}=(k)_n(k+n)$, $(k_0)=1$, and using (3.7) we may write (3.9) as

$$S=\pi P_S\left[(1+\kappa)\sum_{n=0}^{n=\infty}\frac{(\frac{1}{2})_n(-\gamma_Q-\frac{1}{2})_n}{(1)_nn!}\mathcal{I}(2\gamma_Q+1-2n,u_QR)\right.$$
$$\left.-\kappa\sum_{n=0}^{n=\infty}\frac{(\frac{1}{2})_n(-\gamma_Q+\frac{1}{2})_n}{(2)_nn!}\mathcal{I}(2\gamma_Q-1-2n,u_QR)\right]. \quad (3.10)$$

To deal with C we first may write

$$\frac{1}{r_\pm}=\frac{2(\mu\mp\nu)}{R(\mu^2-\nu^2)}.$$

Along the same path as in case of S we then get

$$C=P_C\left[(1+\kappa)\int_{\mu=1,\nu=-1}^{\mu=\infty,\nu=1}\frac{d\mu d\nu\mu(\mu^2-\nu^2)^{\gamma_Q-\frac{1}{2}}}{\sqrt{(\mu^2-1)(1-\nu^2)}}\mathrm{e}^{-u_QR\mu}\right.$$
$$\left.-2\kappa\int_{\mu=1,\nu=-1}^{\mu=\infty,\nu=1}\frac{d\mu d\nu\mu(\mu^2-\nu^2)^{\gamma_Q-\frac{3}{2}}\sqrt{(1-\nu^2)}}{\sqrt{\mu^2-1}}\mathrm{e}^{-u_QR\mu}\right], \quad (3.11)$$

where $P_C = 2P_S/R$ and where we used that integrals including odd powers of ν vanish due to asymmetry. Redoing same steps as before we arrive at

$$C = \pi P_C \Bigg[(1+\kappa) \sum_{n=0}^{n=\infty} \frac{(\frac{1}{2})_n (-\gamma_Q + \frac{1}{2})_n}{(1)_n n!} \mathcal{I}(2\gamma_Q - 2n, u_Q R) \\ -\kappa \sum_{n=0}^{n=\infty} \frac{(\frac{1}{2})_n (-\gamma_Q + \frac{3}{2})_n}{(2)_n n!} \mathcal{I}(2\gamma_Q - 2 - 2n, u_Q R) \Bigg], \quad (3.12)$$

where we again could interchange sum and integral due to the same reasons as before.

The integral A needs a slightly different approach. Focusing on $\langle + | r_-^{-1} | + \rangle$ and using (3.6)

$$\begin{aligned} A =& \frac{(2u_Q R)^{2\gamma_Q}}{4\pi R^2 \Gamma(2\gamma_Q + 1)} \int_{\mu=1,\nu=-1}^{\mu=\infty,\nu=1} \frac{d\mu d\nu (\mu+\nu)^{2\gamma_Q}}{\sqrt{(\mu^2-1)(1-\nu^2)}} \mathrm{e}^{-u_Q R(\mu+\nu)} \\ =& P_A \int_{\mu=1,\nu=-1}^{\mu=\infty,\nu=1} \frac{\mu^{2\gamma_Q} \mathrm{e}^{-u_Q R\mu}}{\sqrt{\mu^2-1}} \sum_{n=0}^{\infty} \frac{(-1)^n (-2\gamma_Q)_n}{\mu^n} \frac{\nu^n \mathrm{e}^{-u_Q R\nu}}{\sqrt{1-\nu^2}} \\ =& P_A \int_{\mu=1}^{\mu=\infty} \sum_{n=0}^{\infty} \frac{(-1)^n (-2\gamma_Q)_n f^I(n, u_Q R) \mu^{2\gamma_Q - n} \mathrm{e}^{-u_Q R\mu}}{\sqrt{\mu^2-1}} \\ =& P_A \sum_{n=0}^{\infty} (-1)^n (-2\gamma_Q)_n f^I(n, u_Q R) \mathcal{I}(2\gamma_Q - n, u_Q R), \end{aligned} \quad (3.13)$$

where

$$P_A = \frac{(u_Q R)^{2\gamma_Q}}{4\pi R^2 \Gamma(2\gamma_Q + 1)}.$$

We now may calculate the integrals to good approximation by truncating the sums in (3.10), (3.12) and (3.13). These results may easily be confirmed by observing that

$$\lim_{R\to 0} S = 1, \quad \lim_{R\to 0} A = A_0 = \lim_{R\to 0} C \quad \text{and} \quad \lim_{R\to\infty} A = \frac{1}{R}, \quad (3.14)$$

since in that limit $|-\rangle \to |+\rangle$. This is indeed the case, as may be seen in fig. 3.1.

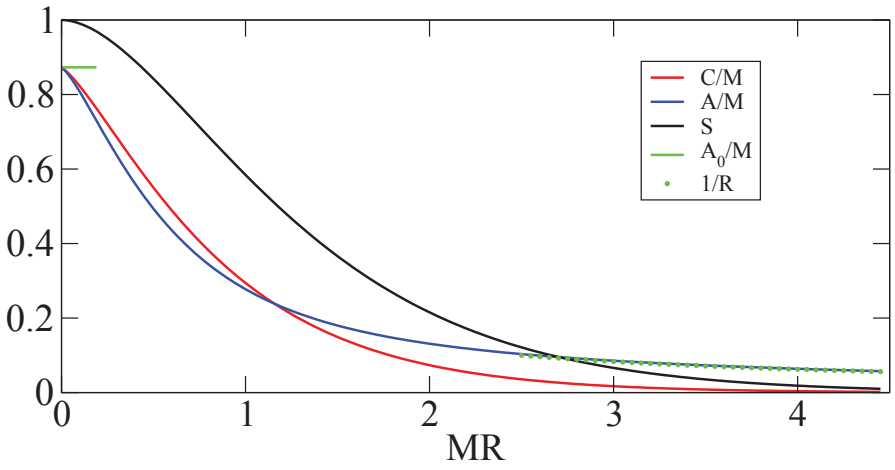

Figure 3.1.: Integrals A, C and S as a function of the two center distance R, $Q = 0.2$, truncation order 10. Note that the results indeed agree with (3.14), as may be seen by comparing the curves to the green line corresponding to A_0 and green dots corresponding to R^{-1}.

3.1.2 Results

Substituting the expressions (3.10), (3.12) and (3.13) calculated in the previous sections into (3.4) one arrives at the expression [38]

$$\det\begin{bmatrix}(\epsilon_{g,Q}-\epsilon)-(\delta\alpha A_0+\alpha A) & (\epsilon_{g,Q}-\epsilon)S-(\delta\alpha+\alpha)C\\ (\epsilon_{g,Q}-\epsilon)S-(\delta\alpha+\alpha)C & (\epsilon_{g,Q}-\epsilon)-(\delta\alpha A_0+\alpha A)\end{bmatrix}=0 \tag{3.15}$$

to be solved for ϵ. The result is then minimized numerically with respect to Q using iterative parabolic interpolation, where we use the sums calculated in the last chapter truncated at some not too small order N, usually $N \sim 10$, see fig. 3.2. Note how the results nicely capture the physics one would expect qualitatively: at large distance of the centers the electron may only be bound at one of them and the other has no effect, while at small distance both centers may be seen as a single center with twice the charge. This is reflected in the dependency of Q_{min} on the distance between the centers, R.

Using this method one may also estimate the distance of both centers at which the system becomes critical, i.e. when the total charge $2\alpha = \zeta > 0.5$, by using the secant method iteratively, see fig. 3.2. The results seem to agree well with [35], see fig. 3.2, who, among other methods, used some asymptotic-matching, which selects putative bound levels by searching for the equality of the logarithmic derivative of the two asymptotic, $r \to 0$ and $r \to \infty$. Obviuosly the critical distance becomes extremely small in the case $\zeta \to 0.5$. This is in agreement with

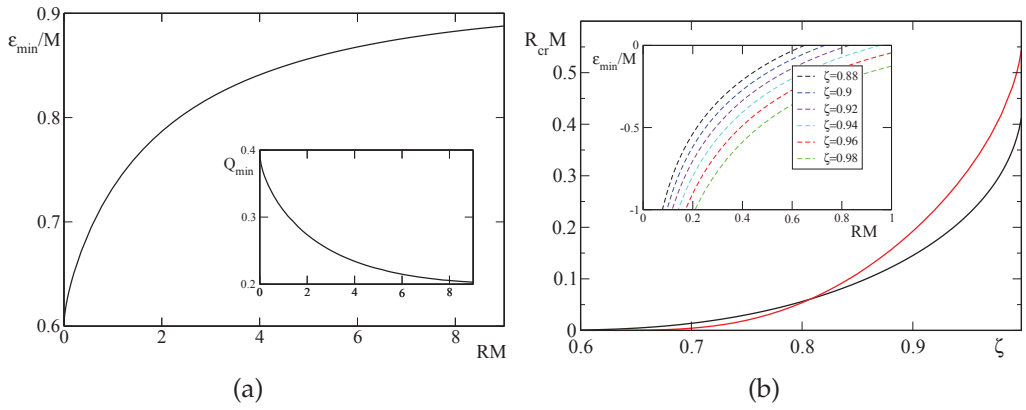

Figure 3.2.: a) Ground state estimate of the two center problem using LCAO as a function of center distance, $\zeta = 0.4$. Inset: the minimizing effective charge Q_{min}. Note: $\epsilon_{g,0.2} = 0.917\,M$, $\epsilon_{g,0.4} = 0.6\,M$. b) Critical distance R_{cr} as a function of the total charge ζ using the LCAO-method (red) and from [35] (black). Inset: estimated energy as a function of the two center distance R for various ζ.

experiments [7], where adatoms hat to be pushed closely together, before the system became critical.

We expect the LCAO method to work best for $\zeta \to 1$, since then the asymptotic behavior of our trial function $\psi_\pm(r_\pm \to 0)$ is close to the exact asymptotic near the centers $\propto r_\pm^{\gamma_\alpha - \frac{1}{2}}$. In this limit, namely, $Q \to 0.5$.

3.2 Dipole Problem

Now we focus on a situation, where we have two charged centers separated by a distance $R = 2a$ with the same absolute charge α but opposite sign, i.e. the total charge of the problem $\zeta = 0$ [40]. It is hard to achieve an intuition, whether bound states may occur or not. This problem was investigated in 3 dimensions in the Schrödinger [41], as well as in the Dirac case [42]. The result was that a critical value of the dipole moment $D = \alpha R$ is necessary for the existence of bound states. In two dimensions it was found [43] in the Schrödinger case that a bound state exist for arbitrary small dipole moments. The solution of the corresponding problem in the two dimensional Dirac case was not yet treated in the literature.

Note that in atomic physics in three dimensions this problem would be highly academical, since highly concentrated negative charges, $Z \sim 130$, necessary to

obtain physics described by us in graphene case, are even harder to achieve that strongly charged positive centers. However, since, as mentioned above, on graphene the effective fine structure constant is much smaller, charges of order $\sim 1e$ are already sufficient to get measurable effects.

The solution of the full dipole problem is very difficult to treat analytically, since no coordinate system can be found, whose coordinate dependencies of the Hamiltonian separate. It turns out, however, that the qualitative behavior of the dipole problem may be explained by means of non relativistic calculations for energies close to the band edge, $\epsilon \to \pm M$. In this limit one may separate the equation in radial and angular components, which may be solved separately. To address the full Dirac problem, we will resort to a numerical diagonalization procedure. Finally we will give some estimates for the scattering behavior in the presence of a dipole impurity.

3.2.1 Model

In analogy to the two center problem we may write the Hamiltonian

$$H = H_T + V^{tc} = -\mathrm{i}\boldsymbol{\sigma} \cdot \nabla + M\sigma_z + \alpha\left(\frac{1}{r_+} - \frac{1}{r_-}\right). \tag{3.16}$$

Again, we have a free choice of our center positions.

This equation is very difficult to solve by analytical means, because there exists no coordinate system, whose coordinate dependencies of the Hamiltonian separate. However, one should be able to capture the qualitative behavior through the dominant $r \to \infty$ asymptotics of V^{tc}. Using the multipole expansion one quickly computes

$$\lim_{r\to\infty} V^{tc}(\mathbf{r}) = -\frac{2\alpha a\cos(\phi)}{r^2} = -\frac{D\cos(\phi)}{r^2} = V^{pd}(\mathbf{r}).$$

One may see V^{pd} as a point-like dipole, $\alpha = D/R$ and $R \to 0$. We note that this potential is highly diverging at $r \to 0$, which requires some regularization. This may be done by means of a cutoff at $r_0 \approx a$, which represents the small scale structure of the problem, see fig. 3.3.

We find an antisymmetry of the Hamiltonian (3.16) w.r.t. the transformation

$$\mathcal{R}_x\sigma_x H\mathcal{R}_x\sigma_x = -H, \tag{3.17}$$

where $\mathcal{R}_x$ inverts the x-coordinate. This represents the electron-hole symmetry of the system, since for any state with the energy ϵ we may find a state with the energy $-\epsilon$. This antisymmetry holds for both V^{tc}, as well as V^{pd}. In fact, it will hold for any potential V that obeys $V(x, y) = -V(-x, y)$.

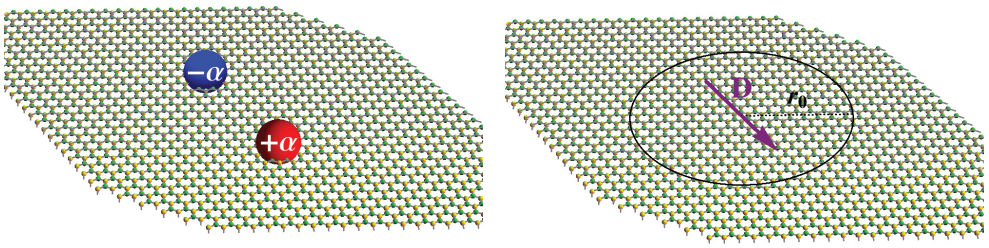

Figure 3.3.: The true physical situation (left) and the corresponding model (right) of a dipole immersed on a graphene sheet.

3.2.2 Nonrelativistic Limit - Point-like Dipole

As mentioned above, we may for now limit ourselves to energies close to a band edge, e.g. $\epsilon \approx -M$. Note that the opposite case $\epsilon \approx M$ is also captured by these calculations, because of the antisymmetry (3.17). Putting $-\epsilon - M = \eta \ll M$, i.e. focusing on weakly bound states, the corresponding Dirac equation reads

$$\begin{bmatrix} 2M + V^{pd} & -\mathrm{i}(\partial_x - \mathrm{i}\partial_y) \\ -\mathrm{i}(\partial_x + \mathrm{i}\partial_y) & -\eta + V^{pd} \end{bmatrix} \begin{bmatrix} f \\ g \end{bmatrix} = 0.$$

Now we regularize the potential by inserting boundary conditions at $r = r_0$, where we choose r_0 such that $V^{pd}(r_0) \ll M$. Remembering the definition of our units (2.16), $\hbar v_F \sim at$ (2.8), and choosing a reasonably large gap $M \approx 0.1\,t$ [20] and $\alpha \approx 1$ we get

$$V^{pd}(r_0) \sim \frac{\alpha}{r_0} \approx \frac{1}{r_0} \quad \text{and} \quad M \approx \frac{0.1t}{ta} = \frac{0.1}{a}$$

and thus

$$r_0 \gg 10a.$$

This constrain should still allow a reasonable experimental realization.

Using this we may neglect V^{pd} w.r.t. $2M$. We now arrive at a highly simplified set of equations,

$$\begin{aligned} &2Mf - \mathrm{i}(\partial_x - \mathrm{i}\partial_y)g = 0 \quad \text{and} \\ &-\mathrm{i}(\partial_x + \mathrm{i}\partial_y)f + (-\eta + V^{pd})g = 0, \end{aligned}$$

where we call f the small and g the large component of the spinor[2]. By substitution we may easily reduce this system to a 2nd order equation for g:

$$0 = \left(\Delta + 2M(-\eta + V^{pd})\right) g, \tag{3.18}$$

or equivalently, in polar coordinates

$$(-\partial_\phi^2 + 2MD\cos(\phi))g = (r^2\partial_r^2 + r\partial_r - 2M\eta r^2)g.$$

for which we seek solutions respecting boundary conditions

$$i)\ g(\pi, r) = g(-\pi, r),\ \ ii)\ g(r_0, \phi) = 0 \ \text{ and } \ iii)\ \lim_{r\to\infty} g(\phi, r) = 0. \tag{3.19}$$

These conditions correspond to an infinitely repulsive circular core with the radius r_0.

Obviously this boundary-value problem may be separated in an angular and a radial part. Using $g(r, \phi) = \Phi(\phi)R(r)$ we may write

$$\begin{aligned} &\Phi'' + (A - 2MD\cos(\phi))\Phi = 0, \\ &r^2R'' + rR' - (A + 2M\eta r^2)R = 0 \end{aligned} \tag{3.20}$$

where A is the separation constant.

By the substitution $\phi = 2u$, $\Phi(2u) = \tilde{\Phi}(u)$ in the angular part we arrive at the equation

$$\tilde{\Phi}'' + (4A - 8MD\cos(2u))\tilde{\Phi} = 0.$$

which is nothing else than the popular Mathieu equation (B.1). Therefore, we may conclude that

$$\Phi_{\pm,j}(\phi) = \begin{cases} ce_{2j}\left(\frac{\phi}{2}, a_{2j}(d)\right), & A_{+,j} = \frac{a_{2j}(d)}{4}, \quad j \in \mathbb{N}_0 \\ se_{2j}\left(\frac{\phi}{2}, b_{2j}(d)\right), & A_{-,j} = \frac{b_{2j}(d)}{4} \quad j \in \mathbb{N} \end{cases}, \tag{3.21}$$

where we defined $d = 4MD$ and a_{2j} are the Mathieu characteristic values. We mention that the solutions *ce* are cos-like, even, while *ce* are sin-like, odd solutions. In fact, if $D \to 0$, $ce_j(\phi, d) \to \cos(j\phi)$, $se_j(\phi, d) \to \sin(j\phi)$ and $a_j = j^2 = b_j$.

This fixes any possible choices of the separation constant. Note that we skipped any solution of order $2j + 1$, $j \in \mathbb{N}_0$, due to boundary conditions (3.19) *i*).

[2]Note that $f \propto \partial g/2M$.

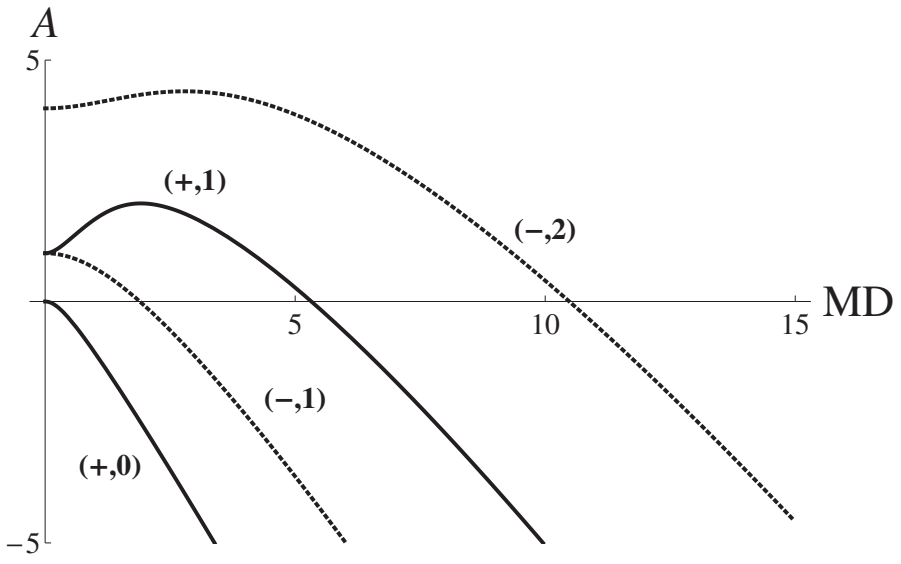

Figure 3.4.: Values of the separation constant $A_{\boldsymbol{\kappa}}$.

The radial part is nothing other than the modified Bessel equation (C.5). We may simply read off the solution from (C.4):

$$R(r) = a_K K_{\sqrt{A}}(\sqrt{2M\eta}r) + a_I I_{\sqrt{A}}(\sqrt{2M\eta}r),$$

where K_ν and I_ν are the corresponding modified Bessel functions. The boundary condition (3.19) *iii*) then enforces $a_I = 0$ since $|I_\nu|$ is exponentially growing for any $\nu \in \mathbb{C}$.

Combining both parts, angular and radial, one arrives at solutions

$$\begin{aligned} g_{+,j}(\phi, r) &= K_{\sqrt{A_{j,+}}}(\sqrt{2M\eta}r)\, ce_{2j}\left(\tfrac{\phi}{2}, a_{2j}(d)\right), \quad j \in \mathbb{N}_0, \\ g_{-,j}(\phi, r) &= K_{\sqrt{A_{j,-}}}(\sqrt{2M\eta}r)\, se_{2j}\left(\tfrac{\phi}{2}, b_{2j}(d)\right), \quad j \in \mathbb{N}, \end{aligned} \tag{3.22}$$

which still have to fulfill (3.19) *ii*). For convenience we now introduce the multiindex $\boldsymbol{\kappa}$, which runs over all valid values of $(\pm, j)$.

We note that $K_\nu(x) \neq 0$ for $\nu \in \mathbb{R}$, thus to fulfill the boundary conditions at hand it is required $\nu \in \mathbb{C}$. Observing possible values for A in (3.21) we conclude that a set of levels may appear when $a_{2j}(d) < 0$ or $b_{2j}(d) < 0$. This happens at certain critical dipole strengths $D^{cr}_{\boldsymbol{\kappa}}$, see fig. 3.4.

Next we will check for bound states. First we note that $K_{\mathrm{i}|\nu|}(z)$ accumulates an infinite number of zeroes as $z \to 0$ [42] and we may conclude, using (3.22), that

once $D > D^{cr}_{\boldsymbol{\kappa}}$ a new infinite set of bound states appears. We will refer to such a set as a *tower* corresponding to $\boldsymbol{\kappa}$. Using (3.22) we may write

$$\eta_{\boldsymbol{\kappa},n} = \frac{z^2_{\boldsymbol{\kappa},n}}{2Mr_0^2},$$

where $z_{\boldsymbol{\kappa},n}$ is the nth largest zero of $K_{\sqrt{A_{\boldsymbol{\kappa}}(D)}}(z)$, $A_{\pm,j} < 0$.

Using

$$\lim_{z\to 0} K_{\mathrm{i}\nu}(z) \approx -\sqrt{\frac{\pi}{\nu \sinh(\pi\nu)}}\left[\sin(\nu\{\ln(z) - \ln(2)\} - \phi_\nu)\right], \tag{3.23}$$

where $\nu \in \mathbb{R}$, $\phi_\nu = \arg(\Gamma[1 + \mathrm{i}\nu])$, we may estimate the functional behavior of $\eta \to 0$. (3.23) becomes exact in the limit $\nu \to 0$. The condition for a zero z_n of (3.23) then reads

$$0 > \nu(\ln(z_n) - \ln(2)) - \phi_\nu = -n\pi.$$

Comparing with (3.22) we find

$$\eta_{\boldsymbol{\kappa},n} = \frac{2}{r_0^2 M}\exp\left(-2\frac{n\pi - \phi_{\nu_{\boldsymbol{\kappa}}}}{\nu_{\boldsymbol{\kappa}}}\right), \quad \nu_{\boldsymbol{\kappa}} = \sqrt{|A_{\boldsymbol{\kappa}}|}. \tag{3.24}$$

We may simplify (3.24) further by expanding $A_{\boldsymbol{\kappa}}$ around $D^{cr}_{\boldsymbol{\kappa}}$. We note, expanding the Mathieu characteristics around their zeroes,

$$A_{+,0} \approx -2(MD)^2$$

for $D \to 0$ and

$$A_{\pm,j} \approx -\frac{\alpha_{\pm,j}}{4}M(D - D^{cr}_{\pm,j})$$

for $D \to D^{cr}_{\pm,j}$ and $j \in \mathbb{N}$. Further [33]

$$\lim_{\nu\to 0}\phi_\nu = -\gamma\nu$$

with the Euler-Mascheroni constant $\gamma \approx 0.5772$. Substituting all of this into (3.24) we arrive at

$$\eta_{+,0,n} = \frac{2\mathrm{e}^{-2\gamma}}{r_0^2 M}\exp\left(-\sqrt{2}\tfrac{n\pi}{MD}\right), \quad \eta_{\pm,j,n} = \frac{2\mathrm{e}^{-2\gamma}}{r_0^2 M}\exp\left(-4\tfrac{n\pi}{\sqrt{\alpha_{\pm,j}M(D-D^{cr}_{\pm,j})}}\right), \quad j \in \mathbb{N},$$

$\boldsymbol{\kappa}$	$\alpha_{\boldsymbol{\kappa}}$	$MD^{cr}_{\boldsymbol{\kappa}}$
$(-,1)$	3.651	1.894
$(+,1)$	3.627	5.324
$(-,2)$	3.643	10.482
$(+,2)$	3.648	17.357

Table 3.1.: The first four numerical values for $\alpha_{\boldsymbol{\kappa}}$ and $MD^{cr}_{\boldsymbol{\kappa}}$.

or in a shorter representation

$$\eta_{\boldsymbol{\kappa},n} = C \exp\left(-\frac{n\pi}{s_{\boldsymbol{\kappa}}}\right), \tag{3.25}$$

where

$$C = \frac{2\mathrm{e}^{-2\gamma}}{r_0^2 M}, \quad s_{\boldsymbol{\kappa}} = \begin{cases} \frac{MD}{\sqrt{2}}, & \text{if } \boldsymbol{\kappa} = (+,0) \\ \frac{\sqrt{\alpha_{\boldsymbol{\kappa}} M(D - D^{cr}_{\boldsymbol{\kappa}})}}{4}, & \text{if } \boldsymbol{\kappa} = (\pm, j), \quad j \in \mathbb{N} \end{cases}. \tag{3.26}$$

For a selection of numeric values of $\alpha_{\boldsymbol{\kappa}}$ and $MD^{cr}_{\boldsymbol{\kappa}}$ please consult table 3.1. We note in passing that if we rescale $r_0 \to r_0\mu$, $\mu \in \mathbb{R}$, we get the same physics by

$$M \to \frac{M}{\mu}, \eta \to \frac{\eta}{\mu} \text{ and } D \to D\mu. \tag{3.27}$$

Note that

$$\lim_{\nu_{\pm,j} \to 0} \eta_{\boldsymbol{\kappa},n} = 0.$$

Also, for $\eta_{\boldsymbol{\kappa},n} \ll M$, $\eta_{\boldsymbol{\kappa},n}$ is a monotonically growing function of $|A_{\boldsymbol{\kappa}}|$ and thus also is a monotonically growing function of $D - D^{cr}_{\boldsymbol{\kappa}}$. From this we conclude that no bound states may return to the continuum, neither by crossing the gap nor by returning to the band they started in, no matter how large the dipole moment may become; at least as long the regularized point-like dipole is a good approximation. We note, however, that other approaches give similar qualitative results, see sec. 3.2.3 below. Once a state become bound by the dipole, it is "trapped" within the for increasing dipole moments.

The energy spectrum near the valence band edge one gets by

$$\epsilon_{\boldsymbol{\kappa},n} = \eta_{\boldsymbol{\kappa},n} - M.$$

Note that due to antisymmetry (3.17) additional bound levels must appear at $-\epsilon_{\boldsymbol{\kappa},n}$, see fig. 3.5 for a qualitative bound level schematics.

We may also now plot corresponding orbitals of our point-like dipole potential solutions, see fig. 3.6. We note that the states look similar to atomic orbitals distorted away from the repulsing center, $\mathbf{c}_+$ for holes, $\mathbf{c}_-$ for electrons. The density function for electrons and holes with the same quantum numbers $(\boldsymbol{\kappa}, n)$ are related to each other by $x \to -x$. For a state with the quantum numbers $(\boldsymbol{\kappa}, n)$ one observes $n-1$ radial and $j + \frac{1}{2} \pm \frac{1}{2}$ angular nodes. Also we may observe from (C.10) that the states are confined on a scale $\sqrt{M\eta}^{-1}$. From this follows: the deeper a state is bound within the gap the stronger it is confined. This resembles the physics of atomic orbitals.

Since no level that gets bound by the dipole can return to the continuum, the gap will become very densely populated. We will estimate the density of bound states, which is defined as

$$\nu(\eta) = \sum_{\boldsymbol{\kappa}} \nu_{\boldsymbol{\kappa}} = \sum_{\boldsymbol{\kappa}} \sum_{n} \delta(\eta - \eta_{n,\boldsymbol{\kappa}}),$$

Focusing on one tower $\boldsymbol{\kappa}$ we may introduce a physical level broadening

$$\delta(\eta - \tilde{\eta}) \to \frac{1}{2\pi} \frac{\Gamma}{\Gamma^2 + (\eta - \tilde{\eta})^2}.$$

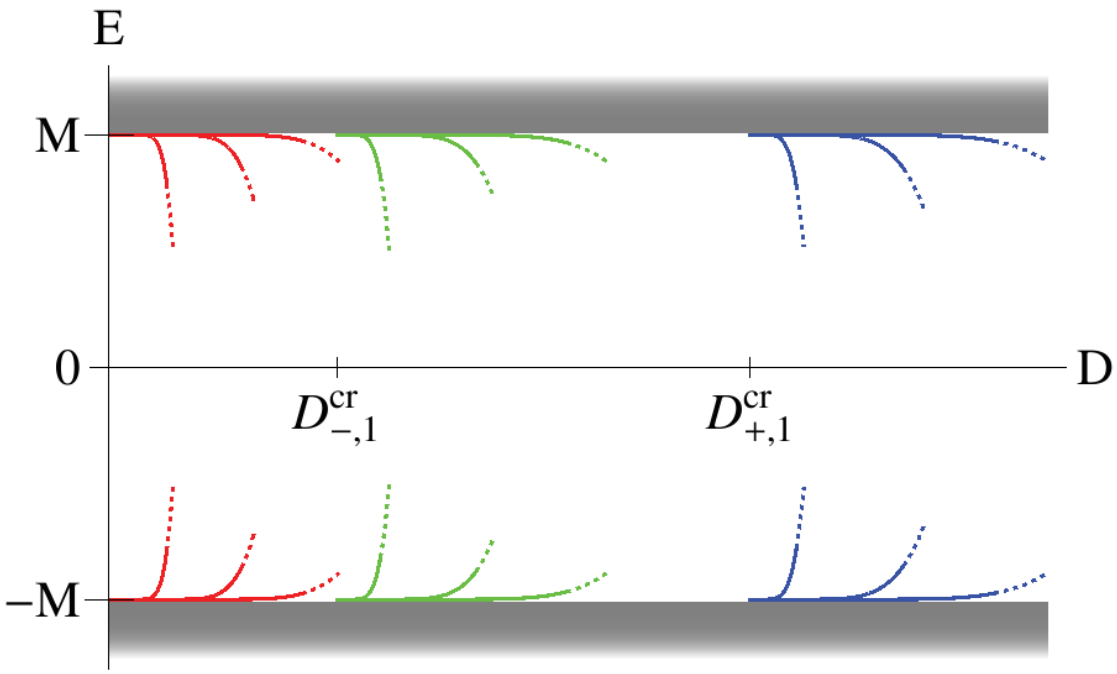

Figure 3.5.: The qualitative level spectrum of the dipole problem near the band edges.

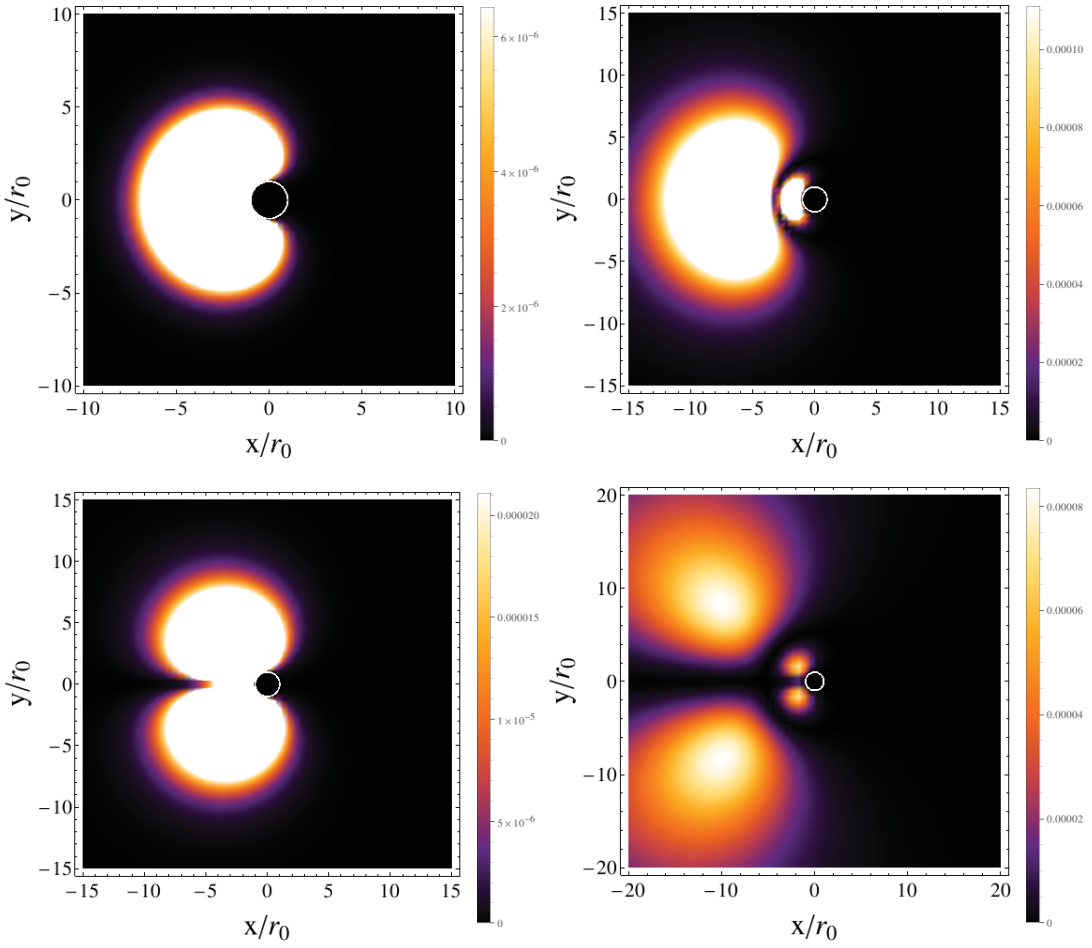

Figure 3.6.: Weakly bound hole states-density (3.22) on the scale $\frac{\mathbf{r}}{r_0}$. Top left: $(+,0,1)$. Top right: $(+,0,2)$. Bottom left: $(-,1,1)$. Bottom right: $(-,1,2)$.

Making the assumption

$$\sum_{n=1}^{\infty} \approx \int_{1}^{\infty} dn = \int_{0}^{\eta_{\boldsymbol{\kappa},1}} \frac{d\eta_{\boldsymbol{\kappa},n}}{|d\eta_{\boldsymbol{\kappa},n}/dn|}$$

justified by the fact that the energies vary slowly on the scale of M as a function of n and regularizing the density at $\eta \to 0$ by a cutoff μ to avoid divergences

inside the integral, one finds

$$\nu_\kappa(\eta) = \lim_{\mu\to 0} \frac{s_\kappa \Gamma}{4\pi^2} \int_\mu^{\eta_{\kappa,1}} \frac{dy}{y(\Gamma^2 + (\eta - y)^2)} =$$
$$- \frac{s_{j,\kappa}\Gamma}{4\pi^2} \lim_{\mu\to 0} \left[\frac{2\eta(\arctan\left(\frac{(\eta-y)}{\Gamma}\right) + \Gamma(\ln(\Gamma^2 + (\eta - y)^2) - 2\ln(y))}{2\Gamma(\Gamma^2 + \eta^2)} \right]_{y=\mu}^{y=\eta_{\kappa,1}}.$$

Now one may perform the limits $\Gamma \to 0$ (zero temperature) and $\mu \to 0$ thereafter. It turns out the only part of the above equations, which survives the first limit, is the arctan. This results in

$$\nu_\kappa(\eta) = \frac{s_\kappa}{4\pi} \frac{1 - \text{sign}(\eta - \eta_{\kappa,1})}{\eta} = \frac{s_\kappa}{2\pi\eta} \theta(\eta_{\kappa,1} - \eta),$$

where we used $\lim_{x\to\infty} \arctan(\pm x) = \pm\pi$ and $\eta > \mu$.

We encounter a divergence at $\eta \to 0$, which is not surprising, since the bound states accumulate near the band edges. Note that the prefactor of this divergences has a noncontinuous derivative w.r.t D at D_κ^{cr}, since new towers appear at these critical dipole moments.

We also note an interesting feature for two successive levels from the same tower:

$$\frac{\eta_{\kappa,n}}{\eta_{\kappa,n+1}} = \exp\left(\frac{\pi}{s_\kappa}\right).$$

This is the so-called Efimov scaling, which was initially discovered in context the of the 3-body boson problem with short range interactions [44] . This characteristic was also predicted for supercritical impurities in graphene, [45] and [46], as well as for Schrödinger fermions in three dimensions [47]. In the dipole case it has its source in the long distance characteristics of the potential at hand. We thus expect it to be independent of the regularization procedure.

3.2.3 Non Relativistic Limit - Abramov-Komarov Solution

One may argue that the qualitative behavior found in the last section will strongly depend on the choice of the boundary-conditions used. To prove the opposite we will use a model that differs strongly from the one we used in the last section.

In 1972 Abramov and Komarov [47] were investigating the bound states spectrum of a non relativistic electron in the field of a dipole in three dimensions

using prolate spheroidal coordinates. It turns out that (3.18) in elliptic coordinates (app. A) with the full two center potential,

$$V^{tc} = -\alpha(\frac{1}{r_+} - \frac{1}{r_-}) = -\frac{4D\nu}{R^2(\mu^2 - \nu^2)},$$

where $D = \alpha R$, coincides with the equation treated in [47]. We will show that although the models only agree in the $r \to \infty$ asymptotics, the results are qualitatively equal.

In elliptic coordinates (3.18) reads

$$\begin{aligned} 0 =& \left(\Delta + 2M(-\eta^{AK} + V^{tc})\right) g \\ =& \frac{4}{R^2(\mu^2 - \nu^2)} \left((\mu^2 - 1)\partial_\mu^2 + \mu\partial\mu - (\nu^2 - 1)\partial_\nu^2 - \nu\partial\nu - \tfrac{1}{2}\eta^{AK}R^2(\mu^2 - \nu^2) - MD\nu)\right), \end{aligned}$$

or equivalently

$$\left((\mu^2 - 1)\partial_\mu^2 + \mu\partial\mu - \tfrac{1}{2}\eta^{AK}R^2\mu^2\right) g = \left((\nu^2 - 1)\partial_\nu^2 + \nu\partial\nu - \tfrac{1}{2}\eta^{AK}R^2\nu^2 + MD\nu\right) g.$$

Using the ansatz

$$g = \frac{U(\mu)}{\sqrt[4]{\mu^2 - 1}} \frac{V(\nu)}{\sqrt[4]{1 - \nu^2}}$$

and introducing the separation constant A, the final separated equations are

$$\begin{aligned} 0 &= \left(\partial_\mu^2 - \frac{R^2M\eta^{AK}}{2} + \frac{A}{\mu^2 - 1} + \frac{3}{4}\frac{1}{(\mu^2 - 1)^2}\right) U(\mu), \\ 0 &= \left(\partial_\nu^2 - \frac{R^2M\eta^{AK}}{2} + \frac{2DM\nu + A}{1 - \nu^2} + \frac{3}{4}\frac{1}{(1 - \nu^2)^2}\right) V(\nu). \end{aligned}$$

Comparing with the starting point of [47],

$$\begin{aligned} 0 &= \left(\partial_\mu^2 + \frac{R^2M\eta^{AK}}{2} + \frac{A}{\mu^2 - 1} + \frac{1 - m^2}{(\mu^2 - 1)^2}\right) U(\mu), \\ 0 &= \left(\partial_\nu^2 + \frac{R^2M\eta^{AK}}{2} + \frac{2DM\nu + A}{1 - \nu^2} + \frac{1 - m^2}{(1 - \nu^2)^2}\right) V(\nu), \end{aligned}$$

where the notation is identical up to m, which in their case is the rotational quantum number along the dipole axis, one finds that both equations are equal if one sets $m^2 = \frac{1}{4}$ and changes the sign of η. This allows us simply to read off the solutions to our equations from the results in [47]. Note, however, that their

solution is approximate in the sense of an expansion in $1/\sqrt{D}$ and thus should fail at $D \to 0$.

They find

$$-\frac{R^2 M \eta^{AK}}{2} \approx \exp\left(-\frac{\Gamma\left(\frac{1}{4}\right)^2 (n+1)}{2\sqrt{M(D-D^{cr,AK})}} + 2\tau(0,m)\right)$$

where

$$\tau(x,m) = 2\ln(2) + \frac{2\arg\left(\Gamma(1+\mathrm{i}x)\right) - \arg\left(\Gamma(1+\mathrm{i}x-m)\right)}{x}.$$

Substituting the variables of our problem we find

$$\begin{aligned} \eta^{AK}_{\boldsymbol{\kappa},n} &\approx \frac{2^5 \mathrm{e}^{-2\gamma}}{RM^2} \exp\left(-\Gamma\left(\tfrac{1}{4}\right)^2 \frac{n+\frac{1}{2}}{2\sqrt{M(D-D^{cr,AK}_{\boldsymbol{\kappa}})}}\right), \\ MD^{cr,AK}_{\boldsymbol{\kappa}} &\approx \frac{\Gamma\left(\frac{1}{4}\right)^4}{64\pi}\left(\left(2m \pm \frac{1}{2}\right)^2 - \frac{1}{6\pi}\right). \end{aligned} \tag{3.28}$$

We note that the functional shape of energies in (3.28) qualitatively agree well with the previous results, (3.25), up to some prefactors. Also we may observe the Efimov scaling again. Thus we may conclude that it is indeed an universal feature of bound states of a potential $\propto \frac{\cos(\phi)}{r^2}$ for $r \to \infty$.

We note that also the critical dipole strengths for formation of bound levels are in good agreement with above results, see tab. 3.2. The only strong deviation occurs at $\boldsymbol{\kappa} = (+,0)$, for which [47] predict a finite dipole strength necessary to allow bound states. However, since their results rely on an expansion in $1/\sqrt{D}$ we may expect that their method fails at $D \to 0$. We also would like to turn the readers attention to a more recent publication, in which it was shown that for the full, relativistic, two center problem, always infinitely many bound states exist [48].

Note that (3.28) allows estimates of zeroes of Mathieu characteristic values a_{2j}, b_{2j}.

3.2.4 Numerical Results on a Finite Disc

So far we could only find the qualitative shape of the spectrum in the vicinity of band edges analytically. Unfortunately there seems to be no way to get the analytic solution for the full Dirac problem, i.e. also to make statements about

$\boldsymbol{\kappa}$	$MD^{cr}_{\boldsymbol{\kappa}}$	$MD^{cr,AK}_{\boldsymbol{\kappa}}$
$(+,0)$	0	0.169
$(-,1)$	1.894	1.888
$(+,1)$	5.324	5.326
$(-,2)$	10.482	10.482
$(+,2)$	17.357	17.357
$(-,3)$	25.951	25.951

Table 3.2.: Comparison of critical dipole strength obtained using the regularized point-like dipole solution, $MD^{cr}_{\boldsymbol{\kappa}}$, and using the results of [47], $MD^{cr,AK}_{\boldsymbol{\kappa}}$.

solutions deep within the gap. Therefore, we will resort to a numerical analysis of the problem to gain an intuition for the behavior of deeply bound states by means of exact diagonalization, [49], [50], on a finite disc.

Our further procedure will be the expansion of the regularized point-like dipole Hamiltonian in free ($V \equiv 0$) solutions on a disc with radius R_c, $\boldsymbol{\psi}_{\boldsymbol{\lambda}}(\mathbf{x}) = \langle \mathbf{x}|\boldsymbol{\lambda}\rangle$, where $\boldsymbol{\lambda}$ may be some multiindex, with appropriate boundary conditions at $r = R_c$. This model serves well to describe a graphene flake with a dipole impurity somewhere on top of it. Note, however, that we may also achieve the quasicontinuous case $R_c \to \infty$ to make the numerical results comparable with bulk graphene. Especially in the dipole case, where the potential is quickly decaying away from the center, one may argue that finite size effects are of small importance.

The energy solutions are then found as the eigenvalues of the matrix

$$H_{\boldsymbol{\lambda},\boldsymbol{\lambda}'} = \langle \boldsymbol{\lambda}|H_T + V^{pd}|\boldsymbol{\lambda}'\rangle, \tag{3.29}$$

where V^{pd} is the regularized point-like dipole potential. Since H_T is already diagonal in $\boldsymbol{\psi}_{\boldsymbol{\lambda}}(\mathbf{x})$ one only needs to calculate the overlaps

$$V_{\boldsymbol{\lambda},\boldsymbol{\lambda}'} = \langle \boldsymbol{\lambda}|V^{pd}|\boldsymbol{\lambda}'\rangle,$$

which we do numerically by the built-in global adaptive *Mathematica* algorithm.

To be more precise, focusing on the K-point $\mathbf{K}$, we expand in free, spherical solutions of (2.8) [31]

$$\boldsymbol{\psi}_{\epsilon,m}(r,\phi) = \mathcal{N}\mathrm{e}^{\mathrm{i}\nu}\begin{bmatrix} a_\epsilon J_{|m|}(u_\epsilon r)\mathrm{e}^{\mathrm{i}m\phi} \\ \mathrm{i}\ \mathrm{sign}(m+\frac{1}{2})\mathrm{sign}(\epsilon) b_\epsilon J_{|m+1|}(u_\epsilon r) e^{\mathrm{i}(m+1)\phi} \end{bmatrix} = \begin{bmatrix} f_{\epsilon,m}(r,\phi) \\ g_{\epsilon,m}(r,\phi) \end{bmatrix} = \langle \mathbf{x}|\epsilon, m\rangle,$$

where $a_\epsilon = \sqrt{|\epsilon + M|}$, $b_\epsilon = \sqrt{|\epsilon - M|}$, $u_\epsilon = a_\epsilon b_\epsilon$ and $\nu \in \mathbb{R}$ is some fixed phase. These solutions fulfill

$$H_T \boldsymbol{\psi}_{\epsilon,m}(r,\phi) = \epsilon \boldsymbol{\psi}_{\epsilon,m}(r,\phi).$$

The boundary conditions we assume to be of minor importance, since for not to small R_c $V^{pd}(R_c)$ goes quickly to 0 and thus it should make not much difference how the states look like close to the boundary. We also note in passing that $V^{pd} \propto (e^{i\phi} + e^{-i\phi})/r^2$ may only couple m and $m \pm 1$.

As we will see below, a convenient choice turns out to be the so-called infinite mass boundary condition [51]:

$$\frac{g_{\epsilon,m}(R_c,\phi)}{f_{\epsilon,m}(R_c,\phi)} = i\exp(i\phi),$$

or, by substituting f and g with their definitions,

$$a_\epsilon J_{|m|}(u_\epsilon R_c) = \mathrm{sign}(m+\tfrac{1}{2})\mathrm{sign}(\epsilon) b_\epsilon J_{|m+1|}(u_\epsilon R_c). \tag{3.30}$$

Solving this for ϵ will give us the discrete spectrum of the disc without any external potential.

We observe the identity $a_{-\epsilon} = b_\epsilon$, from which quickly follows: if ϵ solves the boundary condition (3.30) for $\boldsymbol{\psi}_{\epsilon,m}$, then $-\epsilon$ solves (3.30) $\boldsymbol{\psi}_{\epsilon,-m-1}$. Note that this corresponds to the antisymmetry of the Hamiltonian (3.17). We choose $\nu = 0$ for the positive part of the spectrum and derive the states with negative energies from positive energy states by the symmetry transformation (3.17),

$$\boldsymbol{\psi}_{-\epsilon,-m-1} = \sigma_x \mathcal{R}_x \boldsymbol{\psi}_{\epsilon,m}.$$

From this we may easily derive

$$\begin{aligned}\langle \epsilon, m|V^{pd}|\epsilon', m'\rangle &= \langle -\epsilon, -m-1|\sigma_x\mathcal{R}_x V^{pd}\sigma_x\mathcal{R}_x|-\epsilon', -m'-1\rangle \\ &= -\langle -\epsilon, -m-1|V^{pd}|-\epsilon', -m'-1\rangle.\end{aligned}$$

Including the hermiticity, this reduces the number of matrix elements we need to calculate by a factor of 4. The eigenvalues of the matrices $H_{i,j}$ may then be calculated numerically. Besides R one has to introduce cutoffs of the energy, ϵ_{co}, and of angular momentum, m_{co}. One expects convergence for $R_c \gg r_0$, which is desired anyway, since we are interested in the quasicontinuous case, and $V^{pd}(r_0) \ll E_{co}$. Also one may easily show that our results will obey (3.27). First observe that by scaling $R_c \to R_c/\mu$, $\mu \in \mathbb{R}$, the solutions to the boundary condition (3.30) scale like $\epsilon \to \mu\epsilon$, since we can rewrite the condition (3.30) as

$$0 = f\left(\sqrt{(\epsilon - M)(\epsilon + M)}R_c, \frac{\epsilon - M}{\epsilon + M}\right) = f\left(\sqrt{(\mu\epsilon - \mu M)(\mu\epsilon + \mu M)}\frac{R_c}{\mu}, \frac{\mu\epsilon - \mu M}{\mu\epsilon + \mu M}\right)$$

with some appropriate function f. Next we are calculating how the normalizations scale. Given the parameters M, R_c and $\boldsymbol{\epsilon}$, the last of whom is the set of all

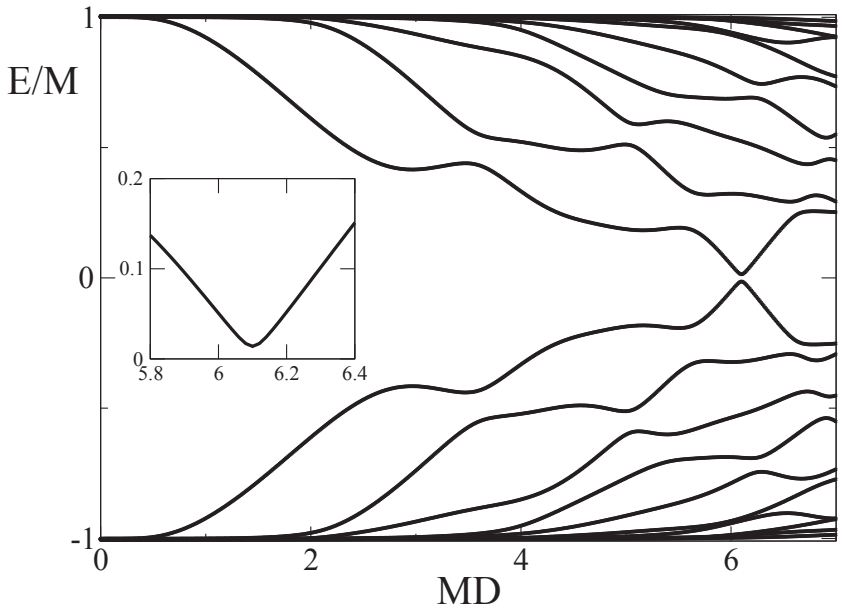

Figure 3.7.: The spectrum of a dipole on a finite disc calculated by the exact diagonalization procedure, $r_0 M = 1$, $RM = 75$, $\epsilon_{co} = 10M$, $m_{co} = 8$. Note the symmetry w.r.t. $E \to -E$. Inset: a zoomed in picture of the lowest level in the vicinity of the zero energy avoided crossing for $DM \approx 6.09$. The minimal energy there is $E_{min} \approx 0.014M$.

energies supported by the free disc,

$$\mathcal{N}_i^{(M,R_c,\boldsymbol{\epsilon})} = \int_0^{R_c} dr\, r|\boldsymbol{\psi}_i(u_i r)|^2 \xrightarrow{r=\mu\tilde{r}} \mu^2 \int_0^{\frac{R_c}{\mu}} d\tilde{r}\, \tilde{r}|\boldsymbol{\psi}_i(\mu u_i \tilde{r})|^2 = \mu^2 \mathcal{N}_i^{(\mu M,R_c/\mu,\mu\boldsymbol{\epsilon})}.$$

To expand H we are evaluating integrals of the form

$$\begin{aligned}\frac{H_{i,j}^{(M,R_c,r_0,\boldsymbol{\epsilon},D)}}{M} &= \frac{\epsilon_i}{M}\delta_{i,j} + \frac{D}{M\sqrt{\mathcal{N}_i^{(M,R_c,\boldsymbol{\epsilon})}\mathcal{N}_i^{(M,R_c,\boldsymbol{\epsilon})}}} \int_0^{R_c} dr\, r \frac{\boldsymbol{\psi}_i^\dagger(u_i r)\boldsymbol{\psi}_j(u_j r)}{\max(r_0,r)^2} \\ &\xrightarrow{r=\mu\tilde{r}} \frac{\mu\epsilon_i}{\mu M}\delta_{i,j} + \frac{(D/\mu)}{\mu M\sqrt{\mathcal{N}_i^{(M\mu,R_c/\mu,\mu\boldsymbol{\epsilon})}\mathcal{N}_j^{(M\mu,R/\mu,\mu\boldsymbol{\epsilon})}}} \int_0^{R_c/\mu} d\tilde{r}\, \tilde{r} \frac{\boldsymbol{\psi}_i^\dagger(\mu u_i \tilde{r})\boldsymbol{\psi}_j(\mu u_j \tilde{r})}{\max(r_0/\mu,\tilde{r})^2} \\ &= \frac{H_{i,j}^{(\mu M,R_c/\mu,r_0/\mu,\mu\boldsymbol{\epsilon},D/\mu)}}{\mu M}.\end{aligned} \tag{3.31}$$

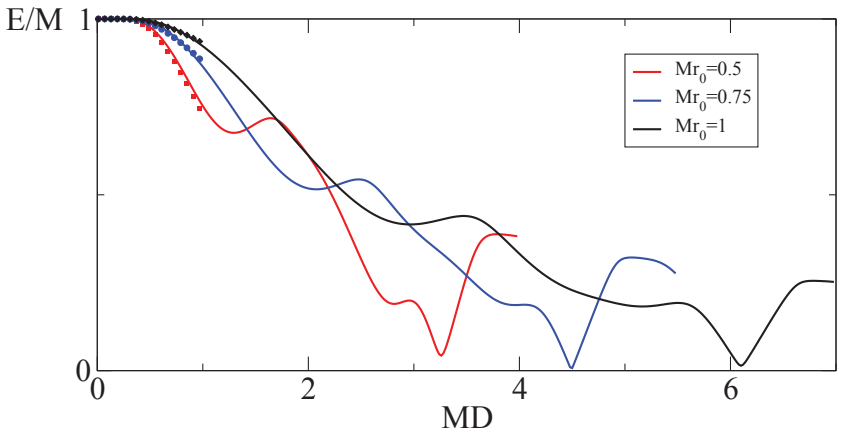

Figure 3.8.: The lowest bound states for $Mr_0 = 0.5$, $Mr_0 = 0.75$ $Mr_0 = 1$, $MR_c = 20$, $\epsilon_{co} = 10M$, $m_{co} = 7$. Dots correspond to respective expressions from (3.32).

Setting $\mu = M^{-1}$ we may eliminate and thus skip M as a parameter, by measuring all other parameters in units of M.

When using $r_0 M = 1$, convergence deep inside the gap, $|\epsilon| < M$, is quickly achieved at $\epsilon_{co} \approx 10M$, $R_c M \approx 20$, $m_{co} = 7$, which forms a space of dimension ≈ 2000. The quasicontinuum, $|\epsilon| > M$, is strongly dependent on R_c, though, thus we expect the results very close to the gap to be a poor approximation.

The results for the lowest (with respect to absolute energy) 20 levels are presented in fig. 3.7. We note many avoided crossings inside the gap. Since the levels are symmetric w.r.t. $\epsilon \to -\epsilon$, they will also avoid crossing $\epsilon = 0$. Because of this reason one expects no criticality. These results are qualitatively equal to other choices of $r_0 M$, see fig. 3.8.

Note that it is difficult to compare the numerical results from the exact diagonalization, which is supposed to give good results deep within the gap, with the weakly bound levels found in previous sections, which are only valid near the edges of the gap. Still, we empirically managed to find a fit, see fig. 3.8, of the type

$$\epsilon(D) = M - \frac{2e^{-2\gamma}}{r_0^2 M} \exp\left(-\frac{\pi\sqrt{2}\nu}{MD}\right), \tag{3.32}$$

which highly resembles (3.25), up to a prefactor $\nu \approx 2^{-1}$ in the D-dependent exponent, and is valid for all choices of Mr_0, even well within the gap. This change of the prefactor s_κ is not surprising, since it depends on boundary conditions at r_0, as may be see by comparing the Abramov-Komarov solutions, (3.28), and the point-like dipole solutions, (3.25). Unfortunately we could not find appropriate

fits for other levels. This we refer to the fact that the other levels are quite shallow and the convergence near the edge of the gap is slow, since the continuum reacts strongly on the change of the boundary condition.

3.2.5 Scattering

A very important observable of a solid state system is its resistivity. Obviously this is dependent on the scattering within the sample, i.e. the inability of a plane wave to propagate, without being scattered by impurities.

We would like to investigate the dependency of scattering on the presence of a dipole type impurity by means of exact analysis near the gap boundary, where we have exact analytical solutions, and deep within the bands, where we may rely on perturbative analysis by means of the Born approximation, see [31].

Regularized Point-like Dipole

We will now focus on a situation, where an electron, characterized by the wave vector

$$\mathbf{k} = \sqrt{(\epsilon - M)(\epsilon + M)}[\cos(\phi_{\mathbf{k}}), \sin(\phi_{\mathbf{k}})]^T,$$

is scattered by the regularized, point-like dipole [38]. Since we would like to use our analytical solutions above, we focus on energies near the conduction band edge, $\eta = \epsilon - M \ll M$.

Asymptotically our solution at some energy should have the form of a freely propagating wave and a circular, scattered part,

$$\lim_{r\to\infty} \psi(\mathbf{r}) = \mathrm{e}^{\mathrm{i}\mathbf{k}\cdot\mathbf{r}} + f_{\phi_{\mathbf{k}}}(\phi)\frac{\mathrm{e}^{\mathrm{i}kr}}{\sqrt{r}},$$

where

$$k = \sqrt{(\epsilon - M)(\epsilon + M)} \approx \sqrt{2M\eta}.$$

We now need to construct this type of asymptotic out of solutions of the radial wave equation, (3.20), inside the conduction band. The results for the valence band follow by the antisymmetry (3.17). We find using the same notation for A_κ as before (3.21):

$$R(r) = \beta_\kappa H^{(1)}_{\sqrt{A_\kappa}}(kr) + H^{(2)}_{\sqrt{A_\kappa}}(kr),$$

where $H^{(1,2)}$ are the corresponding Hankel functions (C.3), $\boldsymbol{\kappa} = (\pm, j)$ and

$$\beta_{\boldsymbol{\kappa}} = -\frac{H^{(2)}_{\sqrt{A_{\boldsymbol{\kappa}}}}(kr_0)}{H^{(1)}_{\sqrt{A_{\boldsymbol{\kappa}}}}(kr_0)}$$

is chosen in a way to fulfill the boundary conditions $R(r_0) = 0$. Any general solution with energy η we may write as a superposition of these solutions

$$\psi_\eta(r) = \sum_{\boldsymbol{\kappa}} c_{\boldsymbol{\kappa}} \left(\beta_{\boldsymbol{\kappa}} H^{(1)}_{\sqrt{A_{\boldsymbol{\kappa}}}}(kr) + H^{(2)}_{\sqrt{A_{\boldsymbol{\kappa}}}}(kr) \right) \Phi_{\boldsymbol{\kappa}}(\phi), \tag{3.33}$$

where we used the definition (3.21) for Φ and $c_{\boldsymbol{\kappa}} \in \mathbb{C}$. Asymptotically this behaves like

$$\psi_\eta(r \to \infty) = \sqrt{\frac{2}{\pi \mathrm{i} kr}} \sum_{\boldsymbol{\kappa}} c_{\boldsymbol{\kappa}} \left(\beta_{\boldsymbol{\kappa}} e^{\mathrm{i}kr} e^{-\mathrm{i}\frac{\pi\sqrt{A_{\boldsymbol{\kappa}}}}{2}} + \mathrm{i} e^{-\mathrm{i}kr} e^{\mathrm{i}\frac{\pi\sqrt{A_{\boldsymbol{\kappa}}}}{2}} \right) \Phi_{\boldsymbol{\kappa}}(\phi). \tag{3.34}$$

We would like to compare this with the incoming part of the wave function, where we suppress the second argument of the Mathieu functions, *ce* and *se*, for convenience:

$$\begin{aligned}
\mathrm{e}^{\mathrm{i}kr\cos(\phi-\phi_{\mathbf{k}})} &= \sum_{m=-\infty}^{\infty} \mathrm{i}^m J_m(kr) \cos(m(\phi - \phi_{\mathbf{k}})) \\
&= \sum_{m=-\infty}^{\infty} \mathrm{i}^m J_m(kr) \left[\cos(m\phi)\cos(m\phi_{\mathbf{k}}) + \sin(m\phi)\sin(m\phi_{\mathbf{k}}) \right] \\
&= \sqrt{\frac{1}{2\pi \mathrm{i} kr}} \sum_{m=-\infty}^{\infty} \left(\mathrm{e}^{\mathrm{i}kr} + \mathrm{i}(-1)^m \mathrm{e}^{-\mathrm{i}kr} \right) \left[\cos(m\phi)\cos(m\phi_{\mathbf{k}}) + \sin(m\phi)\sin(m\phi_{\mathbf{k}}) \right] \\
&= \sqrt{\frac{2}{\pi \mathrm{i} kr}} \left\{ \mathrm{e}^{\mathrm{i}kr} \sum_{j=0}^{\infty} \left(ce_{2j}\left(\frac{\phi_{\mathbf{k}}}{2}\right) ce_{2j}\left(\frac{\phi}{2}\right) + se_{2(j+1)}\left(\frac{\phi_{\mathbf{k}}}{2}\right) se_{2(j+1)}\left(\frac{\phi}{2}\right) \right) \right. \\
&\left. + \mathrm{i}\mathrm{e}^{-\mathrm{i}kr} \sum_{j=0}^{\infty} \left(ce_{2j}\left(\frac{\pi+\phi_{\mathbf{k}}}{2}\right) ce_{2j}\left(\frac{\phi}{2}\right) + se_{2(j+1)}\left(\frac{\pi+\phi_{\mathbf{k}}}{2}\right) se_{2(j+1)}\left(\frac{\phi}{2}\right) \right) \right\}.
\end{aligned} \tag{3.35}$$

Here we expanded sin and cos in terms of the Mathieu functions, see (B.3) for details, and used

$$(-1)^m \cos(\phi) = \cos(m\pi + \phi), \quad (-1)^m \sin(\phi) = \sin(m\pi + \phi).$$

Now we require that all contributions $\propto \exp(-ikr)$ in (3.34), which correspond to incoming circular waves, stem from the incoming part of the wave function (3.35). This may be achieved by setting

$$c_{+,j} = \mathrm{e}^{-\mathrm{i}\frac{\pi\sqrt{A_{+,j}}}{2}} ce_{2j}\left(\frac{\pi+\phi_{\mathbf{k}}}{2}\right),$$
$$c_{-,j} = \mathrm{e}^{-\mathrm{i}\frac{\pi\sqrt{A_{-,j}}}{2}} se_{2j}\left(\frac{\pi+\phi_{\mathbf{k}}}{2}\right).$$

Substituting everything into (3.33) and subtracting the incoming part $\propto \mathrm{e}^{\mathbf{ik}\cdot\mathbf{r}}$ we get

$$f_{\phi_{\mathbf{k}}}(\phi) = \sum_{\boldsymbol{\kappa}} f_{\boldsymbol{\kappa},\phi_{\mathbf{k}}}(\phi),$$

where

$$\begin{aligned} f_{+,j,\phi_{\mathbf{k}}}(\phi) &= \sqrt{\frac{2}{\pi \mathrm{i}k}}\left[\beta_{+,j} ce_{2j}\left(\frac{\pi+\phi_{\mathbf{k}}}{2}\right) e^{-\mathrm{i}\pi\sqrt{A_{+,j}}} - ce_{2j}\left(\frac{\phi_{\mathbf{k}}}{2}\right)\right] ce_{2j}\left(\frac{\phi}{2}\right), \\ f_{-,j,\phi_{\mathbf{k}}}(\phi) &= \sqrt{\frac{2}{\pi \mathrm{i}k}}\left[\beta_{-,j} se_{2j}\left(\frac{\pi+\phi_{\mathbf{k}}}{2}\right) e^{-\mathrm{i}\pi\sqrt{A_{-,j}}} - se_{2j}\left(\frac{\phi_{\mathbf{k}}}{2}\right)\right] se_{2j}\left(\frac{\phi}{2}\right). \end{aligned} \tag{3.36}$$

By defining the scattering cross section as the ratio of total outgoing current divided by the incoming current density, we get

$$\Lambda = \int_0^{2\pi} |f_{\phi_{\mathbf{k}}}(\phi)|^2 d\phi.$$

Also we may calculate the transport cross section, which describes the backscattered contribution by adding a weight function $\propto (kr - \mathbf{k}\cdot\mathbf{r})$:

$$\Lambda_{tr} = \int_0^{2\pi} (1 - \cos(\phi - \phi_{\mathbf{k}}))|f_{\phi_{\mathbf{k}}}(\phi)|^2 d\phi.$$

We may now plot Λ and Λ_{tr} resolved in $\phi_{\mathbf{k}}$, see fig 3.9. Note a suppressed backscattering at $\phi_{\mathbf{k}} = \pi$, which corresponds to incidence normal to the dipole axis. One may argue that the reason for that is the equal contribution to the scattering from both, oppositely charged centers, which destructively interfere with each other.

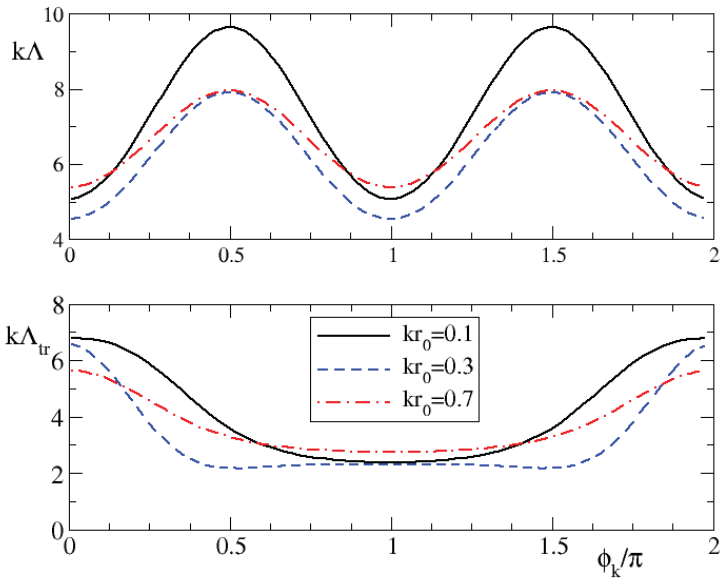

Figure 3.9.: Scattering (top) and transport (bottom) cross section angular dependency w.r.t. the angle of incidence for the incoming electron as contributed to by the five lowest channels from (3.36). $MD = 1.05$.

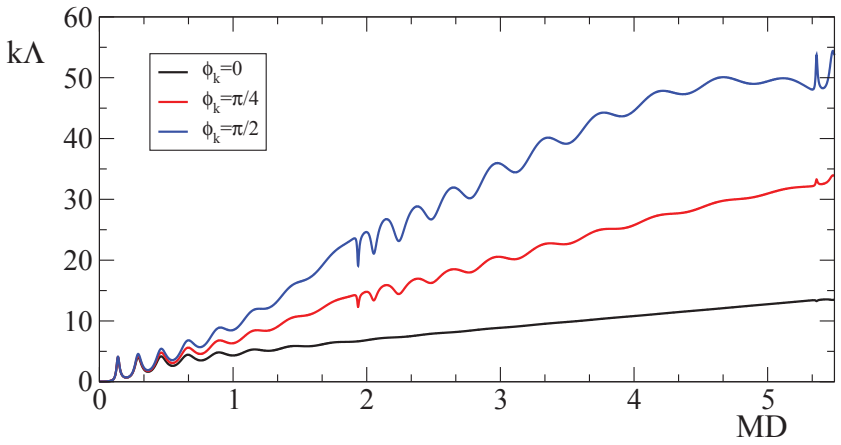

Figure 3.10.: Scattering cross section for a point dipole impurity at $k = 10^{-9}M$, $r_0M = 100$ in the non relativistic limit. Note the resonances at threshold values $MD^{cr}_{-,1} \approx 1.894$ and $MD^{cr}_{+,1} \approx 5.325$ from (3.36).

Also we may see the resonances attributed to appearance of new towers,

which become more pronounced for $|\phi_{\mathbf{k}}| = \pi$, fig. 3.10.

Note that there is a net scattering even for $MD \to 0$, which is the effect of the residual regularization procedure of an infinitely repulsive core, that still may scatter, but it is negligible against the dipole contribution. In the presence of the dipole the scattering amplitude has a separate dependency in ϕ and $\phi_{\mathbf{k}}$, in contrast to the case of a rotatonally invariant scatterer such as the infinitely repulsive core.

Born Approximation

In this section we apply the Born approximation procedure [40], as introduced in [31], to the full dipole problem. The Born approximation usually works well for high energies $|\epsilon/M| \gg 1$, and thus seems appropriate to gain an intuition for the scattering far inside one of the bands. It may not capture any resonances, though, since there is no implicit dependency on the coupling parameter.

We again would like to construct a solution of the Dirac equation with a dipole potential, which asymptotically behaves like

$$\boldsymbol{\psi} = \boldsymbol{\psi}_{in} + \boldsymbol{\psi}_{out},$$

where we assume the incident wave function to be a solution freely propagating along $\mathbf{k}$ [31]

$$\boldsymbol{\psi}_{in,\mathbf{k}}(\mathbf{r}) = \frac{1}{\sqrt{2|\epsilon|}} \begin{bmatrix} \sqrt{|\epsilon + M|} e^{-i\frac{\phi_{\mathbf{k}}}{2}} \\ \text{sign}(\epsilon) \sqrt{|\epsilon - M|} e^{i\frac{\phi_{\mathbf{k}}}{2}} \end{bmatrix} e^{i\mathbf{k}\cdot\mathbf{r}} = \mathbf{u}_{\epsilon,\phi_{\mathbf{k}}} e^{i\mathbf{k}\cdot\mathbf{r}},$$

where $\mathbf{k} = \sqrt{(\epsilon - M)(\epsilon + M)}[\cos(\phi_{\mathbf{k}}), \sin(\phi_{\mathbf{k}})]^T$, $\phi_{\mathbf{k}}$ is the incidence angle w.r.t. the x-axis.

In the Born approximation, which corresponds to first-order perturbation theory, one may express the outgoing scattered wave as

$$(H_T - \epsilon)\boldsymbol{\psi}_{out} = -V\boldsymbol{\psi}_{in}.$$

From this it follows [31]

$$\boldsymbol{\psi}_{out}(\mathbf{r}) = -\int d\mathbf{r}' G_\epsilon(\mathbf{r} - \mathbf{r}')(H_T + \epsilon)V(\mathbf{r}')\boldsymbol{\psi}_{in}(\mathbf{r}'),$$

where

$$\begin{aligned} G_\epsilon(\mathbf{r}') &= \int \frac{d\mathbf{k}}{4\pi^2} \frac{e^{i\mathbf{k}\cdot\mathbf{r}}}{(k^2 + M^2 - (\epsilon + i\,\text{sign}(\epsilon)0))} \\ &= \frac{i\,\text{sign}(\epsilon)}{4} H_0^{(1)}(pr) \xrightarrow{r\to\infty} \frac{i\,\text{sign}(\epsilon)}{4} \sqrt{\frac{2}{\pi pr}} e^{i\left(pr - \frac{\pi}{4}\right)} \end{aligned}$$

is the free Greens-function and $p = \sqrt{\epsilon^2 - M^2}$ and $H_0^{(1)}$ again the corresponding Hankel function of the first kind (C.3). After some straightforward calculations in the large-distance limit, $r \gg r'$, one gets

$$\psi_{out}(\mathbf{r}) \approx \frac{f^{Born}(\phi - \phi_{\mathbf{k}})}{\sqrt{\mathrm{i}r}} \mathbf{u}_{\epsilon,\phi-\phi_{\mathbf{k}}} e^{\mathrm{i}kr},$$

where

$$\begin{aligned} f^{Born}(\phi, \phi_{\mathbf{k}}) &= -\sqrt{\frac{k}{8\pi}} \tilde{V}(\mathbf{k}' - \mathbf{k}) b(\phi - \phi_{\mathbf{k}}), \\ \tilde{V}(\mathbf{k}) &= \int d\mathbf{r} \mathrm{e}^{-\mathrm{i}\mathbf{k}\cdot\mathbf{r}} V(\mathbf{r}), \\ b(\phi) &= \mathrm{e}^{\mathrm{i}\frac{\phi}{2}} \sqrt{\frac{|\epsilon + M|}{|\epsilon - M|}} + \mathrm{e}^{-\mathrm{i}\frac{\phi}{2}} \sqrt{\frac{|\epsilon - M|}{|\epsilon + M|}} \end{aligned} \tag{3.37}$$

and $\mathbf{k}' || \mathbf{r}$, $k' = k$.

We now focus on the full dipole potential,

$$V^{tc}(\mathbf{r}) = \frac{D}{R}\left(\frac{1}{|\mathbf{r} - \mathbf{c}_+|} - \frac{1}{|\mathbf{r} - \mathbf{c}_-|}\right),$$

and from this, using

$$\int d\mathbf{r} \frac{\mathrm{e}^{-\mathrm{i}\mathbf{k}\cdot\mathbf{r}}}{r} = \frac{2\pi}{k},$$

we may calculate the corresponding Fourier transform,

$$\tilde{V}^{tc}(\mathbf{k}) = \frac{4\mathrm{i}\pi D}{Rk} \sin(\mathbf{k} \cdot \mathbf{c}_-).$$

Turning to the ultra-relativistic limit, $\epsilon \gg M$, and substituting this into (3.37) we arrive at

$$f^{Born}(\phi, \phi_{\mathbf{k}}) = \mathrm{i}\frac{2D\sqrt{2\pi k}}{|\mathbf{k}' - \mathbf{k}| c_-} \cos\left(\frac{\phi - \phi_{\mathbf{k}}}{2}\right) \sin((\mathbf{k}' - \mathbf{k}) \cdot \mathbf{c}_-). \tag{3.38}$$

Simple expressions are obtainable in the limit $kR \to 0$ by using

$$|\mathbf{k}' - \mathbf{k}| = 2k \sin\left(\frac{\phi - \phi_{\mathbf{k}}}{2}\right) \text{ and } (\mathbf{k}' - \mathbf{k}) \cdot \mathbf{c}_- = \frac{kR}{2}(\cos(\phi) - \cos(\phi_{\mathbf{k}})) :$$

$$f^{Born}(\phi - \phi_{\mathbf{k}}) = \mathrm{i}D\sqrt{2\pi k} \cos\left(\frac{\phi - \phi_{\mathbf{k}}}{2}\right) \sin\left(\frac{\phi + \phi_{\mathbf{k}}}{2}\right).$$

Now we may calculate the scattering and transport cross sections analytically

$$\Lambda_{tr} = \frac{\pi^2 D^2 k}{2},$$
$$\Lambda = (1 + 2\sin^2(\phi_{\mathbf{k}}))\Lambda_{tr}.$$

Notably, Λ_{tr} is isotropic w.r.t. the angle of incidence $\phi_{\mathbf{k}}$ in this limit, see fig.

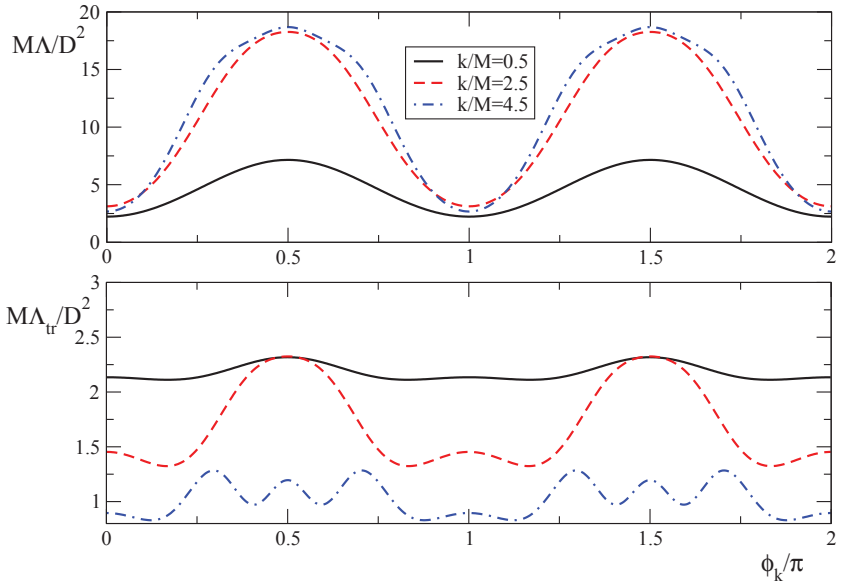

Figure 3.11.: Scattering and transport amplitude for a dipole impurity in Born approximation calculated by numerical integration of (3.38). Note that Λ_{tr} becomes constant for $k \to 0$.

3.11. We can trace this back to the prefactor $\cos\left(\frac{\phi-\phi_{\mathbf{k}}}{2}\right)$, which is characteristic for Dirac fermions and is causing the well known "absence of backscattering" by short ranged impurities [1].

Since Λ_{tr} is corresponding to the resistivity induced by the potential, one may argue, observing the isotropy w.r.t. $\phi_{\mathbf{k}}$ of the former of the previous two equation, that even for a graphene sample with an colinear dipole impurity array immersed on it, the conductance will be isotropic. However, the exact analysis in the previous section shows that there should be a net incidence angle dependency. We conclude that Born approximation fails at low energies.

4 Graphene Quantum Dots with Spin-Orbit Coupling

In this chapter graphene with some electrostatic confining potential, which defines a quantum dot, is considered [52]. Such an potential may be induced by a gate, see for instance [53], or a clusters of impurities, [54]. For some theoretical review one may check [55], [31] and [56], where such quantum dots were treated, but without including SOC, see sec. 2.1.3. However, in reality SOC effects are of course inevitable. Our goal will be to characterize the dots with respect to the shape of the bound level spectrum and critical behavior as a function of SOC related parameters M_{so} and λ_R, since we may expect that a wide range of this parameter space to be experimentally accessible in the near future.

For the sake of simplicity we will limit the discussion to circular-symmetric potentials, since this allows to reduce the corresponding mathematical problem to one dimension and still would allow us to draw conclusions on general behavior.

4.1 General Potentials

We consider the Dirac Hamiltonian of the form (2.12) with an additional scalar potential,

$$H = -\mathrm{i}(\sigma_x\tau_z\partial_x + \sigma_y\partial_y) + \frac{\lambda_R}{2}(\sigma_x s_y\tau_z - \sigma_y s_x) + M_{so}\sigma_z s_z\tau_z + V(r), \tag{4.1}$$

which acts on the space of functions $\boldsymbol{\psi} : \mathbb{R}^2 \to \mathbb{C}^8$:

$$\boldsymbol{\psi}(\mathbf{r}) = \left[\psi_{A\uparrow\mathbf{K}}(\mathbf{r}), \psi_{B\uparrow\mathbf{K}}(\mathbf{r}), \psi_{A\downarrow\mathbf{K}}(\mathbf{r}), \psi_{B\downarrow\mathbf{K}}(\mathbf{r}), \psi_{A\uparrow\mathbf{K}'}(\mathbf{r}), \psi_{B\uparrow\mathbf{K}'}(\mathbf{r}), \psi_{A\downarrow\mathbf{K}'}(\mathbf{r}), \psi_{B\downarrow\mathbf{K}'}(\mathbf{r})\right]^T.$$

Again, we use the units (2.16) for ϵ, M_{so}, λ_R and possible coupling parameters in V. From now on we also will skip the subscript *so* with M_{so} and simply write M. $V(r)$ we choose to be some rotationally symmetric potential.

As we will need them later on, when investigating the scattering, the plain wave-solutions of the free problem ($V \equiv 0$) are provided in the projection on the **K**-sector [1]:

$$\psi^{\pm}_{\mathbf{k}}(\mathbf{r}) = \left[\mathrm{i}\frac{k\mathrm{e}^{-\mathrm{i}\theta_{\mathbf{k}}}}{\epsilon_{\mathbf{k}} - M}, \mathrm{i}, \pm 1, \pm\frac{k\mathrm{e}^{\mathrm{i}\theta_{\mathbf{k}}}}{\epsilon_{\mathbf{k}} - M}\right]^T \mathrm{e}^{\mathrm{i}\mathbf{k}\cdot\mathbf{r}}, \tag{4.2}$$

where $\theta_{\mathbf{k}} = \arg(k_x + \mathrm{i}k_y)$ and

$$\epsilon_{\mathbf{k}} = \mp\frac{\lambda_R}{2} + \sqrt{\left(M \pm \frac{\lambda_R}{2}\right)^2 + k^2}$$

are the positive energy-eigenvalues. The negative energy-eigenvalues are given by

$$\epsilon_{\mathbf{k}} = \mp\frac{\lambda_R}{2} - \sqrt{\left(M \pm \frac{\lambda_R}{2}\right)^2 + k^2},$$

see fig. 2.4. The eigenvalues in the **K**′-sector follow from symmetries of the Hamiltonian, see 4.1.1 below.

One may easily show that

$$[H_{\mathbf{K}^{(\prime)}}, J_z] = 0, \tag{4.3}$$

where $J_z = -\mathrm{i}\partial_\phi + \frac{s_z}{2} + \frac{\tau_z\sigma_z}{2}$ is the corresponding angular momentum. In analogy to the procedure in 2.3 this suggests the following ansatz for the wave function projections around **K**

$$\psi^{\mathbf{K}}_m(\mathbf{r}) = \left[\mathrm{e}^{\mathrm{i}(m-1)\phi}a^{\mathbf{K}}_{\uparrow}(r), \mathrm{i}\mathrm{e}^{\mathrm{i}m\phi}b^{\mathbf{K}}_{\uparrow}(r), \mathrm{e}^{\mathrm{i}m\phi}a^{\mathbf{K}}_{\downarrow}(r), \mathrm{i}\mathrm{e}^{\mathrm{i}(m+1)\phi}b^{\mathbf{K}}_{\downarrow}(r)\right]^T$$

and around **K**′

$$\psi^{\mathbf{K}'}_m(\mathbf{r}) = \left[\mathrm{e}^{\mathrm{i}m\phi}a^{\mathbf{K}'}_{\uparrow}(r), \mathrm{i}\mathrm{e}^{\mathrm{i}(m-1)\phi}b^{\mathbf{K}'}_{\uparrow}(r), \mathrm{e}^{\mathrm{i}(m+1)\phi}a^{\mathbf{K}'}_{\downarrow}(r), \mathrm{i}\mathrm{e}^{\mathrm{i}m\phi}b^{\mathbf{K}'}_{\downarrow}(r)\right]^T,$$

Where $m \in \mathbb{Z}$, to ensure periodicity. Using $-\mathrm{i}(\partial_x \pm \mathrm{i}\partial_y) = \mathrm{e}^{\pm\mathrm{i}\phi}(-\mathrm{i}\partial_r \pm \frac{\partial_\phi}{r})$ the projection of the Hamiltonian into the subspace of the **K**-valley and a total angular momentum m yields the following system of differential equations

$$\begin{aligned} 0 =& \begin{bmatrix} M - (\epsilon - V(r)) & \partial_r + \frac{m}{r} & & \\ -\partial_r + \frac{m-1}{r} & -M - (\epsilon - V(r)) & -\lambda_R & \\ & -\lambda_R & -M - (\epsilon - V(r)) & \partial_r + \frac{m+1}{r} \\ & & -\partial_r + \frac{m}{r} & M - (\epsilon - V(r)) \end{bmatrix} \begin{bmatrix} a^{\mathbf{K}}_{\uparrow}(r) \\ b^{\mathbf{K}}_{\uparrow}(r) \\ a^{\mathbf{K}}_{\downarrow}(r) \\ b^{\mathbf{K}}_{\downarrow}(r) \end{bmatrix} \\ =& (H^{\mathbf{K}}_m - \epsilon)\psi^{\mathbf{K}}_m(r) \end{aligned}$$

(4.4)

and for $\mathbf{K}'$ subspace

$$\begin{aligned} 0 =& \begin{bmatrix} -M-(\epsilon-V(r)) & -\partial_r+\frac{m-1}{r} & & -\lambda_R \\ \partial_r+\frac{m}{r} & M-(\epsilon-V(r)) & & \\ & & M-(\epsilon-V(r)) & -\partial_r+\frac{m}{r} \\ -\lambda_R & & \partial_r+\frac{m+1}{r} & -M-(\epsilon-V(r)) \end{bmatrix} \begin{bmatrix} a_{\uparrow}^{\mathbf{K}'}(r) \\ b_{\uparrow}^{\mathbf{K}'}(r) \\ a_{\downarrow}^{\mathbf{K}'}(r) \\ b_{\downarrow}^{\mathbf{K}'}(r) \end{bmatrix} \\ =& (H_m^{\mathbf{K}'}-\epsilon)\boldsymbol{\psi}_m^{\mathbf{K}'}(r). \end{aligned}$$

(4.5)

4.1.1 Symmetries

The symmetries of a Hamiltonian help to reduce the problem with respect to degrees of freedom of any considered system, which makes it very helpful to collect as many of them as possible, before proceeding with the calculations.

Besides the conservation of the total spin J_z, (4.3), one finds the following symmetries:

$$\sigma_y s_y H_m^{\mathbf{K}} \sigma_y s_y = H_{-m}^{\mathbf{K}} \text{ and } \sigma_x H_m^{\mathbf{K}} \sigma_x = H_m^{\mathbf{K}'}, \tag{4.6}$$

where $H_m^{\mathbf{K}}, H_m^{\mathbf{K}'}$ are the projections of the full Hamiltonian on the corresponding valley and angular momentum subspace. Note that although by this transformations the valley and total angular momentum degree of freedom is changed in the projections on these sectors, the total Hamiltonian, which is the direct sum of all projections, is conserved.

The first operation in (4.6) is related to parity, the product of both to time reversal. These symmetries ensure a fourfold degeneracy for any possible bound state. Due to this we may focus on $\mathbf{K}$ and $m \geq 0$, since the rest follows by the respective transformations in (4.6).

One may already see that for $\lambda_R = 0$ a weak, angle dependent perturbation will change the situation for the observables at most in the second order. Considering a potential of the form

$$V_p(r,\phi) = \sum_{m\neq 0} a_m(r) \mathrm{e}^{\mathrm{i}m\phi} \text{ with } a_m = a_{-m}^*.$$

Here one may neglect $m = 0$, since this will only result in a radial shift of $V(r)$ and the the prior arguments still are true. Then the degenerate states do not mix, since they are spin- and valley-orthogonal. All the other states are also not altered in the first order, since V_p does not conserve the angular quantum

number m. We conclude that the leading contribution is due to the second order. Also one may see that symmetries are conserved up to any order for finite λ_R if $a_m = a_{-m}$.

There is also a "symmetry" in the Rashba parameter λ_R, which is not a degree of freedom of the system, but merely a parameter:

$$s_z H_m^{\mathbf{K}^{(\prime)}}(\lambda_R) s_z = H_m^{\mathbf{K}^{(\prime)}}(-\lambda_R). \tag{4.7}$$

This means that for any bound state of $H(\lambda_R)$ with a defined valley and angular momentum and the energy ϵ_{λ_R} there is a bound state of the $H(-\lambda_R)$ with the energy $\epsilon_{-\lambda_R} = \epsilon_{\lambda_R}$ and the same valley and angular momentum. Obviously one may focus on $\lambda_R > 0$ during calculations. If the spectum has an analytic dependency on λ_R, one may expect a quadratic dependency of non degenerate[1] states of lambda at $\lambda_R \to 0$, the energies behave as $\epsilon_{\lambda_R} = \epsilon_0 + \mathcal{O}\left(\lambda_R^2\right)$.

One may now obviously not proceed along the route of 2.3, since one has four coupled equations instead of only two. It is possible, though, to decouple the 4 coupled differential equations into two 2×2 blocks using a constant, linear transformation in one of the cases, $\partial_r V = 0$, or $m = 0$. To see this, we start at (4.4) and substitute $a_\uparrow$ and $b_\downarrow$ in the rest of the equations. The result one may write in a convenient form using Pauli-matrices:

$$0 = \left[\frac{1}{M-\epsilon+V}\left(\partial_r^2 - \frac{m^2-\frac{1}{2}}{r^2} + \frac{(\partial_r V)}{M-\epsilon+V}\left[-\partial_r + \frac{1}{2r}\right] - M - \epsilon + V\right)\mathbb{1} - \frac{m(\partial_r V)}{r(M-\epsilon+V)}\sigma_z - \lambda_R\sigma_x\right]\sqrt{r}^{-1}\begin{bmatrix} b_\uparrow \\ a_\downarrow \end{bmatrix}. \tag{4.8}$$

Note that one generally may decouple equations of the form $M\mathbf{v} = (A\sigma_i + B\sigma_j)\mathbf{v} = 0$ by the transformation $M \to \tilde{U}MU$ with some constant matrices $U, \tilde{U}$. In (4.8) applying this would be possible in the cases $\lambda = 0$ or, less naively, $m(\partial_r V) = 0$. This is not a coincidence. Note that $H_m^{\mathbf{K}}$ commutes with the first symmetry in (4.6) for $m = 0$. By using

$$UH_0^K U^{-1} = \begin{bmatrix} V + (M-\epsilon) & \partial_r & & \\ -\partial_r - \frac{1}{r} & V - (M + \epsilon - \lambda_R) & & \\ & & V - (M + \epsilon + \lambda_R) & -\partial_r - \frac{1}{r} \\ & & \partial_r & V + (M - \epsilon) \end{bmatrix}, \tag{4.9}$$

[1] Non degenerate within the subspace with a fixed angular momentum m.

where

$$U = \frac{1}{\sqrt{2}} \begin{bmatrix} 1 & & & 1 \\ & 1 & -1 & \\ & 1 & 1 & \\ 1 & & & -1 \end{bmatrix}$$

diagonalizes $\sigma_y s_y$, one ends up with a 2×2 equation system with some shifted energy and mass: $\epsilon \to \epsilon \pm \frac{\lambda_R}{2}$, $M \to M \pm \frac{\lambda_R}{2}$. Note that they may be mapped to each other by the transformation

$$H_0^+(\lambda_R) = \sigma_x H_0^-(-\lambda_R)\sigma_x \tag{4.10}$$

where $H^{+(-)}$ is the upper left (lower right) block of the system (4.9).

4.1.2 Free Circular Waves

We would like to find free, circular solutions of our problem, which we will need during our scattering analysis and which will allow us to find solutions of the quantum-well potential. I.e. we are looking at the Hamiltonian (4.4) with $V \equiv 0$.

We observe that the differential operators $\Theta_m^{\pm} = \pm\partial_r + \frac{m}{r}$ correspond to the ladder-operators of the Bessel functions (C.11). This suggests the ansatz

$$\boldsymbol{\psi}_m^{\mathbf{K}}(r) = \left[f^{\uparrow} Z_{m-1}(ur), g^{\uparrow} Z_m(ur), f^{\downarrow} Z_m(ur), g^{\downarrow} Z_{m+1}(ur) \right]^T, \tag{4.11}$$

where Z_m is a regular Bessel function, J_m or Y_m, if

$$U_\epsilon^{\pm} = (\epsilon - M)(\epsilon + M \pm \lambda) > 0,$$

or a modified one, I_m or K_m, if $U_\epsilon^{\pm} < 0$. Note the asymptotically free wave-like behavior of the regular functions, and decaying wave-, bound-like nature of the modified functions. This ansatz reduces the system of differential equations into a purely algebraic equation for the coefficients f and g in (4.11).

Focusing on the case $U_\epsilon^{\pm} > 0$ we arrive at

$$0 = \begin{bmatrix} M-\epsilon & u & 0 & 0 \\ u & -M-\epsilon & -\lambda_R & 0 \\ 0 & -\lambda_R & -M-\epsilon & u \\ 0 & 0 & u & M-\epsilon \end{bmatrix} \begin{bmatrix} f^{\uparrow} \\ g^{\uparrow} \\ f^{\downarrow} \\ g^{\downarrow} \end{bmatrix}.$$

One quickly finds that the matrix above is singular for $u_\epsilon^\pm = \sqrt{|U_\epsilon^\pm|}$, which plays the role of a wave number. Corresponding wave functions are

$$\psi_{\epsilon,m}^{\pm,J}(r) = \begin{bmatrix} \frac{u_\epsilon^\pm}{\epsilon-\Delta} J_{m-1}(u_\epsilon^\pm r) \\ J_m(u_\epsilon^\pm r) \\ \pm J_m(u_\epsilon^\pm r) \\ \pm\frac{u_\epsilon^\pm}{\epsilon-\Delta} J_{m+1}(u_\epsilon^\pm r) \end{bmatrix}, \quad \psi_{\epsilon,m}^{\pm,Y}(r) = \begin{bmatrix} \frac{u_\epsilon^\pm}{\epsilon-\Delta} Y_{m-1}(u_\epsilon^\pm r) \\ Y_m(u_\epsilon^\pm r) \\ \pm Y_m(u_\epsilon^\pm r) \\ \pm\frac{u_\epsilon^\pm}{\epsilon-\Delta} Y_{m+1}(u_\epsilon^\pm r) \end{bmatrix}. \tag{4.12}$$

Note, however, that the Y solutions are diverging at $r \to 0$ and are thus skipped in the free case, since they are not physical.

Repeating the procedure along similar paths one finds for $U_\epsilon^\pm < 0$

$$\psi_{\epsilon,m}^{\pm,I}(r) = \begin{bmatrix} \frac{u_\epsilon^\pm}{\epsilon-\Delta} I_{m-1}(u_\epsilon^\pm r) \\ I_m(u_\epsilon^\pm r) \\ \pm I_m(u_\epsilon^\pm r) \\ \mp\frac{u_\epsilon^\pm}{\epsilon-\Delta} I_{m+1}(u_\epsilon^\pm r) \end{bmatrix}, \quad \psi_{\epsilon,m}^{\pm,K}(r) = \begin{bmatrix} -\frac{u_\epsilon^\pm}{\epsilon-\Delta} K_{m-1}(u_\epsilon^\pm r) \\ K_m(u_\epsilon^\pm r) \\ \pm K_m(u_\epsilon^\pm r) \\ \pm\frac{u_\epsilon^\pm}{\epsilon-\Delta} K_{m+1}(u_\epsilon^\pm r) \end{bmatrix}. \tag{4.13}$$

Neither of these solutions is normalizable. There may thus be no bound states within the gap without a confining potential.

4.1.3 Currents

In passing we would like to analyze for the possibility of circular, spin selective currents, which may be encountered in edge-states between topologically distinct phases, one example of which is SOC graphene, whose boundaries carry edge states with mentioned properties [12].

The current density operator at **K** is well known to be [1] $\mathbf{j} = \left[\tau_z\sigma_x, \sigma_y\right]^T$. One may easily derive the current density in polar coordinates from this:

$$j_\phi = -\sin(\phi) j_x + \cos(\phi) j_y = -\sin(\phi)\tau_z\sigma_x + \cos(\phi)\sigma_y = \begin{bmatrix} & -\mathrm{i}e^{-\tau_z \mathrm{i}\phi} \\ \mathrm{i}e^{\tau_z \mathrm{i}\phi} & \end{bmatrix}. \tag{4.14}$$

The projection on the m-subspace of the full angular momentum J_z yields $j_\phi = \sigma_x$. The corresponding spin current density is defined by $j_\phi^s = j_\phi s_z$. One may easily show that the second of (4.6) conserves both currents. The first one reverses the total current density but conserves the spin current. Thus any bound state may carry spin filtered, counter propagating, angular currents, which are not canceled by the symmetry-degenerate counterparts from other angular channels ($m \to -m$) and valleys (**K** $\to$ **K**′). This strongly resembles the situation found in [12], although the circular currents in this case are not generated by edge-states, but stem from simple bound states, or, more picturesque, from electrons scattered along the border of a confining potential.

The radial current density is found the same way

$$j_r = \tau_z \begin{bmatrix} & \mathrm{e}^{-\tau_z \mathrm{i}\phi} \\ \mathrm{e}^{\tau_z \mathrm{i}\phi} & \end{bmatrix} \tag{4.15}$$

and its projection on any J_z-subspace gives $j_r = \sigma_y$. Since this matrix is antisymmetric, one expects for the real results of (4.4) and (4.5) the expectation value of j_r to vanish for both spins. Note, however, that this is not necessarily true for superpositions of states, see below.

4.2 Potential Well

The potential well in graphene has already been studied extensively in the past. For a review one may consult [55]. A situation similar to the case dealt with in this work was studied in [56], where no Rashba interaction was included. The potential well will serve us as a way to model qualitative behavior of quantum dots in the presence of SOC.

4.2.1 Model

Now we consider a piecewise constant step potential $V(r) = -V_0\theta(R - r)$ with $V_0 \geq 0$ and $\theta(x)$ is the Heaviside step function. The solutions of (4.4) with this potential are wanted.

The corresponding solutions, from which we have to select the one, fulfilling the continuity at $r = R$, may be copied from equations (4.12) and (4.13) by putting $\epsilon \to \epsilon - V$. The results are

$$\psi^{\sigma,J}_{\epsilon,m}(r) = \begin{bmatrix} \frac{u^\sigma_{\epsilon-V}}{\epsilon-V-M} J_{m-1}(u^\sigma_{\epsilon-V} r) \\ J_m(u^\sigma_{\epsilon-V} r) \\ \sigma J_m(u^\sigma_{\epsilon-V} r) \\ \sigma \frac{u^\sigma_{\epsilon-V}}{\epsilon-V-M} J_{m+1}(u^\sigma_{\epsilon-V} r) \end{bmatrix}, \quad \psi^{\sigma,Y}_{\epsilon,m}(r) = \begin{bmatrix} \frac{u^\sigma_{\epsilon-V}}{\epsilon-V-M} Y_{m-1}(u^\sigma_{\epsilon-V} r) \\ Y_m(u^\sigma_{\epsilon-V} r) \\ \sigma Y_m(u^\sigma_{\epsilon-V} r) \\ \sigma \frac{u^\sigma_{\epsilon-V}}{\epsilon-V-M} Y_{m+1}(u^\sigma_{\epsilon-V} r) \end{bmatrix} \tag{4.16}$$

if $U^\pm_{\epsilon-V} > 0$ and

$$\psi^{\sigma,I}_{\epsilon,m}(r) = \begin{bmatrix} \frac{u^\sigma_{\epsilon-V}}{\epsilon-V-M} I_{m-1}(u^\sigma_{\epsilon-V} r) \\ I_m(u^\sigma_{\epsilon-V} r) \\ \sigma I_m(u^\sigma_{\epsilon-V} r) \\ -\sigma \frac{u^\sigma_{\epsilon-V}}{\epsilon-V-M} I_{m+1}(u^\sigma_{\epsilon-V} r) \end{bmatrix}, \quad \psi^{\sigma,K}_{\epsilon,m}(r) = \begin{bmatrix} -\frac{u^\sigma_{\epsilon-V}}{\epsilon-V-M} K_{m-1}(u^\sigma_{\epsilon-V} r) \\ K_m(u^\sigma_{\epsilon-V} r) \\ \sigma K_m(u^\sigma_{\epsilon-V} r) \\ \sigma \frac{u^\pm_{\epsilon-V}}{\epsilon-V-M} K_{m+1}(u^\sigma_{\epsilon-V} r) \end{bmatrix} \tag{4.17}$$

else, where we introduced the degree of freedom $\sigma = \pm$. Here one has to pay attention to whether the potential solutions are regular on their domain, $[0, R[$

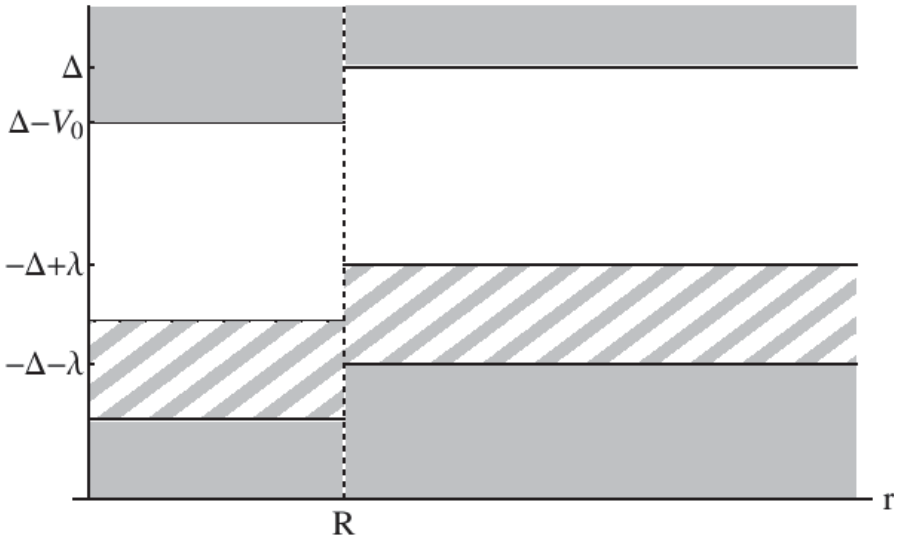

Figure 4.1.: The local, V-dependent, band structure. White area corresponds to $U^{\sigma}_{\epsilon-V} < 0$, gray to $U^{\sigma}_{\epsilon-V} > 0$, gray-dashed to $U^{-}_{\epsilon-V} > 0 > U^{+}_{\epsilon-V}$.

or $[R, \infty[$ respectively. Observing the asymptotic behavior of different Bessel-functions, see (C.6), (C.7), (C.8), (C.10), (C.9), one may conclude that for $r < R$ only J and I type solutions are allowed, while for $R > r$, J, Y and K solutions may be used. Observing the local band-structure, fig. 4.1 we may make statements about the nature of any possibly present state at some fixed energy. Note that in general the minimal number of states at a given ϵ and $m \neq 0$[2] is $N_s = N_> + N_< - 4$, where $N_>$ ($N_<$) is the number of regular solutions at $r > R$ ($r < R$). In the white area at $r > R$ we find only solutions consisting of K_ν functions, which would correspond to bound states given any solution fulfilling continuity there. In this energy range we also have $N_s = 0$, i.e. we can at most have some discrete spectrum there. In the gray dashed are $N_> = 3$, so we expect to have one state, which is continuous in nature (J and Y contributions). In the gray area we have the fully continuous case.

Note that for $m = 0$ the problem reduces to an effectively Rashba uncoupled case with modified ϵ and M. Using (4.9) we can show that the continuity condition (4.18) factorizes into two terms corresponding to the a problem not coupled by λ_R each and with shifted mass and energy $M \to M + \sigma\frac{\lambda_R}{2}, \epsilon \to \epsilon + \sigma\frac{\lambda_R}{2}$. Note that this allows for a situation, where we may have a bound state in the $\sigma = +$ sector parallel to the $\sigma = -$ continuum, right gray dashed area fig. 4.1.

[2] $m = 0$ is a special case due to fact that it can be decoupled, see (4.9)

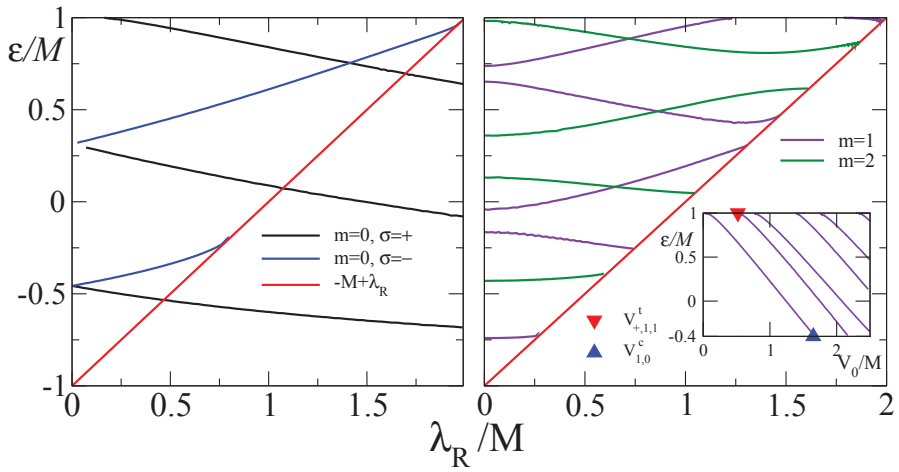

Figure 4.2.: Bound level spectrum as a function of λ_R at a fixed $V_0 = 2M$ and $RM = 3$. Left: $m = 0, \sigma = \pm$. Right: $m = 1, m = 2$. Note that there are non interacting bound states immersed in a continuum. Inset right: Bound level spectrum for $m = 1$ as a function of V_0 at $\lambda_R = 0.6M$.

This is not possible for $m \neq 0$.

We now focus on the energies $\epsilon \in]M - V_0, M[$, which correspond to the range of energies allowing bound states within the well[3].

The continuity at $r = R$ corresponds to

$$a^{+,J}\psi^{+,J}_{\epsilon,m}(R) + a^{-,J}\psi^{-,J}_{\epsilon,m}(R) = a^{+,K}\psi^{+,K}_{\epsilon,m}(R) + a^{-,K}\psi^{-,K}_{\epsilon,m}(R).$$

The condition for the existence of some coefficients a fulfilling above equation may be then written as

$$\det\left[\psi^{+,J}_{\epsilon,m}(R), \psi^{-,J}_{\epsilon,m}(R), \psi^{+,K}_{\epsilon,m}(R), \psi^{-,K}_{\epsilon,m}(R)\right] = 0. \tag{4.18}$$

It is not possible to solve this for ϵ analytically, thus we will rely on numerical root finding procedures.

The corresponding levels are visualized in fig. 4.2 as a functions of λ_R at constant V_0, R and as a function of V_0 at constant λ_R and R (inset). We may clearly see some coexistence of bound states from the $m = 0$, $\sigma = +$ subspace with the $\sigma = -$ continuum (energies below the red dashed line). Also it seems the levels dive almost linearly with growing V_0 and there is some level splitting due to Rashba coupling.

[3]We would like to stress that no continuous solutions were found in the white-white interface, which by above argument of dimensionality may also allow a discrete spectrum of bound states

4.2.2 The Appearance of Bound States

Do bound states exist for arbitrary shallow potential? To answer this question the continuity condition is expanded in $\delta^+ = M - \epsilon$ around $\delta^+ = 0$. One finds that the answer depends strongly on the angular momentum m one considers. In following, we will only focus on $m \geq 0$ and **K**, since the results for $-m$ and **K'** one gets by (4.6).

For $m = 0$ the continuity condition reads

$$0 = \prod_\sigma \Big[(\epsilon - M) u^\sigma_{\epsilon+V_0} J_1\left(u^\sigma_{\epsilon+V_0} R\right) K_0\left(u^\sigma_\epsilon R\right) - u^\sigma_\epsilon (\epsilon - M + V_0) J_0\left(u^\sigma_{\epsilon+V_0} R\right) K_1\left(u^\sigma_\epsilon R\right) \Big] \quad (4.19)$$

or in the limit $\delta^+ \to 0$

$$\prod_\sigma \Big(\delta^+ \sqrt{V_0(2M + V_0 + \sigma\lambda_R)} K_0\Big(\sqrt{\delta^+(2M_{so} + \sigma\lambda_R)} R\Big) J_1\Big(\sqrt{V_0(2M + V_0 + \sigma\lambda_R)} R\Big) + V_0 \sqrt{\delta^+(2M + \sigma\lambda_R)} K_1\Big(\sqrt{\delta^+(2M + \sigma\lambda_R)} R\Big) J_0\Big(\sqrt{V_0(2M + V_0 + \sigma\lambda_R)} R\Big)\Big) = 0.$$

Note that the condition factorizes in two sectors σ. Focusing on one sign of $\sigma = -$ (the other will follow by substitution $\lambda_R \to -\lambda_R$, (4.10)) and expanding the K_n-terms up to the lowest order in δ^+ by using (C.8) one ends up at

$$\delta^+ \sqrt{V_0(2M - \lambda_R + V_0)} J_1\Big(\sqrt{V_0(2M + V_0 - \lambda_R)} R\Big) \left[-\gamma - \ln\left(\frac{\sqrt{\delta^+(2M - \lambda_R)}}{2} R \right) \right] = -\frac{V_0}{R} J_0\Big(\sqrt{V_0(2M + V_0 - \lambda_R)} R\Big)$$

Since $\lim_{x\to 0} x^n \ln(x) = -x^n/n$ one may see

$$\frac{\delta^+}{M}\left(-\gamma + \frac{1}{2} + \ln\left(\frac{\sqrt{2 - \frac{\lambda_R}{M}} RM}{2} \right) \right) = -\frac{\sqrt{V_0}}{RM\sqrt{(2M - \lambda_R)}} \frac{J_0\Big(\sqrt{V_0(2M + V_0 - \lambda_R)} R\Big)}{J_1\Big(\sqrt{V_0(2M + V_0 - \lambda_R)} R\Big)}.$$

Obviously $\delta^+ = 0$ only can be realized for $J_0(\sqrt{V_0(2M - \lambda_R)} R) = 0$. Also, since $\lim_{x\to 0} \frac{J_0(x)}{J_1(x)} = \frac{2}{x}$, $V_0 \to 0$ allows no solution. We conclude that a new bound level appears at a zero of $J_0(\sqrt{V_0(2M + V_0 \pm \lambda_R)} R)$ and that one needs to achieve some finite potential strength V_0 to have a bound level in the $m = 0$ subspace. Same

result was found in [57] in the limit $\lambda_R = M = 0$. We conclude for the threshold potential $V^t_{\sigma,0,i}$ necessary to bind the ith level from the $m = 0$ subspace and $\sigma = \pm$:

$$V^t_{\sigma,0,i} = (M + \sigma\frac{\lambda_R}{2})\left[-1 + \sqrt{1 + \left(\frac{2j^i_0}{R(2M + \sigma\lambda_R)}\right)^2}\right], \quad i > 0.$$

Here j^i_0 is the i-th zero of J_0.

At $m = 1$ in the boundary condition one again may expand K_n around 0 using (C.8). In the limit $\delta^+ \to 0$ one arrives at the condition

$$\delta^+ = 4\frac{(2 - \frac{\lambda_R}{M})^{\frac{\lambda_R}{4M}}(2 + \frac{\lambda_R}{M})^{-\frac{\lambda_R}{4M}}}{\sqrt{4M^2 - \lambda_R^2}R^2}\times$$
$$\exp\left[-2\gamma - \frac{1}{2V_0R^2}\left(\frac{\sqrt{V_0(2M-\lambda_R+V_0)}RJ_0\left(\sqrt{V_0(2M-\lambda_R+V_0)}R\right)}{J_1\left(\sqrt{V_0(2M-\lambda_R+V_0)}R\right)} + (\lambda_R \to -\lambda_R)\right)\right]. \quad (4.20)$$

$\delta^+ \to 0$ now can be achieved by $J_1(\sqrt{V_0(2M \pm \lambda_R + V_0)}R) \to 0$ or in the limit $V_0 \to 0$, when one gets

$$\epsilon = M\left(1 - 4\frac{M(2 - \frac{\lambda_R}{M})^{\frac{\lambda_R}{4M}}(2 + \frac{\lambda_R}{M})^{-\frac{\lambda_R}{4M}}}{\sqrt{4M^2 - \lambda_R^2}R^2}e^{-2\gamma - \frac{2}{V_0R}}\right). \quad (4.21)$$

If $\lambda_R = 0$ the result from [56] is recovered. It follows for the threshold potential strength in the $m = 1$ subspace.

$$V^t_{\pm,1,i} = (M \pm \frac{\lambda_R}{2})\left[-1 + \sqrt{1 + \left(\frac{2j^i_1}{R(2M \pm \lambda_R)}\right)^2}\right], \quad i \geq 0,$$

where j^i_1 is the ith zero of J_1. Note that $i = 0$ is now also included, $j^0_1 = 0$ and thus $V^t_{\pm,1,0} = V^t_{1,0} = 0$.

For $m > 1$ the procedure is repeated. It was not possible to obtain short expressions for the shallow levels $\delta^+ \to 0$, but it is possible to derive a somewhat simpler condition for the threshold potential strength. The condition for the appearance of a new bound level is

$$0 = \sum_{\pm}\Big[2(m-1)\sqrt{V_0(2M \pm \lambda_R + V_0)}J_{m-1}\left(\sqrt{V_0(2M \pm \lambda_R + V_0)}R\right)$$
$$- RV_0(2M \pm \lambda_R)J_m\left(\sqrt{V_0(2M \pm \lambda_R + V_0)}R\right)\Big]J_m\left(\sqrt{V_0(2M \mp \lambda_R + V_0)}R\right). \quad (4.22)$$

We also note that now (4.18) then can't be solved for arbitrary small $V_0 > 0$. We conclude that for arbitrary small V_0 only $|m| = 1$ can provide bound states, which again agrees with [56]. Having found the potential strength V_0, at which a level may appear, and using the fact that the levels dive linearly with growing V_0, one may easily estimate the spectrum.

4.2.3 Critical Potential Strength

In [56] an expression for V_0, at which the lowest level hits the boundary between the gap and the lower continuum, $\epsilon = -M$, was derived for the Rashba uncoupled case. We would like to see, how this changes in the presence of SOC.

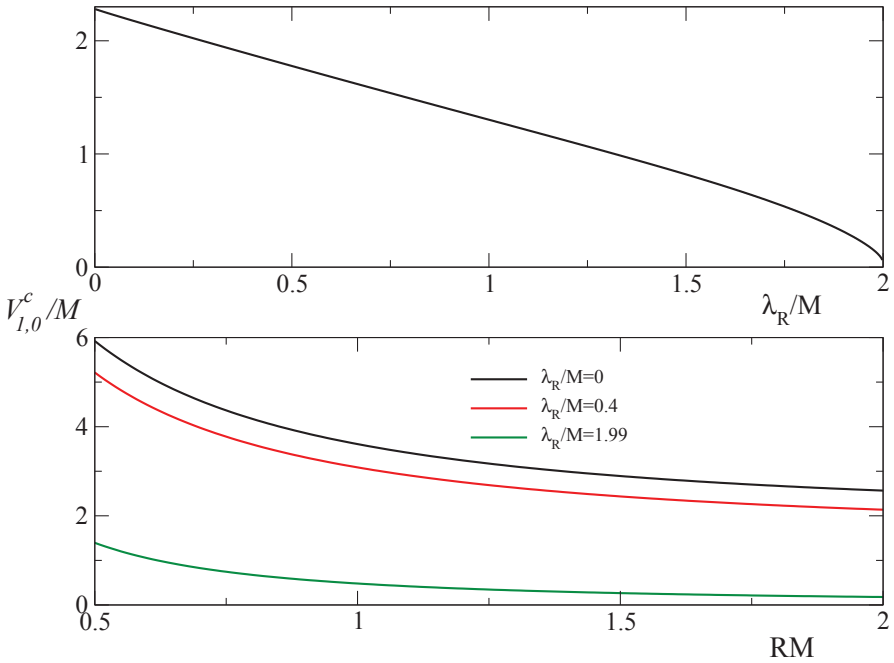

Figure 4.3.: Left: the critical potential strength for the lowest bound state of $m = 1$ as a function of λ_R according to (D.1) at $MR = 3$. The Rashba uncoupled critical energy was calculated to be $V^c_{1,0}(\lambda_R = 0) \approx 2.283M$ in [56], which is nicely fulfilled by our calculated results. The almost-linear behavior may be explained by the weak sensitivity of the lowest bound level with respect to λ_R. Right: same as left as a function of the well size RM. It seems, that the larger the well is, the easier it is to fit an electron into it.

We will call the critical potential strength V^c_κ the potential V_0 at which the bound level, which appears at the threshold potential V^t_κ, will cross the gap

and dive into the opposite continuum. $\boldsymbol{\kappa}$ is the set of quantum numbers, e.g. $\boldsymbol{\kappa} = [\sigma, 0, i]$ for $m \in \{0, 1\}$.

In the presence of Rashba coupling the level of interest is the first bound level in the $m = 1$ subspace. The relevant boundary then is $\epsilon = \lambda_R - M$. If V_0 becomes too big, levels from this subspace may begin diving into the lower half-continuum $\epsilon < \lambda_R - M$. One may again expand (4.19), this time in $\delta^- = \epsilon + M - \lambda_R$ around $\delta^- = 0$. Unfortunately it was not possible to derive a closed expression for $V^c_{1,0}$. We will give the condition for a critical potential in (D.1). Note that although this expression looks intimidating, it is still more simple, than the corresponding full condition (4.18). Using this numerical estimate, which agrees with [56] in the limit $\lambda_R \to 0$, is possible, see fig. 4.3. One may see that a change in the critical potential strength is mainly due to an increase of the valence energy $-M \to -M + \lambda_R$.

Analytic expressions are possible for $m = 0$. Using the effective energy and mass in the $\sigma = \pm$ sector, $\epsilon + \sigma\frac{\lambda_R}{2}$ and $M + \sigma\frac{\lambda_R}{2}$, we may see that the relevant continuum boundaries for the σ-sector are

$$\epsilon + \sigma\tfrac{\lambda_R}{2} = -\left(M + \sigma\tfrac{\lambda_R}{2}\right) \Rightarrow \epsilon = -(M + \sigma\lambda_R).$$

Expanding the decoupled continuity conditions we quickly get

$$V^c_{\sigma,0,i} = (M + \sigma\frac{\lambda_R}{2})\left[1 + \sqrt{1 + \left(\frac{2j^i_1}{R(2M + \sigma\lambda_R)}\right)^2}\right], \quad i > 0,$$

where j^i_1 again is the i-th zero of $J_1(x)$.

Note that for some choices of parameters the lowest state from $m = 0$, $\sigma = +$ subspace for large V_0 may be bound deeper than the first bound level to appear, i.e. the lowest level in the $m = 1$ subspace. However, the relevant boundary for criticality is in the former case $\epsilon = -M - \lambda_R$ which lies higher than the $\sigma = +$ continuum boundary $\epsilon < -M - \lambda_R$. This will always ensure that the ground level with $m = 1$ becomes critical first.

4.2.4 Angular Current Density

On the basis of observations made in [12], we would like to investigate the current structure within the well to search spin selective counter propagating currents.

In what follows we only consider the lowest bound level at $m = 1$, which should serve us as a qualitative example. One may define the local spin current density corresponding to a state $\boldsymbol{\psi}$ by $\boldsymbol{\psi}^\dagger j^s_\phi \boldsymbol{\psi} = \langle j^s_\phi \rangle_r$, where j^s_ϕ is defined as in (4.14).

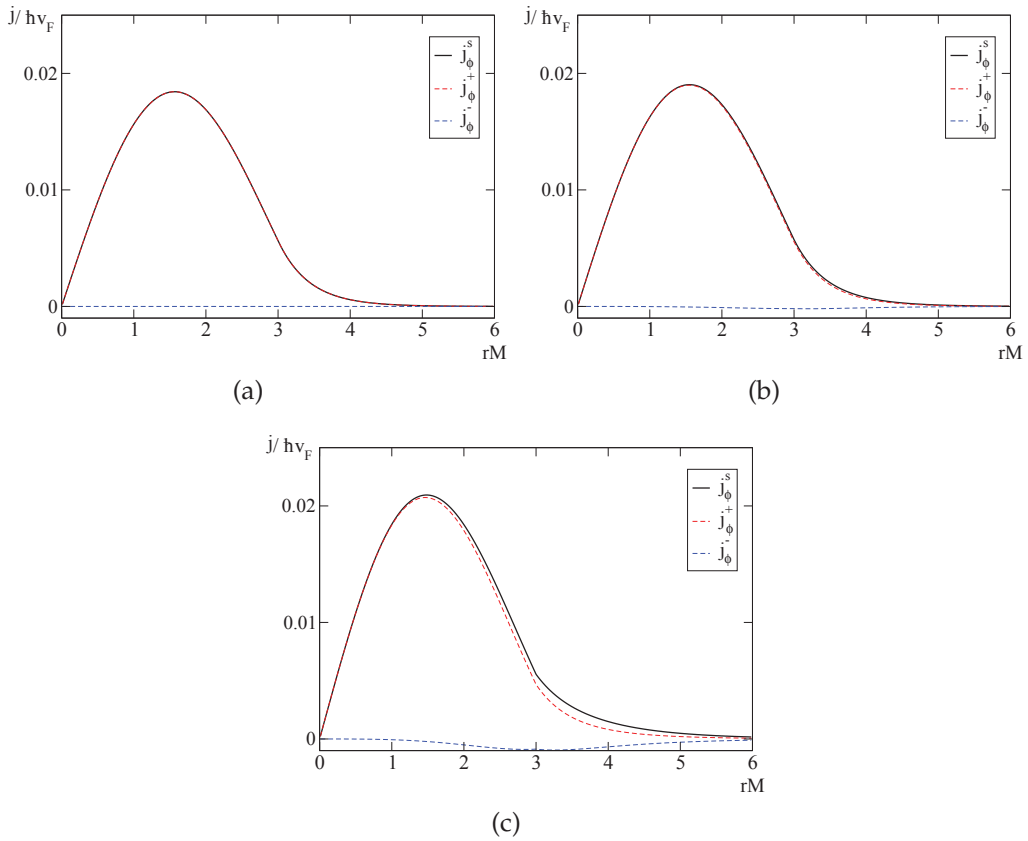

Figure 4.4.: Angular current density carried by lowers bound state of $m = 1$ subspace for $RM = 3$, $\frac{V_0}{M} = 1.05$ and a) $\frac{\lambda_R}{M} = 0$, b) $\lambda_R = 0.5M$, c)$\lambda_R = M$. $j^{\pm}$ is the contribution of $s_z = \pm\frac{1}{2}$ to the current.

The resulting angular current density then qualitatively looks like the curve in fig. 4.4. One may clearly see an angular current, which is bounded by the well. The $s^z = +$ current is in this case dominant. The situation would reverse in the $m = -1$ subspace, where $s^z = -$ contribution would dominate, though the sign of the current would change. Thus the total angular current from both $m = 1$ and $m = -1$ subspace would be zero, while we still have a nonzero effective spin current. A time reversal symmetry breaking perturbation, e.g. a magnetic field, should produce an observable net current.

A similar situation one seems to encounter in [12], where both spins counter propagate along the edge of a graphene sheet. Yet here the situation is a little different, since here the currents are not due to a boundary of topologically distinct continua, but are simply scattered states along the boundaries of the well.

4.2.5 Scattering

We are now interested in the case of an incoming particle along the x-axis, which is scattered by the well. Here we follow the corresponding section in [31] and try to extend the formalism for our spin-orbit coupled case. For this we extend the solutions (4.16) to the region $r > R$ by setting $V_0 = 0$, which then represent continuum states for $\epsilon > M$ and $M \pm \lambda_R > \epsilon$. One will now try to represent a scattered solution by a superposition of circular waves. From now on σ also refers to $m \neq 0$ subspaces. Let us for now focus on the case of incoming electrons with $\sigma = -$.

Note that similar calculations were performed by [54] for the case of a finite region with Rashba coupling. Importantly, there the asymptotic states were considered of the form $\lambda_R = 0$, i.e. $u_\epsilon^+ = u_\epsilon^-$. This means also that there are no bound states, which exist inside a continuum, but are not coupled to it, as in our case. We will see that, unlike other critical levels, these uncoupled bound states do not contribute to scattering via resonances. This property is only protected by the symmetry (4.6). If we introduce a symmetry-breaking perturbation, new resonances should appear.

We note that there are three different energy regions, which admit continuum solutions. In the region $-M - \lambda_R < \epsilon < -M + \lambda_R$ one only has two continuum solutions $\boldsymbol{\psi}^{-,J}$ and $\boldsymbol{\psi}^{-,Y}$, which makes the problem similar to the case discussed in [31]. For $\epsilon > M$ and $\epsilon < -M - \lambda_R$, on the other hand, one has a two-dimensional Hilbert-space of solutions, since there exist four different continuum solutions: $\boldsymbol{\psi}^{\pm,J}$ and $\boldsymbol{\psi}^{\pm,Y}$. Since for now one only focuses on incoming particles with $\sigma = -$, we require that the $\sigma = +$ direction should only have asymptotically outgoing wave contributions. I.e. the $r > R$ solutions in the $\sigma = +$ sector are of the shape

$$\boldsymbol{\psi}^{+,J} + \mathrm{i}\boldsymbol{\psi}^{+,Y} \sim \mathrm{e}^{\mathrm{i}u_\epsilon^+ r}.$$

Now for any ϵ we have a unique solution for $r > R$ in the $\sigma = +$ sector which we from now on will denote by $\boldsymbol{\psi}^{+,>}_{\epsilon,m}$. The corresponding solution $\boldsymbol{\psi}^{-}_{>,m}$ for $\sigma = -$ we will assume to be a linear combination of the form

$$\boldsymbol{\psi}^{-,>}_{\epsilon,m} = \boldsymbol{\psi}^{-,J}_{\epsilon,m} + z_m \boldsymbol{\psi}^{-,Y}_{\epsilon,m},$$

where z_m in general is some complex-valued number, which one gets from the continuity-condition

$$a^{-,<}\boldsymbol{\psi}^{-,<}_{\epsilon+V_0,m}(R) + a^{+,<}\boldsymbol{\psi}^{+,<}_{\epsilon+V_0,m}(R) = A_m(\boldsymbol{\psi}^{-,J}_{\epsilon,m}(R) + z_m\boldsymbol{\psi}^{-,Y}_{\epsilon,m}(R) + \eta_m\boldsymbol{\psi}^{+,>}_{\epsilon,m}(R)). \quad (4.23)$$

Here η_m represents the amplitude for being scattered into the opposite σ-sector, in the current case corresponding to the process $- \to +$. Note that the $\boldsymbol{\psi}^{\pm,<}_{\epsilon+V_0,m}$ parts

represent regular solutions from the set (4.12) and (4.13) at the corresponding energies, and $\boldsymbol{\psi}^{+,>}_{\epsilon,m}$ is either $\boldsymbol{\psi}^{+,K}_{\epsilon,m}$ or $\boldsymbol{\psi}^{+,Y}_{\epsilon,m} + \mathrm{i}\boldsymbol{\psi}^{+,Y}_{\epsilon,m}$, depending on whether one is inside the $\sigma = +$-continuum, $\epsilon < -M - \lambda_R$, or not.

The procedure now is as follows. We find the exact continuous solutions of the problem for each m obeying (4.23). From these, by linear combination, we try to construct a solution, which asymptotically behaves like

$$\vec{u}\mathrm{e}^{\mathrm{i}u^-_\epsilon x} + \vec{v}\frac{f^-(\phi)}{\sqrt{-\mathrm{i}r}}\mathrm{e}^{\mathrm{i}u^-_\epsilon r} + \vec{v}\frac{f^+(\phi)}{\sqrt{r}}\mathrm{e}^{\mathrm{i}u^+_\epsilon r},$$

i.e. a combination of an incoming plane wave with $\sigma = -$ and of outgoing circular waves with both spins, we thus allow for spin-flips.

Lets look at the plane wave-part of the wave function. Following (4.2) the wave incoming at an energy ϵ in the $\sigma = -$ sector along the x-axis is given by

$$\boldsymbol{\psi}^-_{in} = \left[\mathrm{i}\frac{u^-_\epsilon}{\epsilon - M}, \mathrm{i}, -1, -\frac{u^-_\epsilon}{\epsilon - M}\right]^T \mathrm{e}^{\mathrm{i}u^-_\epsilon x}.$$

Note that due to rotational symmetry of the problem the direction of incidence does not matter. Now, using [33]

$$\mathrm{e}^{\mathrm{i}x\cos\phi} = \sum_{m=-\infty}^{\infty} \mathrm{e}^{\mathrm{i}m\phi}(\mathrm{i})^m J_m(x),$$

we may compute

$$\boldsymbol{\psi}^-_{in} = \sum_{m=-\infty}^{\infty} \mathrm{i}^m \mathrm{e}^{\mathrm{i}m\phi}\left[\tfrac{u^-_\epsilon}{\epsilon - M}\mathrm{e}^{-\mathrm{i}\phi}J_{m-1}(u^-_\epsilon r), \mathrm{i}J_m(u^-_\epsilon r), -J_m(u^-_\epsilon r), -\mathrm{i}\tfrac{u^-_\epsilon}{\epsilon - M}\mathrm{e}^{\mathrm{i}\phi}J_{m+1}(u^-_\epsilon r)\right]^T.$$

This is a superposition of free, circular solutions. In the asymptotic limit this behaves like

$$\begin{aligned}\boldsymbol{\psi}^-_{in,\epsilon}(r\to\infty) = {} & \sqrt{\tfrac{1}{2\mathrm{i}\pi u^-_\epsilon r}} \sum_{m=-i\infty}^{\infty} \mathrm{i}^m \mathrm{e}^{\mathrm{i}m\phi}\times \\ & \Big(\left[\tfrac{u^-_\epsilon}{\epsilon - M}\mathrm{e}^{-\mathrm{i}\phi}(-\mathrm{i})^{m-1}, \mathrm{i}(-\mathrm{i})^m, -(-\mathrm{i})^m, -\mathrm{i}\tfrac{u^-_\epsilon}{\epsilon - M}\mathrm{e}^{\mathrm{i}\phi}(-\mathrm{i})^{m+1}\right]^T \mathrm{e}^{\mathrm{i}u^-_\epsilon r} + \\ & \qquad \mathrm{i}\left[\tfrac{u^-_\epsilon}{\epsilon - M}\mathrm{e}^{-\mathrm{i}\phi}(\mathrm{i})^{m-1}, \mathrm{i}(\mathrm{i})^m, -(\mathrm{i})^m, -\mathrm{i}\tfrac{u^-_\epsilon}{\epsilon - M}\mathrm{e}^{\mathrm{i}\phi}(\mathrm{i})^{m+1}\right]^T \mathrm{e}^{-\mathrm{i}u^-_\epsilon r}\Big), \end{aligned} \quad (4.24)$$

where we used that the Bessel function behave like (C.9)

$$J_m(x\to\infty) = \sqrt{\tfrac{2}{\pi x}}\cos(x - \tfrac{m}{2}\pi - \tfrac{\pi}{4}), \quad Y_m(x\to\infty) = \sqrt{\tfrac{2}{\pi x}}\sin(x - \tfrac{m}{2}\pi - \tfrac{\pi}{4}).$$

Now one may proceed in the same spirit as [31], or [58] more fundamentally. Given z_m from the continuity-condition above the $\sigma = -$ part of a general wave function solving the Dirac-equation at some energy ϵ is of the form

$$\begin{aligned}\boldsymbol{\psi}^-_\epsilon = &\sum_{m=-i\infty}^{\infty} A_m \mathrm{e}^{\mathrm{i}m\phi}\times \\ &\left(\left[\tfrac{u^-_\epsilon}{\epsilon-M}\mathrm{e}^{-\mathrm{i}\phi}J_{m-1}(u^-_\epsilon r), \mathrm{i}J_m(u^-_\epsilon r), -J_m(u^-_\epsilon r), -\mathrm{i}\tfrac{u^-_\epsilon}{\epsilon-M}\mathrm{e}^{\mathrm{i}\phi}J_{m+1}(u^-_\epsilon r)\right]^T + \right. \\ &\left. z_m\left[\tfrac{u^-_\epsilon}{\epsilon-M}\mathrm{e}^{-\mathrm{i}\phi}Y_{m-1}(u^-_\epsilon r), \mathrm{i}Y_m(u^-_\epsilon r), -Y_m(u^-_\epsilon r), -\mathrm{i}\tfrac{u^-_\epsilon}{\epsilon-M}\mathrm{e}^{\mathrm{i}\phi}Y_{m+1}(u^-_\epsilon r)\right]^T\right) \quad (4.25)\end{aligned}$$

which, again, in the asymtotic limit behaves like

$$\begin{aligned}\boldsymbol{\psi}^-_\epsilon(r\to\infty) = &\sqrt{\tfrac{1}{2\mathrm{i}\pi u^-_\epsilon r}}\sum_{m=-\infty}^{\infty} A_m \mathrm{e}^{\mathrm{i}m\phi}\times \\ &\left(\left[\tfrac{u^-_\epsilon}{\epsilon-M}\mathrm{e}^{-\mathrm{i}\phi}(-\mathrm{i})^{m-1}, \mathrm{i}(-\mathrm{i})^m, -(-\mathrm{i})^m, -\mathrm{i}\tfrac{u^-_\epsilon}{\epsilon-M}\mathrm{e}^{\mathrm{i}\phi}(-\mathrm{i})^{m+1}\right]^T(1-\mathrm{i}z_m)\mathrm{e}^{\mathrm{i}u^-_\epsilon r} + \right. \\ &\left. \mathrm{i}\left[\tfrac{u^-_\epsilon}{\epsilon-M}\mathrm{e}^{-\mathrm{i}\phi}(\mathrm{i})^{m-1}, \mathrm{i}(\mathrm{i})^m, -(\mathrm{i})^m, -\mathrm{i}\tfrac{u^-_\epsilon}{\epsilon-M}\mathrm{e}^{\mathrm{i}\phi}(\mathrm{i})^{m+1}\right]^T(1+\mathrm{i}z_m)\mathrm{e}^{-\mathrm{i}u^-_\epsilon r}\right). \quad (4.26)\end{aligned}$$

Now one postulates that all the $\mathrm{e}^{-\mathrm{i}u^-_\epsilon r}$ parts of the asymptotic solutions $\boldsymbol{\psi}$ shall be only due to the $\boldsymbol{\psi}^-_{in}$ contribution. To fulfill this the appropriate choice of A_m is

$$A_m = \frac{\mathrm{i}^m}{1+\mathrm{i}z_m}.$$

The outgoing part in the $\sigma = -$ sector of the solution then is

$$\begin{aligned}\boldsymbol{\psi}^-_{out,\epsilon}(r\to\infty) = (\boldsymbol{\psi}^-_\epsilon - \boldsymbol{\psi}^-_{in,\epsilon})(r\to\infty) = \\ \left[\mathrm{i}\tfrac{u^-_\epsilon}{\epsilon-M}\mathrm{e}^{-\mathrm{i}\phi}, \mathrm{i}, -1, -\tfrac{u^-_\epsilon}{\epsilon-M}\mathrm{e}^{\mathrm{i}\phi}\right]^T \sum_{m=-i\infty}^{\infty} \frac{\mathrm{e}^{\mathrm{i}m\phi}}{\sqrt{2\mathrm{i}\pi u^-_\epsilon}}\frac{-2\mathrm{i}z_m}{1+\mathrm{i}z_m}\frac{e^{\mathrm{i}u^-_\epsilon r}}{\sqrt{r}}. \quad (4.27)\end{aligned}$$

We define

$$f^{-,-}_m = \sqrt{\frac{2}{\mathrm{i}\pi u^-_\epsilon}}\frac{-\mathrm{i}z_m}{1+\mathrm{i}z_m},$$

the scattering amplitude into the m channel. Using the definition of the current-density operator, (4.14) and (4.15), one finds

$$\langle J_r\rangle_{out,\pm}/\langle J_x\rangle_{in} = |\sum_m f^{-,\pm}e^{\mathrm{i}m\phi}|^2/r.$$

We note that due to the symmetries 4.6 $f_m = f_{-m}$. From this we expect a symmetric scattering with respect to $\phi \to -\phi$. For the corresponding scattering amplitude into the sector $\sigma = +$ one quickly gets

$$f_m^{-,+} = \sqrt{\frac{2}{i\pi u_\epsilon^+}} \frac{\eta_m}{1 + iz_m},$$

where η_m is the corresponding component in the continuity condition (4.23).

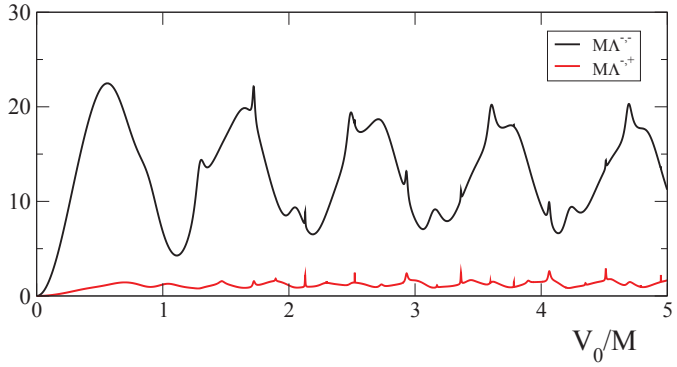

Figure 4.5.: Potential strength dependency of the scattering cross section $\Lambda^{-,\pm}$ for $\epsilon = 2M$, $RM = 3$, $\lambda_R = 0.5M$. Note the strongly resonant behavior.

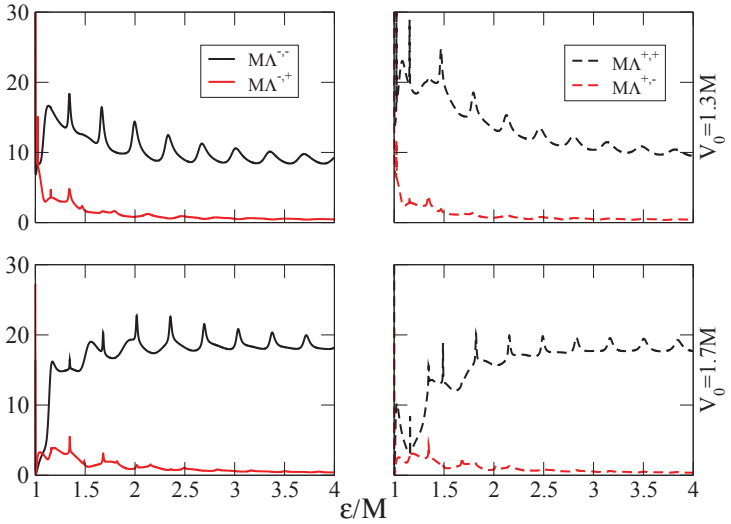

Figure 4.6.: Scattering cross sections $\Lambda^{\sigma,\sigma'}$ for $V_0 = 1.3M$ and $V_0 = 1.7M$ as a function of ϵ for $\lambda = 0.5M$, $RM = 3$. Again we realize the strongly resonant behavior. It seems that the inter scattering between the channels σ is typically suppressed at high momenta.

By normalizing the outgoing current by the incident current density, the total scattering cross section follows to be

$$\Lambda_s^{-,\pm} = \frac{u_\epsilon^\pm}{u_\epsilon^-} \int_0^{2\pi} d\phi |\sum_m f_m^{-,\pm} \mathrm{e}^{\mathrm{i}m\phi}|^2 = 2\pi \frac{u_\epsilon^\pm}{u_\epsilon^-} \sum_m |f_m^{-,\pm}|^2.$$

The u-dependent prefactor is due to the shape of the spinors for the corresponding channels. Note that there is no scattering into the $\sigma = +$ sector from an incoming particle in sector $\sigma = -$ at energies within the half continuum $]-M-\lambda_R, -M+\lambda_R[$. The respective $+ \to \pm$ process one may derive in a completely analogous way. We may now plot the scattering amplitudes, fig. 4.6.

The transport cross sections are also easily calculated

$$\Lambda_{tr}^{\sigma,\sigma'} = \frac{u_\epsilon^{\sigma'}}{u_\epsilon^\sigma} \int_0^{2\pi} d\phi |\sum_m f_m^{\sigma,\sigma'} \mathrm{e}^{\mathrm{i}m\phi}|^2 (1-\cos(\phi)) = \Lambda_{tr}^{\sigma,\sigma'} - 2\pi \frac{u_\epsilon^{\sigma'}}{u_\epsilon^\sigma} \sum_m \Re\left(f_m^{\sigma,\sigma'} \, f_{m+1}^{\sigma,\sigma'\,*}\right).$$

As expected, the overall scattering becomes small for shallow potentials, fig. 4.5. Note the resonant behavior of the scattering amplitudes.

It turns out that whenever a resonance hits the band gap, a new bound level is created. This is illustrated in fig. 4.7 for $m = 0$ (disconnected spins) and fig. 4.8 for $m = 1$ (connected spins). This is indeed not surprising, since there is no formal difference between a bound level diving into a continuum ([30], see below) and an immersed level getting bound. The tuning-direction of V_0 should have no effect.

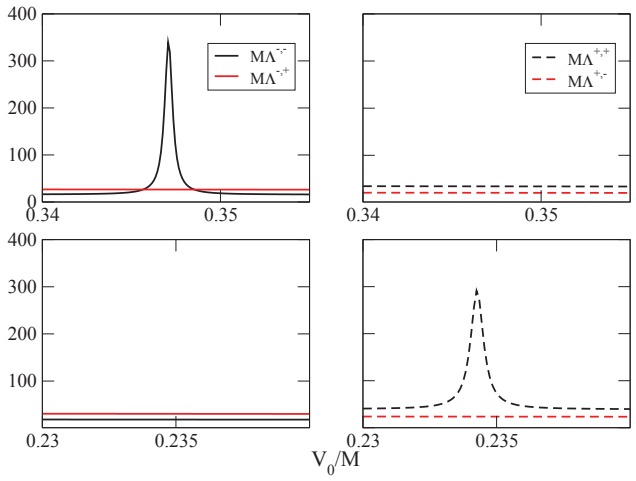

Figure 4.7.: Scattering cross sections $\Lambda^{\sigma,\sigma'}$ at $\epsilon = 1.0001M$ in the vicinity of $V^t_{-,0,1}$ (top) and $V^t_{+,0,1}$ (bottom), $RM = 3$, $\lambda_R = 0.5M$. Note that only resonances appear in scattering processes **from and into** the channel σ corresponding to a level about to be bound. All the other cross sections show no resonances.

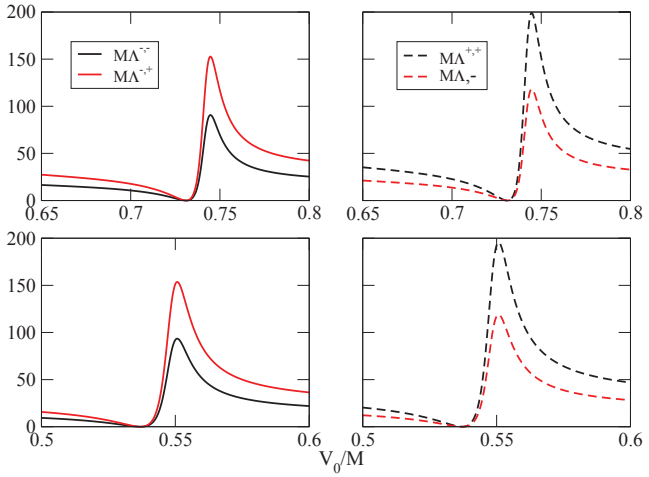

Figure 4.8.: Scattering cross sections $\Lambda^{\sigma,\sigma'}$ at $\epsilon = 1.0001M$ in the vicinity of $V^t_{-,1,1}$ (top) and $V^t_{+,1,1}$ (bottom), $RM = 3$, $\lambda_R = 0.5M$. Since now the according bound levels have no definite σ, all scattering processes are showing resonances. Same behavior was seen also at threshold potentials corresponding to $m > 1$ and for higher levels.

Using this method now allows us to observe resonances in the lower half-continuum of $\sigma = -$, see fig. 4.9, which correspond to the famous Fano resonances [30]. Note that obviosly it makes a large difference, whether the diving level is decoupled in the sectors σ, or not. If that is the case, we may only observe

resonances within the sector, in which the level is bound. Due to this we may not observe resonances of the $\sigma = +$, $m = 0$ sector inside the half continuum $\epsilon \in [-\lambda_R - M, \lambda_R - M]$, see fig. 4.9, and resonances belonging to levels at threshold to get bound, see fig. 4.7 and 4.8. We expect that by introducing a perturbation breaking the symmetry (4.6) *i*) we will get additional resonances.

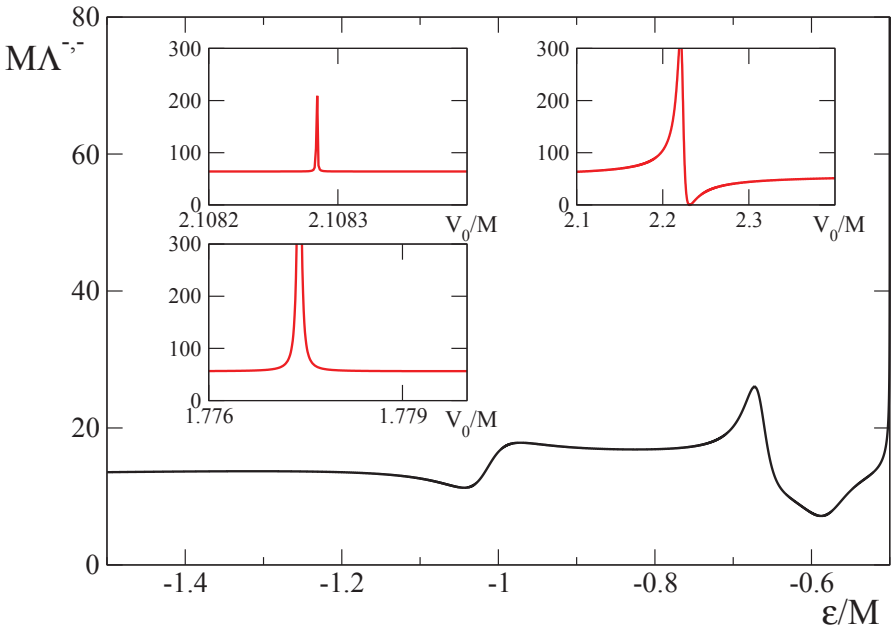

Figure 4.9.: Scattering cross section $\Lambda^{-,-}$ in the lower half-continuum, $RM = 3$, $\lambda_R = 0.5M$, $V = 2.3M$. We see some resonances appear, whenever V_0 hits a critical value, see insets, which makes a bound level dissolve into the lower continuum. Note: $V^c_{1,1} \approx 1.777M$, $V^c_{2,1} \approx 2.108M$, $V^c_{-,0,1} \approx 2.231M$. However, we see no resonances corresponding to levels $m = 1$, $\sigma = +$, which are symmetry protected from the $\sigma = -$ continuum.

For the transport cross section we find similar, resonant behavior. Resonances within the scattering cross section are accompanied by resonances of the transport cross section, see fig. 4.10. All other statements about the scattering cross section also hold for the transport cross section.

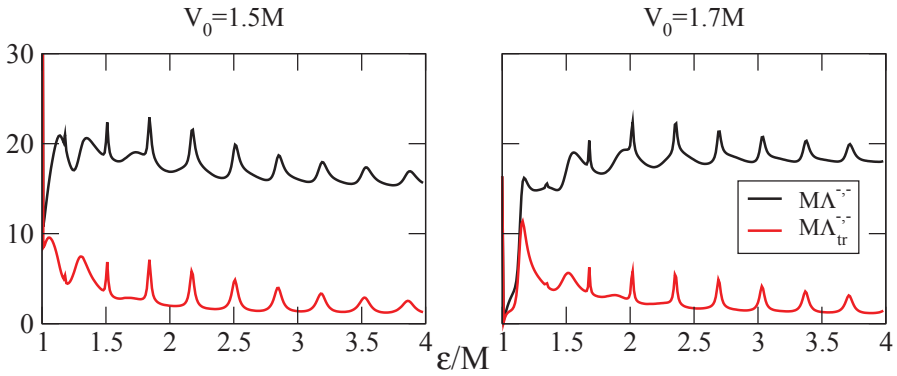

Figure 4.10.: Scattering cross section $\Lambda^{-,-}$ and transport cross section $\Lambda_{tr}^{-,-}$ as a function of energy at $R = 3$, $\lambda_R = 0.5$. Positions of resonances coincide for both cross sections. Comparison of general combinations $\Lambda^{\sigma,\sigma'}$ and $\Lambda_{tr}^{\sigma,\sigma'}$ gives qualitatively equal results.

4.3 Coulomb Impurity

For the sake of completeness we now present the exact solution for the case of a SOC Coulomb impurity, $V(r) = -\frac{\alpha}{r}$, with $m = 0$. However, an exact solution for $m \neq 0$ is so far not available. This also includes $m = 1$, presumably carrying the state with the lowest energy [31], [32].

4.3.1 Exact Solution for $m = 0$

We now focus on the transformed set of equations (4.9). Following [31] and substituting $V = -\frac{\alpha}{r}$ in (4.9) we may observe that the resulting two sets of equations are of the form (2.17) with $m = 0$ and $M \to M \pm \frac{\lambda_R}{2} = M^{\pm}$, $\epsilon \to \epsilon \pm \frac{\lambda_R}{2} = \epsilon^{\pm}$. This allows us simply to read off the solutions from (2.18):

$$\psi^{\pm}(r) = \mathbf{e}_{\mp} \otimes \mathrm{e}^{-u_\epsilon^{\pm} r}(2u_\epsilon^{\pm} r)^{\gamma-\frac{1}{2}} \times \left[\begin{array}{l} \sqrt{(M^{\pm}+\epsilon^{\pm})}\left({}_1F_1(\gamma-\frac{\alpha\epsilon^{\pm}}{u^{\pm}}, 1+2\gamma; 2u_\epsilon^{\pm} r) + \frac{\gamma-\frac{\alpha\epsilon^{\pm}}{u}}{\frac{1}{2}+\frac{\alpha M^{\pm}}{u_\epsilon^{\pm}}}\,{}_1F_1(1+\gamma-\frac{\alpha\epsilon^{\pm}}{u_\epsilon^{\pm}}, 1+2\gamma; 2u_\epsilon^{\pm} r)\right) \\ \sqrt{(M^{\pm}-\epsilon^{\pm})}\left({}_1F_1(\gamma-\frac{\alpha\epsilon^{\pm}}{u_\epsilon^{\pm}}, 1+2\gamma; 2u_\epsilon^{\pm} r) - \frac{\gamma-\frac{\alpha\epsilon^{\pm}}{u_\epsilon^{\pm}}}{\frac{1}{2}+\frac{\alpha M^{\pm}}{u_\epsilon^{\pm}}}\,{}_1F_1(1+\gamma-\frac{\alpha\epsilon^{\pm}}{u_\epsilon^{\pm}}, 1+2\gamma; 2u_\epsilon^{\pm} r)\right) \end{array}\right], \tag{4.28}$$

$\mathbf{e}_\pm = \left[\frac{1}{2} \pm \frac{1}{2}, \frac{1}{2} \mp \frac{1}{2}\right]^T$, $u_\epsilon^\pm = \sqrt{|(M-\epsilon)(M+\epsilon \pm \lambda_R)|}$ and $\gamma = \sqrt{\frac{1}{4} - \alpha^2}$. Following the argument in 2.3 we now may easily select the energies with bound solutions:

$$\epsilon_{n,\pm} = \mathrm{sign}(\alpha)\left(M \pm \tfrac{\lambda_R}{2}\right)\sqrt{\frac{(n+\gamma)^2}{\alpha^2 + (n+\gamma)^2}} \mp \frac{\lambda_R}{2}, \quad n \in \mathbb{N}.$$

Again, we encounter the falling to the center phenomenon at $\alpha = 0.5$, which we will bypass by regularizing the potential:

$$V(r) \to -\frac{\alpha}{\max(R, r)}.$$

Solutions for $r < R$ one may easily read from (4.12) with the shift $\epsilon \to \epsilon + \frac{\alpha}{R}$:

$$\boldsymbol{\psi}^\pm(r)_{r<R} = \mathbf{e}_\mp \otimes \begin{bmatrix} -\sqrt{\epsilon^\pm + \frac{\alpha}{R} + M^\pm}\, J_1(u^\pm_{\epsilon^\pm + \frac{\alpha}{R}} r) \\ \sqrt{\epsilon^\pm + \frac{\alpha}{R} - M^\pm}\, J_0(u^\pm_{\epsilon^\pm + \frac{\alpha}{R}} r) \end{bmatrix}, \tag{4.29}$$

where we used $J_{-n}(x) = -1^n J_n(x)$.

4.3.2 Bound Levels and Critical Coupling

The task is now to find solutions continuous at $R = r$. Note that in (4.28) and (4.29) we may focus on one sign only and thus skip $\pm$, since, as before in 4.2.2, the condition for criticality factorize. In the respective results the $\pm$-cases are then reestablished by taking $M \to M^\pm$.

The condition for the existence of a bound level at ϵ is

$$\sqrt{\frac{M+\epsilon}{\epsilon + M + \frac{\alpha}{R}}} \frac{{}_1F_1(\gamma - \frac{\alpha\epsilon}{u_\epsilon}, 1 + 2\gamma; 2u_\epsilon R) + \frac{\gamma - \frac{\alpha\epsilon}{u}}{\frac{1}{2} + \frac{\alpha M}{u_\epsilon}}\, {}_1F_1(1 + \gamma - \frac{\alpha\epsilon}{u_\epsilon}, 1 + 2\gamma; 2u_\epsilon R)}{J_1\left(u_{\epsilon + \frac{\alpha}{R}} R\right)} =$$

$$-\sqrt{\frac{M-\epsilon}{\epsilon - M + \frac{\alpha}{R}}} \frac{{}_1F_1(\gamma - \frac{\alpha\epsilon}{u_\epsilon}, 1 + 2\gamma; 2u_\epsilon R) - \frac{\gamma - \frac{\alpha\epsilon}{u_\epsilon}}{\frac{1}{2} + \frac{\alpha M}{u_\epsilon}}\, {}_1F_1(1 + \gamma - \frac{\alpha\epsilon}{u_\epsilon}, 1 + 2\gamma; 2u_\epsilon R)}{J_0\left(u_{\epsilon + \frac{\alpha}{R}} R\right)}. \tag{4.30}$$

This condition may be solved numerically. Again, there are values of α, for which the energy of $\sigma = +$ is located inside the continuous spectrum of $\sigma = -$. The diving points of both spins into the corresponding continuum are different, but tend to $\alpha = \frac{1}{2}$ in the limit $R \to 0$, see fig. 4.11.

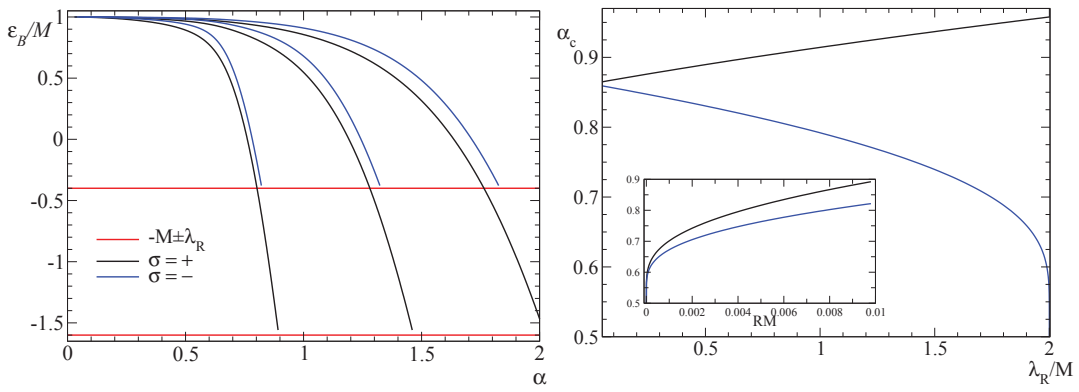

Figure 4.11.: Left: The lowest bound level of $m = 0$, $\sigma = \pm$ in dependency of α up to the critical coupling, $\lambda_R = 0.6M$, $RM = 0.01$. Right: Critical coupling in dependency of λ_R at $RM = 0.01$. Inset: Critical coupling as a function of R at $\lambda_R = 0$ (black) and at $\lambda_R = \pm 0.6M$ (blue) for $\sigma = \mp$.

5 Summary

In this work we investigated the effect of electrostatic impurities on graphene, which form quantum dots. In detail, we focused on the ability of such impurities to bind electrons and the critical phenomena connected to this. We also calculated the scattering and transport cross sections of such impurities, which makes it possible to estimate the conductance using the Drude formula.

In chapter 3 we investigated the effects of two impurities in graphene, which served us as a model for clusters of adatoms. This may be experimentally realized, see e.g. [7].

In the first part of chapter 3 we focused on two equally charged Coulomb centers located at a distance R from each other. Using the LCAO method we were able to estimate the ground state energy. The results were in good agreement with the analytically accessible limits $R \to 0$ and $R \to \infty$. Therefore, we conclude that intermediate results should also be accurate. Further, using the same method we could calculate the distance R_{cr} between the two centers at which the system becomes critical. These results are also in good agreement with previous publications [35].

In the second part of chapter 3 we were able to calculate the qualitative spectrum close to the band edges of a dipole impurity on graphene. In particular, we discovered some universal phenomena, which do not depend on short range details of the problem, e.g. the Efimov scaling and critical dipole strength necessary for appearance of infinite bound state sets. We also found that the functional shapes of the bound energies are independent of short range characteristics of the potentials. A striking feature here is that at finite dipole moments a bound state is always present in contrast to the respective problem in three dimensions. This was also confirmed for the full, two center, dipole potential [48]. It should also be possible to create similar physics in semiconducting hetero structures. Infact, the nonrelativistic calculations then become exact.

We discovered that dipole impurities lack criticality since we found no bound states being able to return to one of the continua. We were able to characterize the qualitative behavior of bound levels deep within the gap using the numerical exact diagonalization procedure. It was possible to find fits for the ground state

energies, which are of the same qualitative shape as analytical results obtained before. It seems that there should be no zero energy states. This supports our previous claims of no critical behavior.

Finally, we addressed the scattering of a dipole impurity in the full relativistic limit using the born approximation and in the non relativistic limit using the analytical results for the low energy continuum states. Although there is no criticality, we could find resonances corresponding to states at the threshold of being bound by the dipole.

In chapter 4 we investigated the effects of SOC on critical effects on circular graphene quantum dots, which serve us as model for general impurities. It turned out that bound states always exist for finite potential strengths. Moreover, we could calculate closed, analytical expressions of threshold potential strengths necessary to bind electrons in the gap as well as conditions for criticality.

We found a strong dependency of threshold and critical potential strength on the Rashba parameter λ_R, due to the corresponding up shift of the valence energy and level splitting, and we were able to show the appearance of Fano resonances.

We also discovered the bound levels existing within, but not coupled to, a continuum and hence are not contributing to scattering. This property is protected by a symmetry. Therefore, we expect that a weak local perturbation, breaking this symmetry, would establish a connection between both and thus additional resonances would appear.

It may be an object of further research to find the dependency of newly emerging scattering resonance on the strength of the perturbation breaking the above mentioned symmetry. Systems with several electrons or holes bound to a dipole may also be investigated.

A Elliptic Coordinates

Given the two centers $\mathbf{c}_\pm = [\pm a, 0]^T$ in the $x-y$-plane one may define $r_\pm = |\mathbf{r}-\mathbf{c}_\pm|$, which enclose the angles $\theta_\pm$ with the x-axis. Then one gets the elliptic coordinates by setting:

$$\begin{aligned} \mu &= \frac{r_+ + r_-}{2a} \in [1, \infty[, \\ \nu &= \frac{r_+ - r_-}{2a} \in [-1, 1[. \end{aligned} \tag{A.1}$$

We refer to μ as the radial and to ν as the angular coordinate.

The inverse transformation reads

$$x = a\mu\nu \text{ and } y^2 = a(\mu^2-1)(1-\nu^2). \tag{A.2}$$

Note that the case of an positive and negative y have to be treated separately.

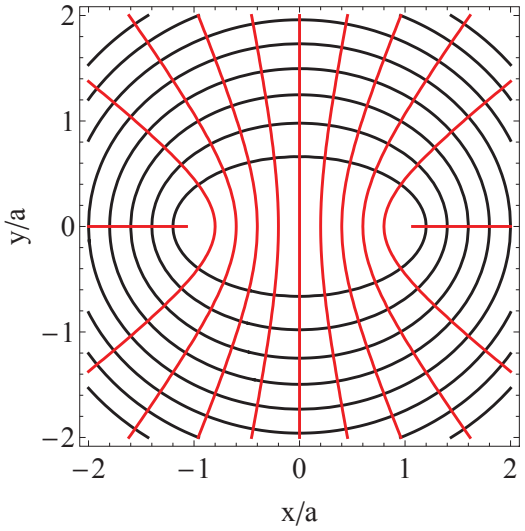

Figure A.1.: Elliptic coordinates. Constant μ (black) and constant ν (red) contours.

Alternatively one may introduce

$$\nu = \cos(\eta), \quad \eta \in [0, 2\pi[.$$

In that case both signs of y are covered. The volume element is

$$dV = a^2 d\mu d\nu \frac{a^2(\mu^2-\nu^2)}{\sqrt{(\mu^2-1)(1-\nu^2)}} = d\mu d\eta \frac{a^2(\mu^2-\cos(\eta)^2)}{\sqrt{\mu^2-1}}. \tag{A.3}$$

The Laplacian is easily obtained from the definition (A.1)

$$\Delta = \frac{1}{a^2(\mu^2-\nu^2)} \left(\sqrt{\mu^2-1}\partial_\mu \frac{1}{\sqrt{\mu^2-1}}\partial_\mu + \sqrt{1-\nu^2}\partial_\nu \frac{1}{\sqrt{1-\nu^2}}\partial_\nu \right).$$

Usefull relations are

$$\begin{aligned}
&\cos(\theta_\pm) = \frac{z \pm a}{r_\pm} = \frac{\mu\nu \pm 1}{\mu \pm \nu}, \quad \sin(\theta_\pm) = \text{sign}(\theta_\pm)\frac{\sqrt{(\mu^2-1)(1-\nu^2)}}{\mu \pm \nu}, \\
&\cos(\theta_+ - \theta_-) = \frac{(\mu^2+\nu^2-2)}{\mu^2-\nu^2} \text{ and } \sin(\theta_+ - \theta_-) = \pm 2\frac{\sqrt{(\mu^2-1)(1-\nu^2)}}{\mu^2-\nu^2}.
\end{aligned} \tag{A.4}$$

The last two results were obtained using addition theorems for sine and cosine.

We also note that by using the η coordinate in the limit $a \to 0$ one arrives at the polar coordinate system, if one redefines $\mu \to a\mu$, $\nu \to a\nu$.

B Properties of Mathieu Functions

One may introduce the Mathieu functions as solutions of the eigenvalue equation (we follow [33] throughout this section)

$$-\partial_z^2 y + 2k^2 \cos(2z) y = a y. \tag{B.1}$$

Within this work we are only interested in periodic solutions, which may be acquired in the form of series of cos and sin functions. Setting $k^2 = q$:

$$\begin{aligned} ce_{2n}(z,q) &= \sum_{r=0}^{\infty} A_{2r}^{2n} \cos(2rz), \;\; ce_{2n+1}(z,q) = \sum_{r=0}^{\infty} A_{2r+1}^{2n+1} \cos((2r+1)z), \\ se_{2n}(z,q) &= \sum_{r=0}^{\infty} B_{2r}^{2n} \sin(2rz), \;\; se_{2n+1}(z,q) = \sum_{r=0}^{\infty} B_{2r+1}^{2n+1} \sin((2r+1)z), \end{aligned} \tag{B.2}$$

where the A and B coefficients are q-dependent. Obviously $ce_i(z)$ are even solutions, while $se_i(z)$ odd w.r.t. $z \to -z$, see fig. B.1.

We denote the eigenvalues, also called characteristic values, corresponding to ce_i and se_i as a_i and b_i and they may be found by solving the eigenvalue equation for the coefficients A, B, which, for instance, for A_{2r}^{2n} reads

$$\begin{bmatrix} a_{2n} & -q & 0 & 0 & 0 & \dots \\ -2q & a-4 & -q & 0 & 0 & \dots \\ 0 & -q & a-16 & -q & 0 & \dots \\ \ddots & \ddots & \ddots & \ddots & \ddots & \ddots \end{bmatrix} \begin{bmatrix} A_0 \\ A_2 \\ A_4 \\ \vdots \end{bmatrix} = 0.$$

We note a hierarchy $a_0 < b_1 \leq a_1 < b_2 \leq a_2 < \dots$, where equality holds for $q = 0$, see fig. B.1. All the characteristics eventually become negative, for sufficiently large q, while $a_0 \leq 0$, where, again, equality is true for $q = 0$.

The Mathieu functions form an orthogonal system,

$$\int_0^{2\pi} \sigma e_j(\phi, q) \sigma' e_{j'}(\phi, q) d\phi = \pi \delta_{\sigma,\sigma'} \delta_{j,j'},$$

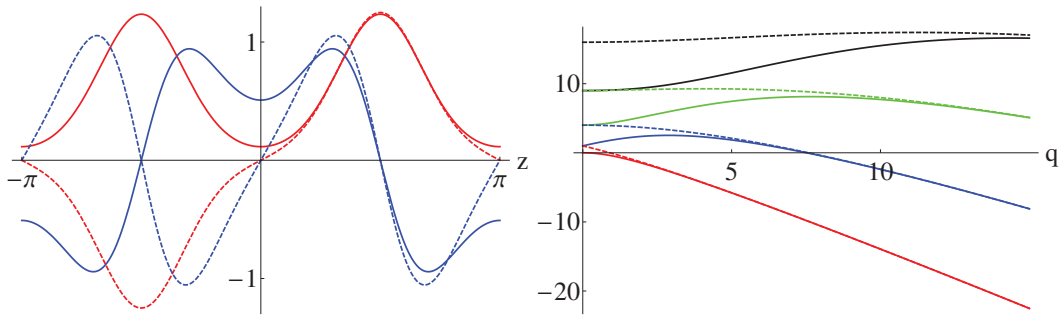

Figure B.1.: Left: The first two periodic Mathieu functions ce^i (solid) and se^i (dashed) at $q = 10$. Right: Characteristic values (solid) a_i, $i \in \{0,1,2,3\}$ and (dashed) b_i, $i \in \{1,2,3,4\}$.

where $\sigma \in \{c,s\}$. We thus may expand simple trigonometric functions in σe:

$$\begin{aligned} \cos(2m\phi) &= \sum_{j=0}^{\infty} ce_{2j}(\phi,q)A_{2m}^{2j}, \quad \cos((2m+1)\phi) = \sum_{j=0}^{\infty} ce_{2j+1}(\phi,q)A_{2m+1}^{2j+1}, \\ \sin(2m\phi) &= \sum_{j=1}^{\infty} se_{2j}(\phi,q)B_{2m}^{2j}, \quad \sin((2m+1)\phi) = \sum_{j=0}^{\infty} se_{2j+1}(\phi,q)B_{2m+1}^{2j+1}. \end{aligned} \tag{B.3}$$

One may also expand trigonometric functions in even order functions $\sigma e_{2j}\left(\frac{\phi}{,}q\right)$ only. Note the halfing of the first variable. One may write

$$\cos(m\phi) = \cos\left(2m\tfrac{\phi}{2}\right) \quad \text{and} \quad \sin(m\phi) = \sin\left(2m\tfrac{\phi}{2}\right)$$

and then simply substitute in the even parts of (B.3).

C Properties of Bessel Functions

Consider the differential equation

$$\left[z^2\partial_z^2 + z\partial_z + (z^2 - \nu^2)\right] J_\nu(z) = 0.$$

One solution may be given for $\arg(z) < \pi$ in the form of the series (we will cite from [33] throughout this chapter)

$$J_\nu(z) = \frac{z^\nu}{2^\nu}\sum_{n=0}^{\infty}(-1)^n\frac{z^{2n}}{2^{2n}\Gamma(\nu+n+1)}. \tag{C.1}$$

This is the Bessel function of the first kind of order $\nu \in \mathbb{C}$. A second, linearly independent solution for non-integer ν (from now on we use $n \in \mathbb{Z}$, $\nu \in \mathbb{C}/\mathbb{Z}$) would also be

$$Y_\nu(z) = \frac{1}{\sin(\nu\pi)}\left(\cos(\nu\pi)J_\nu(z) - J_{-\nu}(z)\right),$$

the Bessel function of the second kind. One may extend the range of this solutions for integer orders by means of the relation

$$\begin{aligned}\pi Y_n(z) = 2J_n(z)\ln(\tfrac{z}{2}) &- \sum_{k=0}^{n-1}\frac{(n-k-1)!}{k!}\left(\frac{z}{2}\right)^{2k-n} \\ &- \sum_{k=0}^{\infty}\frac{(-1)^l}{k!(k+n)!}\left(\frac{z}{2}\right)^{n+2k}\left(\psi(k+1)+\psi(k+n+1)\right),\end{aligned} \tag{C.2}$$

where $\psi(x) = \partial_x \ln(\Gamma(x))$ (for the rest of the chapter $\nu \in \mathbb{C}$, $n \in \mathbb{N}$). One may introduce the complex-valued Hankel functions by means of the transformation

$$\begin{aligned}H_\nu^{(1)}(z) &= J_\nu(z) + \mathrm{i}Y_\nu(z), \\ H_\nu^{(2)}(z) &= J_\nu(z) - \mathrm{i}Y_\nu(z).\end{aligned} \tag{C.3}$$

Now the solutions may be extended to purely imaginary arguments z. One defines the real-valued modified Bessel functions of the first and second kind:

$$I_\nu(z) = e^{-i\frac{\pi}{2}\nu} J_\nu(iz), \quad K_\nu(z) = \frac{\pi i}{2} e^{i\frac{\pi}{2}\nu} H_\nu^{(1)}(iz), \tag{C.4}$$

which are two linearly independent solutions to the differential equation

$$\left[z^2\partial_z^2 + z\partial_z - (z^2 + \nu^2)\right] f(z) = 0. \tag{C.5}$$

Focusing on arbirtary order, one may see that for small $|z|$ from (C.1)

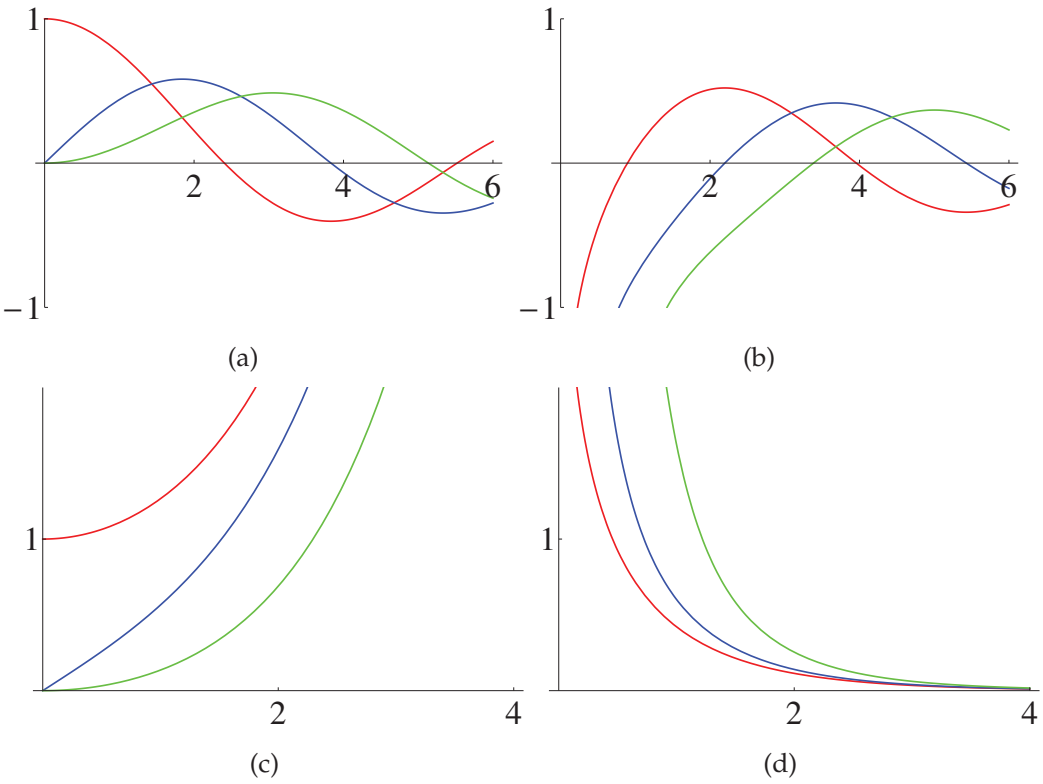

Figure C.1.: Plots of Bessel functions a) J_n, b) Y_n, c) I_n and d) K_n of order 0 (red), 1 (blue) and 2 (green).

$$J_\mu(z) \sim \frac{z^\mu}{2^\mu \Gamma(\mu + 1)} + O(z^{\mu+1}). \tag{C.6}$$

This allows to see the asymptotics of Y_n for integer orders using (C.2)

$$Y_0(z) \sim \frac{2}{\pi}(\ln(\tfrac{z}{2}) + \gamma) + O(z^2), \quad Y_n(z) \sim -\frac{(n-1)!}{z^n} + O(z^{-n+2}) \text{ for n>0.}$$

For non integer orders one may find

$$Y_\nu(z) = \frac{1}{\sin(\pi\nu)}\left[\cos(\pi\nu)\left(\frac{z}{2}\right)^\nu \sum_{k=0}^{\infty} \frac{(-1)^k}{\Gamma(\nu+1+k)}\left(\frac{z}{2}\right)^{2k} - \left(\frac{z}{2}\right)^{-\nu} \sum_{k=0}^{\infty} \frac{(-1)^k}{\Gamma(-\nu+1+k)}\left(\frac{z}{2}\right)^{2k}\right] \quad \text{(C.7)}$$

Further

$$I_n(z) \sim \frac{1}{n!}\left(\frac{z}{2}\right)^n + O(z^{n+2}), \quad K_0(z) \sim -(\gamma + \ln(\tfrac{z}{2})) + O(z^2)$$
$$\text{and for n>0} \quad K_n(z) \sim \frac{(n-1)!}{2}\left(\frac{2}{z}\right)^n + O(z^{-n+2}) \quad \text{(C.8)}$$

where $\gamma = 0.577216$ is the Euler-Mascheroni constant. In the lowest order of z^{-1} one gets for $|z| \to \infty$

$$J_\nu(z) \sim \sqrt{\frac{2}{\pi z}}\cos(z - \tfrac{\pi\nu}{2} - \tfrac{\pi}{4})(1 + O(z^{-1})), \quad Y_\nu(z) \sim \sqrt{\frac{2}{\pi z}}\sin(z - \tfrac{\pi\nu}{2} - \tfrac{\pi}{4})(1 + O(z^{-1})). \quad \text{(C.9)}$$

From this the asymptotics for the Hankel and modified Bessel functions follow:

$$H_\nu^{(1)}(z) \sim \sqrt{\frac{2}{\pi z}}\mathrm{e}^{\mathrm{i}(z - \frac{\pi\nu}{2} - \frac{\pi}{4})}(1 + O(z^{-1})), \quad H_\nu^{(2)}(z) \sim \sqrt{\frac{2}{\pi z}}\mathrm{e}^{-\mathrm{i}(z - \frac{\pi\nu}{2} - \frac{\pi}{4})}(1 + O(z^{-1})),$$
$$I_\nu(z) \sim \frac{\mathrm{e}^z}{\sqrt{2\pi z}}(1 + O(z^{-1})), \quad K_\nu(z) \sim \sqrt{\frac{\pi}{2z}}\mathrm{e}^{-z}(1 + O(z^{-1})). \quad \text{(C.10)}$$

Following recursion formulas turn out to be useful

$$\frac{2}{z}Z_\nu(z) = Z_{\nu-1}(z) + Z_{\nu+1}(z), \quad 2\partial_z Z_\nu(z) = Z_{\nu-1}(z) - Z_{\nu+1}(z),$$

where $Z \in \left\{J, Y, H^{(1)}, H^{(2)}\right\}$. This allows to define some ladder-operators

$$\left(\frac{\nu}{z} \pm \partial_z\right) Z_\nu(z) = Z_{\nu\mp1}(z). \quad \text{(C.11)}$$

We give respective ladder-operators for the modified Bessel functions:

$$\left(\partial_z \pm \frac{\nu}{z}\right) I_\nu(z) = I_{\nu\mp1}(z), \quad \left(\partial_z \pm \frac{\nu}{z}\right) K_\nu(z) = -K_{\nu\mp1}(z).$$

Finally we notice following symmetry relations with respect to an integer order for the regular Bessel and Hankel functions J_n, Y_n and $H_n^{(i)}$:

$$Z_{-n}(z) = (-1)^n Z_n(z), \quad n \in \mathbb{N}.$$

For the modified Bessel functions: $I_{-n}(z) = I_n(z)$. For K_ν this is even valid for non-integer orders: $K_{-\nu}(z) = K_\nu(z)$.

D Condition for the Critical Coupling of a Potential Well Within $m = \pm 1$ Subpace

The condition reads

$$
\begin{aligned}
&-4(V_0+\lambda_R-2M)\times\\
&J_1\left(u^-_{V_0+\lambda_R-M}R\right)\left\{u^+_{\lambda_R-M}(V_0+\lambda_R-2M)J_1\left(u^+_{V_0+\lambda_R-M}R\right)K_0\left(u^+_{\lambda_R-M}R\right)\right.\\
&\left.+\,(\lambda_R-2M)u^+_{V_0+\lambda_R-M}J_0\left(u^+_{V_0+\lambda_R-M}R\right)K_1\left(u^+_{\lambda_R-M}R\right)\right\}\\
&+R(\lambda-2M)\left[u^+_{\lambda_R-M}(V_0+\lambda_R-2M)\left\{u^-_{V_0+\lambda_R-M}J_1\left(u^+_{V_0+\lambda_R-M}R\right)J_2\left(u^-_{V_0+\lambda_R-M}R\right)\right.\right.\\
&\left.+u^+_{V_0+\lambda_R-M}J_1\left(u^-_{V_0+\lambda_R-M}R\right)J_2\left(u^+_{V_0+\lambda_R-M}\right)R\right\}K_0\left(u^+_{\lambda_R-M}R\right)\\
&+(\lambda_R-2M)u^-_{V_0+\lambda_R-M}u^+_{V_0+\lambda_R-M}\left\{J_0\left(u^+_{V_0+\lambda_R-M}R\right)J_2\left(u^-_{V_0+\lambda_R-M}R\right)\right.\\
&\left.+J_0\left(u^-_{V_0+\lambda_R-M}R\right)J_2\left(u^+_{V_0+\lambda_R-M}R\right)\right\}K_1\left(u^+_{\lambda_R-M}R\right)\\
&+u^+_{\lambda_R-M}(V+\lambda_R-2M)\left\{u^+_{V_0+\lambda_R-M}J_0\left(u^+_{V_0+\lambda_R-M}R\right)J_1\left(u^-_{V_0+\lambda_R-M}R\right)\right.\\
&\left.\left.-\,u^-_{V_0+\lambda_R-M}J_0\left(u^-_{V_0+\lambda_R-M}R\right)J_1\left(u^+_{V_0+\lambda_R-M}R\right)\right\}K_2\left(u^+_{\lambda_R-M}R\right)\right]\\
&+R(\lambda-2M)\left[u^+_{\lambda_R-M}(V+\lambda_R-2M)\left\{u^-_{V_0+\lambda_R-M}J_1\left(u^+_{V_0+\lambda_R-M}R\right)J_2\left(u^-_{V_0+\lambda_R-M}R\right)\right.\right.\\
&\left.-u^+_{V_0+\lambda_R-M}J_1\left(u^-_{V_0+\lambda_R-M}R\right)J_2\left(u^+_{V_0+\lambda_R-M}\right)R\right\}K_0\left(u^+_{\lambda_R-M}R\right)+\\
&(\lambda-2M)u^-_{V_0+\lambda_R-M}u^+_{V_0+\lambda_R-M}\left\{J_0\left(u^+_{V_0+\lambda_R-M}R\right)J_2\left(u^-_{V_0+\lambda_R-M}R\right)\right.\\
&\left.+\,J_0\left(u^-_{V_0+\lambda_R-M}R\right)J_2\left(u^+_{V_0+\lambda_R-M}\right)R\right\}K_1\left(u^+_{\lambda_R-M}R\right)\\
&-u^+_{\lambda_R-M}(V+\lambda_R-2M)\left\{u^+_{V_0+\lambda_R-M}J_0\left(u^+_{V_0+\lambda_R-M}R\right)J_1\left(u^-_{V_0+\lambda_R-M}R\right)\right.\\
&\qquad\left.\left.+\,u^-_{V_0+\lambda_R-M}J_0\left(u^-_{V_0+\lambda_R-M}R\right)J_1\left(u^+_{V_0+\lambda_R-M}R\right)\right\}K_2\left(u^+_{\lambda_R-M}R\right)\right]=0. \qquad \text{(D.1)}
\end{aligned}
$$

If any V_0 fulfills this condition, another bound state from $m = \pm 1$ subspace becomes critical.

Bibliography

[1] Castro Neto, A. H., Guinea, F., Peres, N. M. R., Novoselov, K. S., and Geim, A. K. The electronic properties of graphene. Rev. Mod. Phys. **81**, 109–162, Jan (2009).

[2] Wallace, P. R. The band theory of graphite. Phys. Rev. **71**, 622–634, May (1947).

[3] Novoselov, K., Geim, A., S.V., M., Jiand, D., Zhang, Y., Dubonos, S., Grigorieva, I., and Firsov, A. Electric field effect in atomically thin carbon films. Science **306**, 666, Oct (2004).

[4] Van Bommel, A., Crombeen, J., and Van Tooren, A. Leed and auger electron observations of the sic(0001) surface. Surf. Sci. **48**, 463, Mar (1975).

[5] Shelton, J., Patil, H., and Blakely, J. Equilibrium segregation of carbon to a nickel (111) surface: A surface phase transition. Surf. Sci. **43**, 493, Jun (1974).

[6] Vozmediano, M., Katsnelson, M., and Guinea, F. Gauge fields in graphene. Physics Reports **496**, 109, Nov (2010).

[7] Wang, Y., Wong, D., Shytov, A. V., Brar, V. W., Choi, S., Wu, Q., Tsai, H.-Z., Regan, W., Zettl, A., Kawakami, R. K., Louie, S. G., Levitov, L. S., and Crommie, M. F. Observing atomic collapse resonances in artificial nuclei on graphene. Science **340**(6133), 734–737 (2013).

[8] Wakabayashi, K., Fujita, M., Ajiki, H., and Sigrist, M. Electronic and magnetic properties of nanographite ribbons. Phys. Rev. B **59**, 8271–8282, Mar (1999).

[9] Huertas-Hernando, D., Guinea, F., and Brataas, A. Spin-orbit coupling in curved graphene, fullerenes, nanotubes, and nanotube caps. Phys. Rev. B **74**, 155426, Oct (2006).

[10] Weeks, C., Hu, J., Alicea, J., Franz, M., and Wu, R. Engineering a robust quantum spin hall state in graphene via adatom deposition. Phys. Rev. X **1**, 021001, Oct (2011).

[11] Zhang, Y., Tan, Y.-W., Stormer, H., and Kim, P. Experimental observation of the quantum hall effect and berry's phase in graphene. Nature **483**, 201–204, Sep (2005).

[12] Kane, C. L. and Mele, E. J. Quantum spin hall effect in graphene. Phys. Rev. Lett. **95**, 226801, Nov (2005).

[13] Greiner, W., Müller, B., and Rafelski, J. Quantum Electrodynamics of Strong Fields. Springer, (1985).

[14] Khalilov, V. and Choon-Lin, H. Dirac electron in a coulomb field in 2+1 dimensions. Modern Physics Letters A **13**, 615–622, Mar (1998).

[15] Qi, X.-L. and Zhang, S.-C. Topological insulators and superconductors. Rev. Mod. Phys. **83**, 1057–1110, Oct (2011).

[16] Gomes, K., Mar, W., Ko, W., Guinea, F., and Manoharan, H. Designer dirac fermions and topological phases in molecular graphene. Nature **483**, 306–310, Mar (2012).

[17] Ashcroft, N. W. and Mermin, N. D. Solid State Physics. Holt, Rinehart and Winston, (1988).

[18] Weyl, H. Elektron und gravitation i. Z. f. Phys. **32**, 330, May (1929).

[19] Giovannetti, G., Khomyakov, P. A., Brocks, G., Kelly, P. J., and van den Brink, J. Substrate-induced band gap in graphene on hexagonal boron nitride: Ab initio density functional calculations. Phys. Rev. B **76**, 073103, Aug (2007).

[20] Zhou, S. Y., Gweon, G., Fedorov, A. V., First, P. N., de Heer, W. A., Lee1, D.-H. Guinea, F., Castro Neto, A. H., and Lanzara, A. Substrate-induced bandgap opening in epitaxial graphene. Nature Mat. **6**, 770, Sep (2007).

[21] Bychkov, Y. A. and Rashba, E. I. Oscillatory effects and the magnetic susceptibility of carriers in inversion layers. J. Phys. C: Solid State Phys. **17**, 6039, Apr (1984).

[22] Ando, T. Spin-orbit interaction in carbon nanotubes. J.Phys.Soc.Jpn. **69**, 1757, Jun (2000).

[23] Min, H., Hill, J. E., Sinitsyn, N. A., Sahu, B. R., Kleinman, L., and MacDonald, A. H. Intrinsic and rashba spin-orbit interactions in graphene sheets. Phys. Rev. B **74**, 165310, Oct (2006).

[24] Balakrishnan, J., Wai Koon, G. K., Jaiswal, M., H., C. N. A., and Ã–zyilmaz, B. Colossal enhancement of spin-orbit coupling in weakly hydrogenated graphene. Nature Physics **9**, 284, Mar (2013).

[25] Abdelouahed, S., Ernst, A., Henk, J., Maznichenko, I. V., and Mertig, I. Spin-split electronic states in graphene: Effects due to lattice deformation, rashba effect, and adatoms by first principles. Phys. Rev. B **82**, 125424, Sep (2010).

[26] Varykhalov, A., Sánchez-Barriga, J., Shikin, A. M., Biswas, C., Vescovo, E., Rybkin, A., Marchenko, D., and Rader, O. Electronic and magnetic properties of quasifreestanding graphene on ni. Phys. Rev. Lett. **101**, 157601, Oct (2008).

[27] Dirac, P. A. M. The quantum theory of the electron. Proceedings of the Royal Society of London. Series A **117**(778), 610–624 (1928).

[28] Dirac, P. A. M. The quantum theory of the electron. part ii. Proceedings of the Royal Society of London. Series A **118**(779), 351–361 (1928).

[29] Zel'dovich, Y. B. and Popov, S. Electronic structure of superheavy atoms. Sov. Phys. Usp. **14**(6), 403–440 (1971).

[30] Fano, U. Effects of configuration interaction on intensities and phase shifts. Phys. Rev. **124**, 1866–1878, Dec (1961).

[31] Novikov, D. S. Elastic scattering theory and transport in graphene. Phys. Rev. B **76**, 245435, Dec (2007).

[32] Gamayun, O. V., Gorbar, E. V., and Gusynin, V. P. Supercritical coulomb center and excitonic instability in graphene. Phys. Rev. B **80**, 165429, Oct (2009).

[33] Gradshteyn, I. S. and Ryzhik, I. M. Table of Integrals, Series and Products, Fourth Edition. Academic Press New York and London, (1965).

[34] Pereira, V. M., Castro Neto, A. H., Liang, H. Y., and Mahadevan, L. Geometry, mechanics, and electronics of singular structures and wrinkles in graphene. Phys. Rev. Lett. **105**, 156603, Oct (2010).

[35] Sobol, O. O., Gorbar, E. V., and Gusynin, V. P. Supercritical instability in graphene with two charged impurities. Phys. Rev. B **88**, 205116, Nov (2013).

[36] Schwabl, F. Quantenmechanik. Springer, (2002).

[37] Matveev, V., Matrasulov, D., and Rakhimov, H. Two-center problem for the dirac equation. Physics of Atomic Nuclei **63**, 318–321 (2000).

[38] Klöpfer, D., De Martino, A., Matrasulov, D., and Egger, R. Scattering theory and ground-state energy of dirac fermions in graphene with two coulomb impurities. EPJB **87**, 187, Aug (2014).

[39] Prudnikov, A., Brychkov, Y. A., and Marichev, O. Integrals and Series. Gordon and Breach Science Publishers S.A., (1986).

[40] De Martino, A., Klöpfer, D., Matrasulov, D., and Egger, R. Electric-dipole-induced universality for dirac fermions in graphene. Phys. Rev. Lett. **112**, 186603, May (2014).

[41] Camblong, H. E., Epele, L. N., Fanchiotti, H., and Garcia Canal, C. A. Quantum anomaly in molecular physics. Phys. Rev. Lett. **87**, 220402, Nov (2001).

[42] Matrasulov, D. U., Matveev, V. I., and Musakhanov, M. M. Eigenvalue problem for the relativistic electric-dipole system. Phys. Rev. A **60**, 4140–4143, Nov (1999).

[43] Connoly, K. and Griffiths, D. J. Critical dipoles in one, two, and three dimensions. Am. J. Phys. **75**, 524, Jun (2007).

[44] Efimov, V. Energy levels arising from resonant two-body forces in a three-body system. Physics Letters B **33**(8), 563 – 564 (1970).

[45] Shytov, A. V., Katsnelson, M. I., and Levitov, L. S. Atomic collapse and quasi–rydberg states in graphene. Phys. Rev. Lett. **99**, 246802, Dec (2007).

[46] Gamayun, O. V., Gorbar, E. V., and Gusynin, V. P. Supercritical coulomb center and excitonic instability in graphene. Phys. Rev. B **80**, 165429, Oct (2009).

[47] Abramov, D. I. and Komarov, I. V. Weakly bound states of a charged particle in a finite-dipole field. Theor. Math. Phys **13**, 1090, Nov (1972).

[48] Cuenin, J.-C. and Siedentop, H. Dipoles in graphene have infinitely many bound states. arXiv[math phys] **1403.7160v1**, Mar (2014).

[49] Drake, G. W. F. and Goldman, S. P. Application of discrete-basis-set methods to the dirac equation. Phys. Rev. A **23**, 2093–2098, May (1981).

[50] Talman, J. D. Minimax principle for the dirac equation. Phys. Rev. Lett. **57**, 1091–1094, Sep (1986).

[51] Berry, M. and Mondragon, R. Neutrino billiards: time-reversal symmetry-breaking without magnetic fields. Proc.R.Soc.Lond.A **412** (1987).

[52] Klöpfer, D., De Martino, A., and Egger, R. Bound states and supercriticality in graphene-based topological insulators. Crystals-Graphenes **3**, 14, Jan (2013).

[53] Liu, X. L., Hug, D., and Vandersypen, L. M. K. Gate-defined graphene double quantum dot and excited state spectroscopy. Nano Letters **10**(5), 1623–1627 (2010).

[54] Asmar, M. M. and Ulloa, S. E. Spin-orbit interaction and isotropic electronic transport in graphene. Phys. Rev. Lett. **112**, 136602, Apr (2014).

[55] Recher, P. and Trauzettel, B. Quantum dots and spin qubits in graphene. Nanotechnology **21**, 302001, Jul (2010).

[56] Gamayun, O. V., Gorbar, E. V., and Gusynin, V. P. Magnetic field driven instability of a charged center in graphene. Phys. Rev. B **83**, 235104, Jun (2011).

[57] Bardarson, J. H., Titov, M., and Brouwer, P. W. Electrostatic confinement of electrons in an integrable graphene quantum dot. Phys. Rev. Lett. **102**, 226803, Jun (2009).

[58] Landau, L. D. and Lifshitz, E. M. Quantum Mechanics - Non-Relativistic Theory, Second Edition. Pergamon Press, (1965).

Danksagung

Großer Dank geht an alle, die es mir ermöglicht haben diese Arbeit anzufertigen, insbesondere an Prof.Dr. Reinhold Egger, für seine Betreuung und die Gelegenheit an seinem Institut zu forschen.
Prof. Dr. Dr. Carsten Müller danke ich für seine Korefenz dieser Arbeit.
I would also like to thank Prof. Dr. Alessandro De Martino and Prof. Dr. Davron Matrasulov for the fruitfull and pleasant collaboration.
Ausserdem möchte ich danken:

- Meinen Kollegen für die angenehme Arbeitsathmosphäre: Dr. Alexander Zazunov, Aldo Brunetti, Amin Naseri, Andrea Nava, Dr. Arijit Kundu, Arthur Hütten, Donyor Babajanov, Dr. Erik Eriksson, Laura Cohnitz, Roland Hützen, Stephan Weiss und allen die ich vergessen habe.
- Den nichtwissenschaftlichen Mitarbeitern für ihre Hilfsbereitschaft: Jens Bremer und Karin Wildhagen.
- Meinen Eltern, für ihren unaufhörlichen Antrieb.
- Meinen Freunden, für die Ablenkung ausserhalb der Arbeit, was meine geistige Gesundheit in schwierigen Phasen erhalten hat.
- Herren Temme Jr. und Sr., für ihre Durchsicht der Arbeit.
- Meinem Physiklehrer, Klaus Cloppenburg, für seinen wunderbaren Unterricht, welcher mich ausgezeichnet auf mein Studium vorbereitet hat.

Zum Schluß geht ein großer Dank an Maria, für ihre Unterstützung in allen Lebenslagen.

Erklärung

Die hier vorliegende Dissertation habe ich eigenständig und ohne unerlaubte Hilfe angefertigt. Die Dissertation wurde in der vorgelegten oder ähnlichen Form noch bei keiner anderen Institution eingereicht. Ich habe bisher keine erfolglosen Promotionsversuche unternommen.

Düsseldorf, den 22. Sep. 2014.

_____

(Denis Klöpfer)